NAVAL POSTGRADUATE SCHOOL

MONTEREY, CALIFORNIA

THESIS

ADDITIVE MANUFACTURING OF STAINLESS-STEEL NANOCOMPOSITES

by

Michael L. O'Donnell

June 2023

Thesis Advisor:	Troy Ansell
Second Reader:	Walter C. Smith

Approved for public release. Distribution is unlimited.

This project was funded in part by the NPS Naval Research Program.

THIS PAGE INTENTIONALLY LEFT BLANK

REPORT DOCUMENTATION PAGE			*Form Approved OMB No. 0704–0188*

1. AGENCY USE ONLY *(Leave blank)*	**2. REPORT DATE** June 2023	**3. REPORT TYPE AND DATES COVERED** Master's thesis

4. TITLE AND SUBTITLE ADDITIVE MANUFACTURING OF STAINLESS-STEEL NANOCOMPOSITES	**5. FUNDING NUMBERS** NPS-23-N081-A
6. AUTHOR(S) Michael L. O'Donnell	
7. PERFORMING ORGANIZATION NAME(S) AND ADDRESS(ES) Naval Postgraduate School Monterey, CA 93943-5000	**8. PERFORMING ORGANIZATION REPORT NUMBER**
9. SPONSORING / MONITORING AGENCY NAME(S) AND ADDRESS(ES) N/A	**10. SPONSORING / MONITORING AGENCY REPORT NUMBER**

11. SUPPLEMENTARY NOTES The views expressed in this thesis are those of the author and do not reflect the official policy or position of the Department of Defense or the U.S. Government. This project was funded in part by the NPS Naval Research Program.

12a. DISTRIBUTION / AVAILABILITY STATEMENT Approved for public release. Distribution is unlimited.	**12b. DISTRIBUTION CODE** A

13. ABSTRACT (maximum 200 words)

Additive manufacturing of stainless-steel nanocomposites is one potential method for creating hydrophobic metallic surfaces to mitigate corrosion. Laser powder bed fusion (LPBF) is a 3-D printing method utilized to print metallic components including 316L stainless-steel (SS). LPBF was used to print composites of 316L SS and graphene nanoplatelets (GNP) with varying volumetric concentrations. The print energy density parameters for the LPBF process were also varied to investigate potential differences in print quality. To assist in the printing process, the printed material was baked in between print sessions to prevent moisture accumulation or premature particle adhesion. In addition to researching the hydrophobicity of these printed surfaces, samples were polished to a smooth surface to test the hydrophobicity when surface roughness is not a key factor. Through material characterization including sessile water-drop contact angle measurements, optical profilometry, and SEM microscopy, it was determined that the addition of GNP particles enhanced the hydrophobicity of the as-printed samples while additionally showing encouraging improvements to the hydrophobic tendencies of polished samples. Trends suggest that further improvements to the hydrophobicity of 3-D printed samples could be reached with increased GNP concentration or the addition of another nanomaterial with hydrophobic tendencies.

14. SUBJECT TERMS additive manufacturing, graphene nanoplatelets, 3-D printing, hydrophobic surface, stainless steel 316L	**15. NUMBER OF PAGES** 147
	16. PRICE CODE

17. SECURITY CLASSIFICATION OF REPORT Unclassified	**18. SECURITY CLASSIFICATION OF THIS PAGE** Unclassified	**19. SECURITY CLASSIFICATION OF ABSTRACT** Unclassified	**20. LIMITATION OF ABSTRACT** UU

NSN 7540–01-280-5500

Standard Form 298 (Rev. 2–89)
Prescribed by ANSI Std. 239–18

THIS PAGE INTENTIONALLY LEFT BLANK

Approved for public release. Distribution is unlimited.

ADDITIVE MANUFACTURING OF STAINLESS-STEEL NANOCOMPOSITES

Michael L. O'Donnell
Ensign, United States Navy
BS, United States Merchant Marine Academy, 2022

Submitted in partial fulfillment of the
requirements for the degree of

MASTER OF SCIENCE IN MECHANICAL ENGINEERING

from the

NAVAL POSTGRADUATE SCHOOL
June 2023

Approved by: Troy Ansell
Advisor

Walter C. Smith
Second Reader

Brian S. Bingham
Chair, Department of Mechanical and Aerospace Engineering

THIS PAGE INTENTIONALLY LEFT BLANK

ABSTRACT

Additive manufacturing of stainless-steel nanocomposites is one potential method for creating hydrophobic metallic surfaces to mitigate corrosion. Laser powder bed fusion (LPBF) is a 3-D printing method utilized to print metallic components including 316L stainless-steel (SS). LPBF was used to print composites of 316L SS and graphene nanoplatelets (GNP) with varying volumetric concentrations. The print energy density parameters for the LPBF process were also varied to investigate potential differences in print quality. To assist in the printing process, the printed material was baked in between print sessions to prevent moisture accumulation or premature particle adhesion. In addition to researching the hydrophobicity of these printed surfaces, samples were polished to a smooth surface to test the hydrophobicity when surface roughness is not a key factor. Through material characterization including sessile water-drop contact angle measurements, optical profilometry, and SEM microscopy, it was determined that the addition of GNP particles enhanced the hydrophobicity of the as-printed samples while additionally showing encouraging improvements to the hydrophobic tendencies of polished samples. Trends suggest that further improvements to the hydrophobicity of 3-D printed samples could be reached with increased GNP concentration or the addition of another nanomaterial with hydrophobic tendencies.

THIS PAGE INTENTIONALLY LEFT BLANK

TABLE OF CONTENTS

LIST OF FIGURES

THIS PAGE INTENTIONALLY LEFT BLANK

LIST OF TABLES

THIS PAGE INTENTIONALLY LEFT BLANK

ACKNOWLEDGEMENTS

This work would not have been possible without the contributions and support of so many NPS staff members. First, I would like to thank my advisor, Dr. Troy Ansell. Without his ability to help problem solve and assist as needed, the project would never have been completed on time. I would also like to thank Mr. John Mobley from the NPS Mechanical Engineering Shop, who was always able to help me with the post-print machining process with the quickest turnaround time possible. Thank you to Dr. Walter Smith and Stefan Kohlgrueber for training me to use the EOS M100 printer and always being ready to assist when roadblocks in the printing process were met. Thank you to Moritz Menge for providing the training needed to access the clean room to complete most of my experimentation. Thank you to all the staff and support team who provided me with the ability to conduct this research during my time here at NPS.

Finally, I would like to thank all my friends and classmates who helped me complete this year at NPS. Without the ability to switch out of school mode to relax and unwind, this work would never have been completed in a timely manner.

THIS PAGE INTENTIONALLY LEFT BLANK

I. MOTIVATION

A. CORROSION

Corrosion is one of the most substantial economic and engineering issues facing the U.S. Department of Defense, the United States, and the modern world. With the United States estimating that the costs of corrosion being 3–4% of the global Gross Domestic Product (GDP) of $96 trillion, it was estimated that the 2021 cost of corrosion was approximately $6 trillion [1]. It was estimated that the global cost of corrosion in 2013 was $2.5 trillion, which is equivalent to 3.4% of the global GDP [2]. In the United States alone, the collective cost of corrosion was $451 billion, equivalent to 2.7% of U.S. GDP [2]. These estimates reflect an increase from the earliest comprehensive cost of corrosion study in 1949 by H.H. Uhlig. In the study, the cost of corrosion to the United States was estimated to be $5.5 billion ($54 billion adjusted for 2013), equal to 2.1% of 1949 GDP [3].

In 2016, the Department of Defense (DOD) spent $20.6 billion on corrosion-related repairs and upgrades [4]. Under the DOD, the Department of the Navy (DON) was responsible for $6.1 billion worth of corrosion repairs across ships, ground vehicles, and aircraft [5]. Along with the monetary cost, corrosion impacts asset availability. It is estimated that there is an annual loss of 16,700+ hours of availability due to corrosion, taking ships, ground vehicles, and aircraft out of the active fleet and reducing the capabilities of the Navy and Marine Corps [6]. When specifically looking at ships and aircraft, where aero- and hydrodynamics are paramount concerns for maneuverability and operational efficiency, corrosion can lead to increased frictional and surface drag forces, reducing the effectiveness of the asset.

B. BIOFOULING

Biofouling is defined as the "accumulation of aquatic organisms such as microorganisms, plants, and animals, on surfaces and structures immersed in or exposed to the aquatic environment" [7]. In addition to corrosion, biofouling on the hulls of ships is an economic factor that challenges the global and United States merchant fleet as well as U.S. Navy ships. In addition to the economic factor of ships requiring periodic hull

cleanings to remove accumulated biofilm and calcareous growths, there is another associated consequence, ship efficiency. With up to 90% of global transcontinental transportation of goods being moved across ocean waters on merchant ships, the cost of biofouling can influence the labor of moving goods and materials, which can result in greater global prices [8]. Ranging from light slime, which begins to accumulate hours after a ship's submersion into water, to heavy calcareous growths, biofouling can require from 10–85% more power to achieve a desired speed, increasing carbon- and sulfur dioxide emissions up to 70% [9]. Additionally, the presence of biofouling can increase surface friction of a ship up to 70%, decreasing the performance of the ship's drive train and propulsion methods up to 50% of its base value [8].

Biofouling carries a large efficiency and economic cost. Along with the increase in time needed to complete a voyage and linked to the additional fuel required to resist and overcome the additional frictional forces that are applied to the ship with biofilm, there is a substantial monetary cost of biofouling. Across the United States military, merchant, and recreational marine fleets, the annual associated cost of biofouling is $120 billion per year [9]. With a study in 1992, it was calculated that the U.S. Navy accrued $75–100 million yearly in fuel penalties resulting from the biofouling accumulation on the hulls of ships, with an additional $56 million annually to clean and protect the hulls of just the DDG-51 class of ships, 30% of the fleet [10]. Twenty years later, in 2011, it was estimated that the biofouling-related drag increase on ships cost the Navy $180–260 million, not accounting for the cost to remove the growths and refinish the hulls [11]. With the technology at the time, predictions for the increase in cost of biofouling in the Navy increased to $400-540 million annually [10].

C. METALLIC SURFACE PROTECTION

To battle the harmful effects of corrosion and biofouling for aircraft and ships, the U.S. Navy utilizes many forms of metallic protection. One of the most prevalent protection methods used for U.S. Navy aircraft and ships is specialized paint. Paint can be an effective form of metallic protection but requires frequent periods of maintenance to maintain the protective shell. In 1997, 279 aircraft assigned to F/A-18 squadrons were analyzed for paint

usage over a 12-month period with a standard allotment for touch-up paint kits being 2,240 kits. When the study was completed, over 7600 paint kits were used, surpassing the normal allotment by over 5400 kits, a +300% increase [12].

The need for metallic surface protection is amplified when analyzing U.S. Navy ships, as there are more factors leading to metallic fouling, including corrosion, erosion, and biofouling. To protect against each of these harmful reactions, naval ships undergo routine maintenance cycles that involve stripping the protective paint from the ship's hull, cleaning the base metal, and reapplying layers of protective paint. Multiple types of paint are applied to protect against as many dangers as possible including anticorrosive and antifouling coatings. The normal service life for the coatings is five years, which has become problematic for the Navy. In Naval Sea Systems Command's (NAVSEA) 2020 report to Congress, the underwhelming ratio of dry-docks to ships highlights the inability for ships to be maintained at a regular five-year interval, straining the protective coating's ability to prevent biofouling and corrosion. At a ratio of 1:5 dry-docks to ships and a desire to increase the fleet mix from 300 to 355 battle force ships, the need for a stronger metallic protection system is needed [13]. To assist in the battle against corrosion and biofouling and protect a ship hull's integrity, the Navy utilizes remote aquatic vehicles, named Lamp Ray, to perform cleanings and record hull thickness measurements to track the ability to extend or speed up the dry dock cycle [14].

While surface coatings and the Lamp Ray remote aquatic vehicle are crucial in fighting against biofouling growths and corrosion, neither can prevent either phenomenon. To address the root issue plaguing the navy, the spotlight must be shown on the most widely used material to construct aircraft and ships: steel. Steel is naturally hydrophilic, meaning that water will spread across the surface and disperse as evenly as possible. Various studies have been conducted altering the wettability of steel, showing that the initial state before alteration always shows a hydrophilic nature, normally with the contact angle of steel samples being between 40–60 degrees [15]. The point of transition from hydrophilic to hydrophobic is a contact angle greater than 90 degrees, where meeting or exceeding 90 degrees indicates a hydrophobic, or water-fearing, surface [16]. Both types of surfaces are beneficial in different applications, as a hydrophobic surface is desired when trying to

prevent corrosion or biofouling and a hydrophilic surface is desired when placed in a heat exchange system, as the heat transfer is maximized [17], [16]. If it were possible to reverse the material property of steel or stainless steel, creating a hydrophobic surface, water would tend to stay in a spherical shape, moving across the surface without wetting it.

A previous study conducted by students at the Naval Postgraduate School attempted to create a hydrophobic surface of stainless steel-carbon nanotube composite using a laser powder bed fusion 3D printer. In the study, the hydrophobicity of a printed sample was measured by conducting a water drop contact angle measurement over time. By replicating the study with graphene nanoplatelets in place of carbon nanotubes (CNT), the goal will be to test and record if a hydrophobic surface can be created.

II. BACKGROUND

A. METALS AND CORROSION

1. Types of Corrosion

Corrosion is defined as the "destructive attack of a metal by a chemical or electrochemical reaction within its environment," normally accompanied by physical deterioration such as erosion or physical wear [18]. Many types of corrosion are commonly found damaging metallic surfaces, all with varying intensities of danger to the material. Uniform corrosion, the most common form responsible for the most material loss, is considered one of the least dangerous forms of corrosion, as the uniform rate of material loss can be predicted and monitored [19]. Galvanic corrosion, very commonly found in marine environments with ships containing many forms of metal in their construction, occurs when a metallic contact is made between a more and less noble metal, where the less noble metal will begin to corrode [19]. Additionally, in a marine environment is microbial corrosion, where organisms attached to the hull of a ship or submerged structure produce an electron flow or hydrogen ions, weakening and corroding the base metal [20].

Iron and iron-based alloys are subjected to another level of corrosion, as the formation of hydrous ferric oxide on the surface begins to rust the metallic surface [18]. As seen in Figure 1, when a metal is in contact with an electrically conductive environment anodic and cathodic regions form. The anodic half-cell location releases metal ions into the environment at a positive charge, leaving a void space where the atoms were previously located, while the negatively charges electrons traveling to another location in the metal, known as the cathodic site. With iron or iron-based metals, the released ions then interact with oxygen present within the environment to form the ferric oxide known as rust [21].

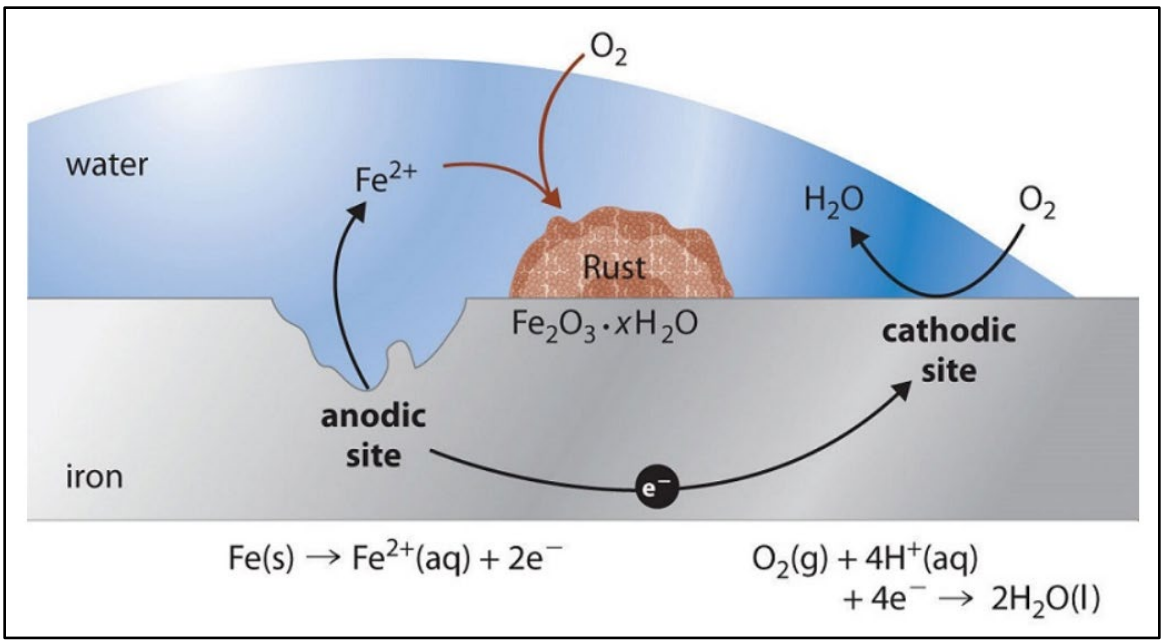

Figure 1. Schematic Diagram of Corrosion Process of Iron in a Water Environment. Source: [21].

2. Typical Rates of Corrosion

Depending on the base metal and corrosive environment in consideration, there are standard rates of corrosion. Carbon steel in motionless seawater has been measured to corrode at a rate of 0.05–0.1 mm/year, a much greater rate than stainless steel at 0.001 mm/year [22]. The standard rates of corrosion are greatly influenced by the material composition of the material as well as environmental variables. The temperature of the environment can greatly increase the rate of corrosion by increasing the internal energy leading ion release, potentially even causing passive metals to become active and reactive [20]. Relative velocity between a metallic structure and the environment can also greatly influence the corrosion rate, acting more as an enhancement to other factors rather than being a direct factor. As corrosion continues to occur on the surface of a metal, a corrosive byproduct begins to form, protecting the base metal. At high velocities, erosive particles within the environment can impinge on the protective layer, removing it and allowing the corrosion process to begin again [23]. While the majority of cases observed indicates that greater velocity (any velocity greater than stationary) guarantees greater corrosion rates, some state otherwise, where lower corrosion rates are observed when in

flowing water [24]. The greatest environmental influence on the rate of corrosion observed on a metal is the level of submersion into the environment. When considering an oceanic seawater environment, the potential corrosion areas are broken up into four zones, as seen in Figure 2. The four zones are identified as atmospheric, splash, tidal, and submerged.

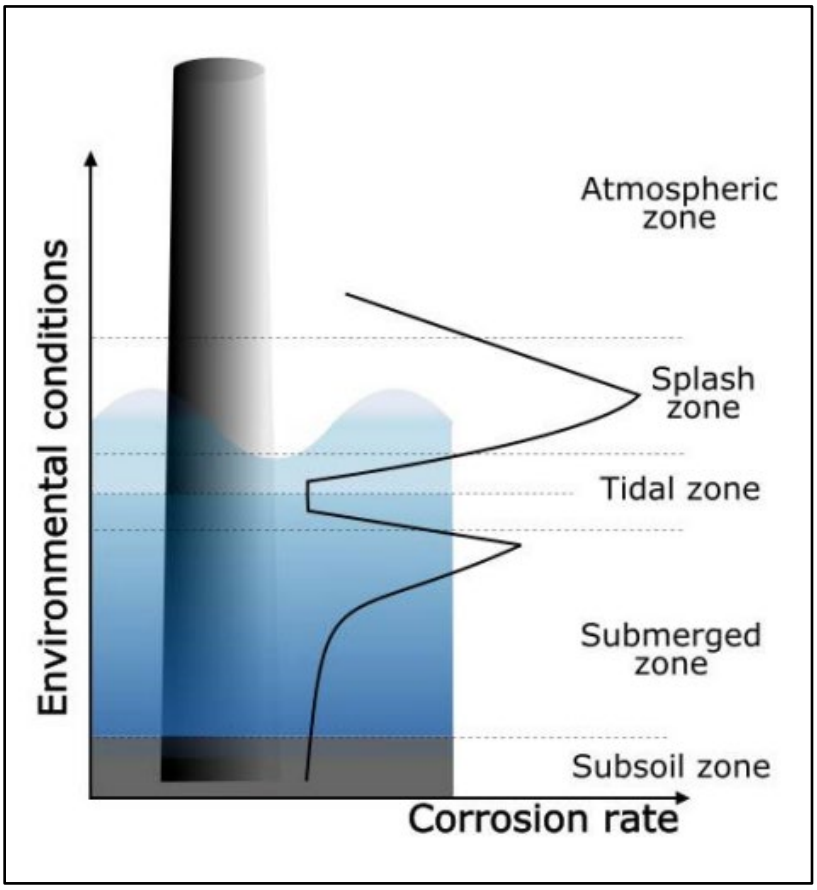

Figure 2. Corrosion Zones for a Seawater Environment. Source: [25].

A naval ship would naturally exist in all four zones depending on the sea conditions. The atmospheric zone, identified as the area of the ship that is exposed to sunlight, wind, spray, and rain, typically has greater protection than other zones due to a protective coating system, usually paint [26]. The typical corrosion rate for the atmospheric zone for an unprotected sample of steel ranges from 0.076–0.020 mm/year [27]. The most heavily attacked region of a ship would be found in the splash zone (0.20–0.50 mm/year), were the hull is wetted by waves and water spray and where any damage to a protective coating

would be found from docking and other exercises [25]. The tidal zone and submerged zone (0.1-0.2 mm/year) are infrequently exposed to aerated seawater, and with the addition of biofouling growth, the rate of corrosion can greatly vary [26].

3. 316-L Stainless Steel

The rate of corrosion for most stainless steels depends heavily on the material composition and the wt-% of Chromium (Cr) present. The wt-% of Cr present in the 316-L stainless steel to be used for experimentation, shown in Table 1, ranges from 17–19 wt-%, well over the 10.5 wt-% threshold for Cr needed to form a passive layer, preventing corrosion [28].

Table 1. Material Composition of EOS Stainless Steel 316-L. Adapted from [29].

Element	Material Composition	
	Min %	Max %
Fe	Balance	
Cr	17	19
Ni	13	15
Mo	2.25	3
C		0.030
Mn		2
Cu		0.50
P		0.025
S		0.010
Si		0.75
N		0.10

With a concentration of Cr greater than 10.5 wt-%, the metal is able to undergo passivation, defined as the loss of electrochemical reactivity experienced under particular environmental conditions [30]. The passivation process creates a protective film of chromium oxide on the surface of stainless steel, preventing direct contact with the environment. As shown in Figure 3, the passivation process allows for self-healing of stainless steel when the passive film is damaged, elongating the life cycle of the metal, a substantial difference when compared to mild steels that begin to corrode and rust when the protective layers are stripped away.

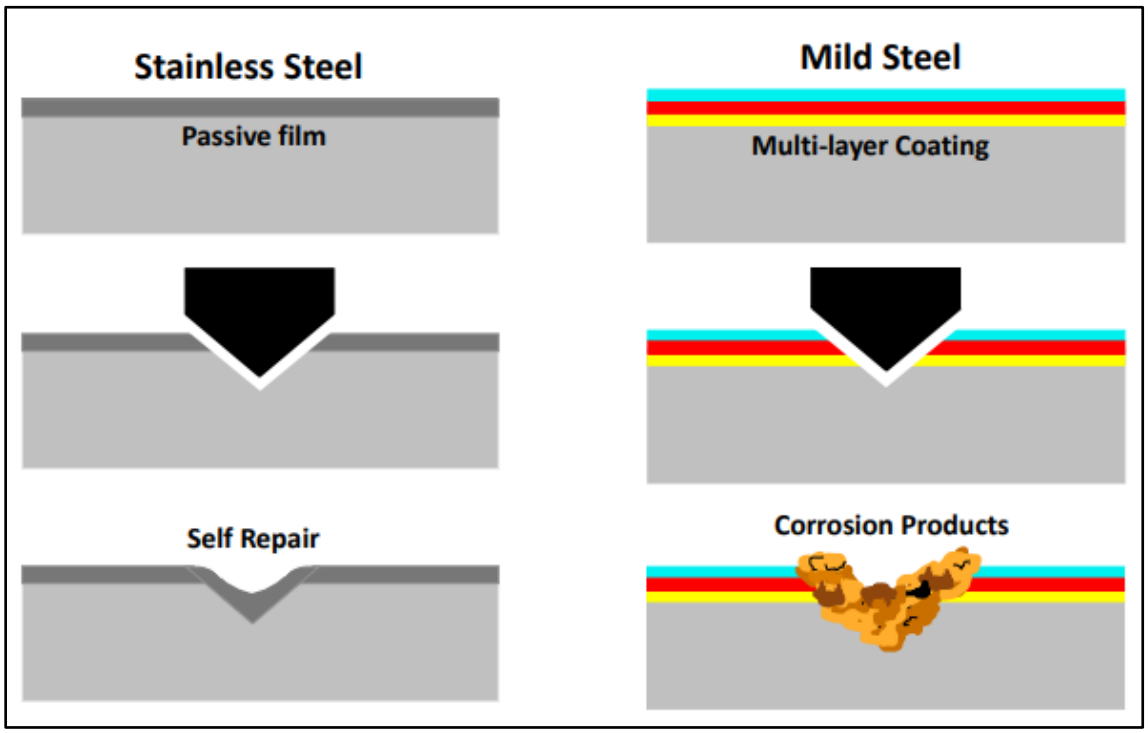

Figure 3. Self-healing Nature of Stainless Steel with a Chromium-based Passive Film. Source: [28].

While passivation cannot fully protect a metal from corrosion, the rate is greatly decreased. With the ability to self-repair after damage, restoring the metal surface almost to its original composition, the rate of corrosion for stainless steel without any additional environmental factors influencing the corrosion rate is approximately 0.001 mm/year, a significant decrease over standard carbon steel at 0.05–0.1 mm/year.

B. HYDROPHOBICITY

1. Wettability

All solid surfaces are subject to a certain level of wetting, defined as the "ability of a liquid to adhere and keep in contact with a solid surface," as a direct result of intermolecular attraction between two media-liquid and solid [31]. A painted object is a result of wetting and adhesion, the oil used in an engine to keep parts lubricated and moving is a wetting medium, and plants have adapted to maximize the wettability of leaves to ensure water is collected and the plant remains alive [32]. While the phenomenon of wetting is typically a liquid and solid interface, liquid trapped between two solid surfaces can create a solid-solid interface with strong bond, like a glue or epoxy bond [33]. With both liquid-solid and solid-solid interfaces, the strength of bond is strongly correlated to the surface's ability to attract or repel water. Water naturally possesses a certain attraction to itself, known as cohesion, resulting in rain falling as droplets instead of mist, as the water molecules pull together to form drops [34]. In addition to cohesive forces, water can also be subject to adhesive forces, defined as the attraction between unlike substances, resulting in water clinging to surfaces [34]. When water is present on the surface, both cohesive and adhesive forces are in action. A physical representation of cohesion and adhesion can be seen in Figure 4.

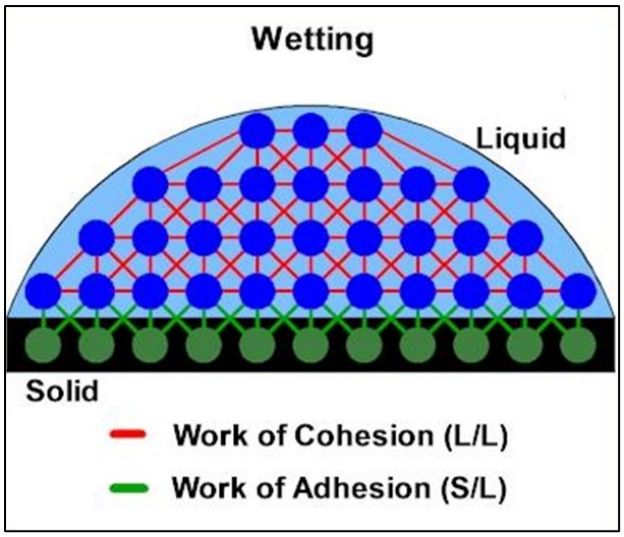

Figure 4. Cohesion and Adhesion of Water. Source: [35].

To determine which forces are stronger when water is present on a surface, a measurement of the contact angle of the water droplet must be made. Contact angle is "a measure of the surface energy present in a solid-liquid-vapor system," notably water in contact with a surface and air in the environment [36]. A measure of contact angle is initiated at the liquid-solid interface and measures out to the outer limits of the water profile, as seen in Figure 5. As the contact angle increases and surpasses 90°, the water drop would be considered to have stronger cohesive forces than adhesive forces. A true hydrophobic surface is considered when the average contact angle of water drops exceeds 90°, defined as a material with low wettability [37]. If the contact angle is less than 90°, the water drop has greater adhesive forces, wanting to spread along the surface and cling, meaning the surface has a greater wettability and is considered hydrophilic.

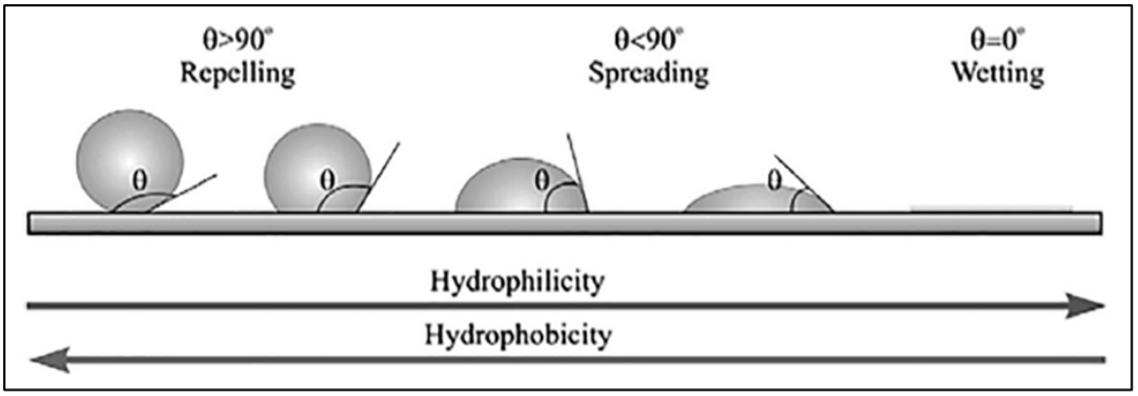

Figure 5. Measuring Contact Angle Based on Level of Wettability. Source: [37].

2. Governing Equations of Wettability

The concept of wettability is driven by three governing equations: Young's equation, Wenzel equation, and the Cassie-Baxter equation. The following equations are most used when the liquid found on a surface are water. For clarity, any variable with subscript letters 'L', 'S', or 'V' refer to liquid, solid, and vapor, respectively. Young's equation is the base for the two successive equations, as the Wenzel and Cassie-Baxter equations modifying the base equation and incorporating additional variables to determine the contact angle.

The base equation for determining the contact angle of a water droplet is Young's equation, defined as the following:

$$\cos\theta_Y = \frac{\sigma_{SV} - \sigma_{SL}}{\sigma_{LV}} \tag{1}$$

In Young's equation, θ_Y refers to the contact angle between the water droplet and the solid surface, σ_{SV} refers to the surface interaction within solid-vapor interface, σ_{SL} corresponds to the interaction between the solid-liquid interface, and σ_{LV} corresponds to the surface tension of the water drop with regards to the liquid-vapor interface [38]. The vapor referred to in the equation refers to the environment surrounding the water drop and solid surface, generally decided to be atmospheric air. The surface is assumed to be a smooth, planar, rigid, and homogeneous surface, as seen in Figure 6 [38].

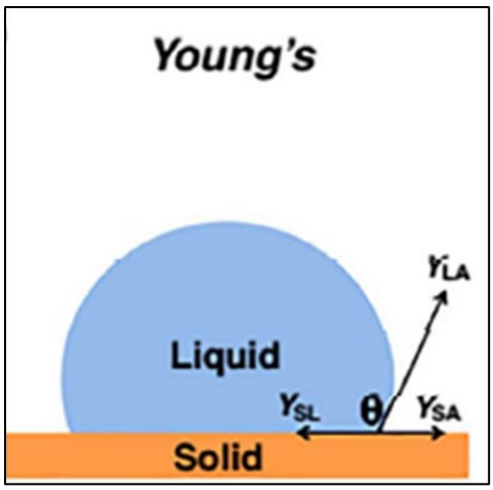

Figure 6. Model of Young's Equation and Surface. Source: [37].

Using Young's model, the determination of whether a surface is hydrophobic or hydrophilic is strictly dependent on the contact angle measured. If the liquid-liquid cohesion value is assumed to be uniform and standardized, the measure of contact angle is directly related to the difference in strength of surface tension between the solid-vapor relationship and the solid-liquid relationship. Due to limitations with producing truly smooth and homogeneous surfaces, modifications to Young's equations are required. To

model realistic surfaces with varying surface roughness, Young's equation was modified by Wenzel, resulting in the Wenzel equation [39].

The Wenzel equation differs from Young's equation by considering surfaces where the surface is not perfectly smooth. The surface roughness factor, a value greater than 1 and proportional to the actual surface area compared to the potential surface area, is added to the base Young's equation to create the Wenzel equation, defined in Equation (2) [37].

$$\cos\theta_W = \frac{r(\sigma_{SV} - \sigma_{SL})}{\sigma_{LV}} = r \bullet \cos\theta_Y \tag{2}$$

In the Wenzel equation, θ_W corresponds to the new contact angle when considering surface roughness, r is the surface roughness factor, and θ_Y is the initial contact angle calculated using Young's equation [39]. A visual representation of the Wenzel equation is seen in Figure 7.

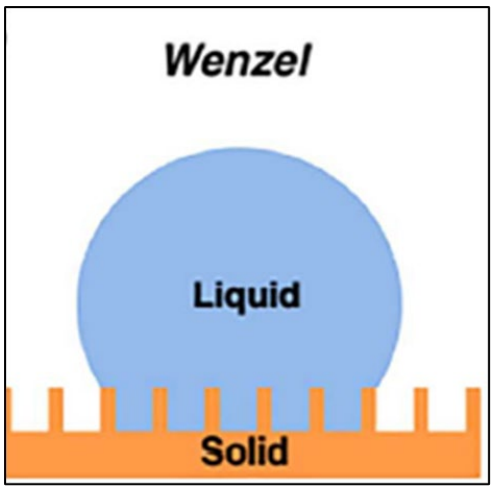

Figure 7. Model of the Wenzel Equation with Rough Surface. Source: [37].

The surface roughness factor has a great influence on the wettability characteristic of a surface. When considering surface roughness with a hydrophobic surface chemistry, an increase in surface roughness will result in an increase in the effective contact angle. Opposite to a hydrophobic surface, a hydrophilic surface chemistry would result in a

decrease in contact angle as the surface roughness increases [38]. The resulting circumstances for each situation are modeled in Figure 8, where a hydrophobic surface would effectively repel a water droplet towards the tip of a surface, minimizing the contact surface area, and where a hydrophilic surface would demonstrate the wicking effect as the water drop sinks into and coats the surface [40].

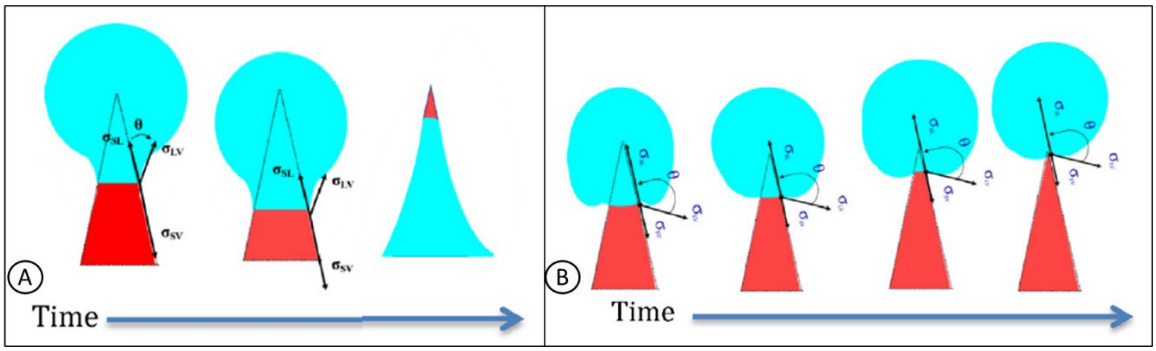

Figure 8. Wettability Mechanisms. Source: [38]. [A] Hydrophilic Surface Demonstrating Wicking Effect, [B] Hydrophobic Surface Demonstrating Water Rising to Minimize Contact Surface Area.

While the Wenzel equation and model applies to many wettability scenarios in a perfect environment, the inclusion of air pockets or voids in real-world applications requires another equation for proper modeling. To model the macroscopic liquid-air-solid interfaces when air pockets or voids are present on a perfectly smooth surface such as in Young's model, the Cassie-Baxter equation is used, defined in Equation (3) [41]. When surface roughness is included, known as the base Wenzel model, the Cassie-Baxter equation is modified, defined in Equation (4) [37].

$$\cos\theta_{CB} = f\cos\theta_{Y} + (1-f) \tag{3}$$

$$\cos\theta_{CB_{M}} = r \bullet f\cos\theta_{Y} + (1-f) \tag{4}$$

In these equations, the variable f represents the ratio of solid – liquid interface to the entire interface within the effective surface area, not accounting for any air pockets or void spaces [38]. A model representation of the Cassie-Baxter equation as modified for inclusion of surface roughness factor is seen in Figure 9.

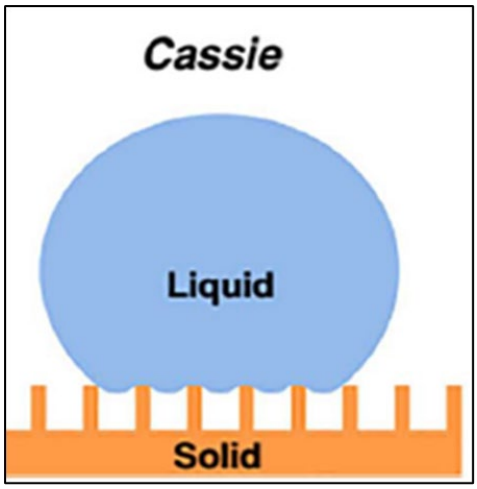

Figure 9. Model of the Cassie-Baxter Equation with Rough Surface. Source: [37].

3. Hydrophobicity in Nature

Many biological mechanisms and designs possess features to naturally enhance hydrophobicity for protection and survival. Commonly referred to as the "Lotus Effect," the adaptations of plant life and animals have created natural hydrophobic and superhydrophobic surfaces. A superhydrophobic surface is one where the effective contact angle of a water drop exceeds 150°, presented as an almost perfect spherical water droplet when placed on a surface. The hydrophobic surfaces of many plants are created using air pockets that are trapped within surface pores [42]. By anchoring to the interior walls of the pores, the air becomes trapped, forming a thin barrier between the plant and the water droplet. With the air barrier, the water drop "slips" along causing the "slip effect," resulting in a reduction of skin friction and causing the water drop to slide off the surface [42]. If the air barrier does not diminish through external forces, the hydrophobicity of the surface can remain indefinitely. Natural adaptations to maximize the trapping of air in near proximity of a plant and other organic material is especially critical in underwater applications, as the potential to trap new pockets of air is unlikely [42].

A plant that exhibits hydrophobic tendencies utilizing the trapped air method is the lotus plant, specifically the lotus leaf. Lotus leaves, when observed at a microscopic level,

are covered in epidermal cell papillae of varying height and size giving the leaves high levels of surface roughness, shown in Figure 10.

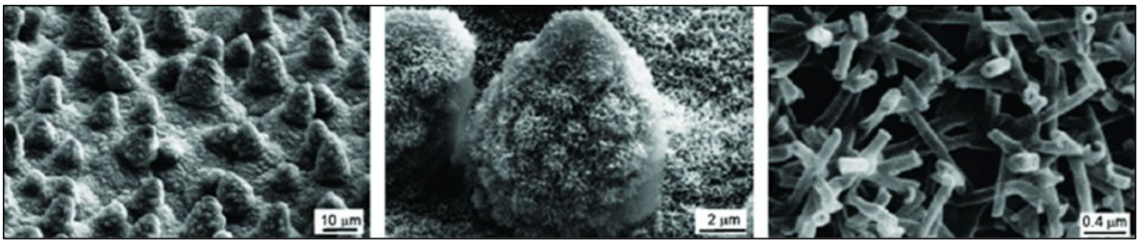

Figure 10. Scanning Electron Microscope Images of Lotus Leaf At Increasing Magnifications. Source: [42].

While the lotus leaves have a dense layer of wax coating the entire surface, providing a degree of hydrophobicity alone, the combination of the wax and papillae protrusions result in effective contact angles being measured to exceed 150°. The combination of the two hydrophobic factors results in the contact of water to a lotus leaf to resemble the model shown in Figure 11. In the figure, the tips of the larger papillae and the tension of the water drop produce repellent force (re) while some smaller papillae are in adhesive states (ad), and some papillae are in both states simultaneously, as seen at point (n) [43].

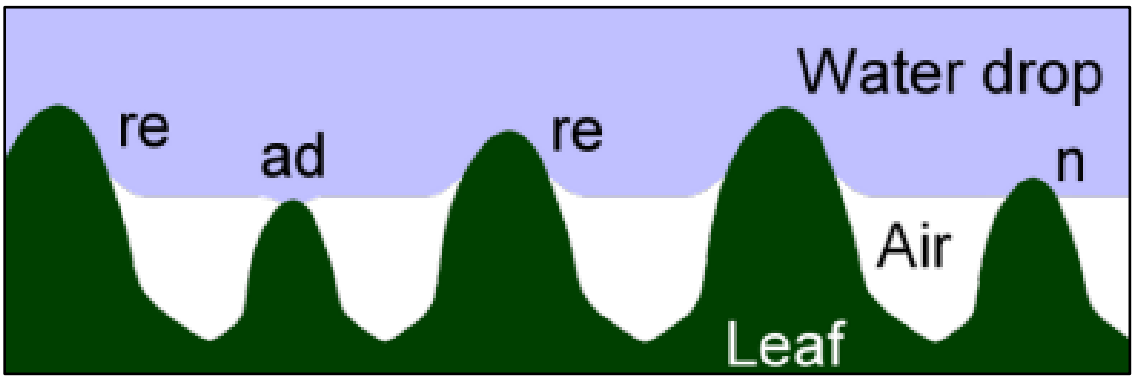

Figure 11. Hydrophobic Representation of Lotus Leaf with Air Barrier. Source: [43].

4. Chemically Engineered Hydrophobic Materials

The need for engineered hydrophobic materials ranges from uses in medical equipment to uses as a lubricant to trap insects and prevent escape. One of the most used hydrophobic materials found in all aspects of life is polytetrafluoroethylene (PTFE), also known as Teflon With exceptional material properties such as high chemical and temperature resistance, high electrical insulation power, high durability, and anti-adhesion and low water absorption, this hydrophobic material can be found in cookware, fabrics, aerospace components, medical equipment, military equipment, and 3-D print polymers [44], [45]. While Teflon can be very useful in many situations, concerns for chemical components leeching from the plastic material prevents certain applications. In addition to this, the scale and types of parts coated or created using Teflon is limited due to the high temperature sintering process required to coat an object.

To coat materials that would not withstand the sintering process required to provide a PTFE coating, a fluorosilane or other silane coating can be used. Fluorosilane has been proven to enhance a polymers ability to endure heat, light, flame, moisture and chemicals, similar to Teflon, without requiring a sintering process or other complex application process [46]. With the ability to be brushed on to a surface and create a hard coating, fluorosilane can be used to coat both organic and inorganic materials and increase the effective contact angle to greater than 90° in materials such as marble, stone, wood, glass, silicone and brass [46]. However, the practical application of fluorosilane coatings is limited due to the high toxicity factor to humans. Due to this, investigation into machined surfaces for the creation of hydrophobic surfaces is required.

5. Fabricated Hydrophobic Surfaces

The creation of a hydrophobic surface on a bare metallic or composite surface has been proven possible utilizing chemical etching, laser etching, or additive manufacturing with hydrophobic characteristic enhancing geometries.

a. Etching

Two forms of etching are possible for the creation of hydrophobic surfaces: chemical and laser. Chemical etching requires an acidic or basic solution to be applied to the surface, where the solution etches any dislocation or surface impurity, creating a higher surface roughness. This etching technique is inexpensive and can be scaled greatly, but is limited in use due to hazards and environmental concerns [37].

Laser etching, also known as laser ablation, is also widely used for the creation of hydrophobic surfaces. A much safer, faster, and more automated process, laser ablation affects the surface of a material in small pulses with a small point of contact, focusing energy. The focused beam of energy is absorbed by the material, heating and melting/evaporating the point of contact, leaving a void in its place [47]. The process of laser ablation for the creation of higher surface roughness and a more hydrophobic surface may be seen in Figure 12.

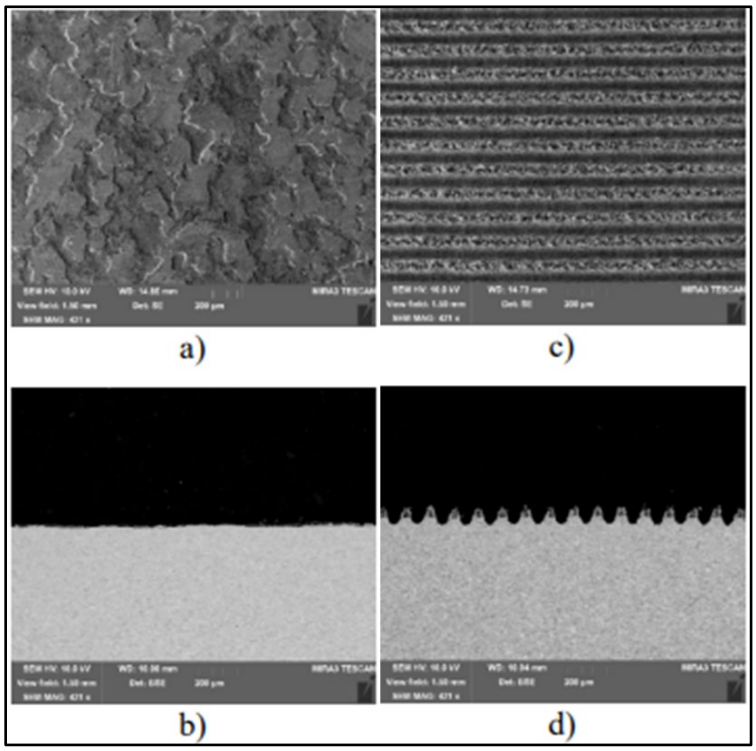

Figure 12. Laser Ablation of Galvanized Steel. Source: [47]. [A], [B] Initial State. [C], [D] After Laser Ablation.

b. Additive Manufacturing

Template-based methods of additive manufacturing though casting with the addition of an external polyaniline (PANI) has been proven to create hydrophobic surfaces. By using naturally hydrophobic surfaces such as leaves and reptile skins, molds can be taken using polydimethylsiloxane (PDMS) as a coating. Using the process shown in Figure 13, the PDMS template can then be used to create a PANI film, which can be used in casting processes. When the final part is cast and cooled, the template is either removed or dissolved if damaged, allowing for low cost, fast, and repeatable procedures [37].

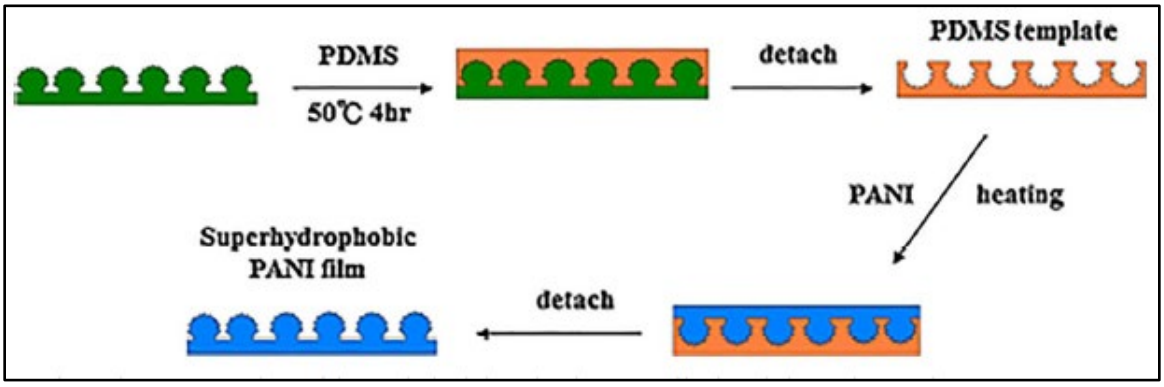

Figure 13. Hydrophobic Surface Templating Process. Source: [37].

In addition to templating technology, advanced in 3-D printing additive manufacturing have shown promise in the creation of hydrophobic surfaces. In an experiment conducted by Budan [48], promising results were gathered after 3-D printing stainless steel and carbon nanotube composite powders using selective laser melting (SLM) processes. With further experimentation and modifying the composite powder to replace carbon nanotubes with graphene nanoplatelets, there is potential for the creation of another hydrophobic surface.

C. GRAPHENE NANOPLATELETS

1. Graphene

Graphene, the origin for all other graphitic derivatives, is a unique hexagonally structured two-dimensional carbon material with highly desired mechanical properties [49]. A single layer of graphene, considered the thinnest material on earth with a thickness of one carbon atom (0.34 nm), possesses incredible strength relative to its size and weight [50]. Graphene is also considered one of the strongest materials discovered, with an average ultimate tensile strength (UTS) of 130 GPa [51]. Additionally, graphene is extremely light, weighing only 0.77 milligrams per square meter, as compared to roughly 80 grams per square meter for standard printer paper [51]. In its hexagonal honeycomb atomic structure, as seen in Figure 14, graphene has other extraordinary physical properties, as seen in Table 2.

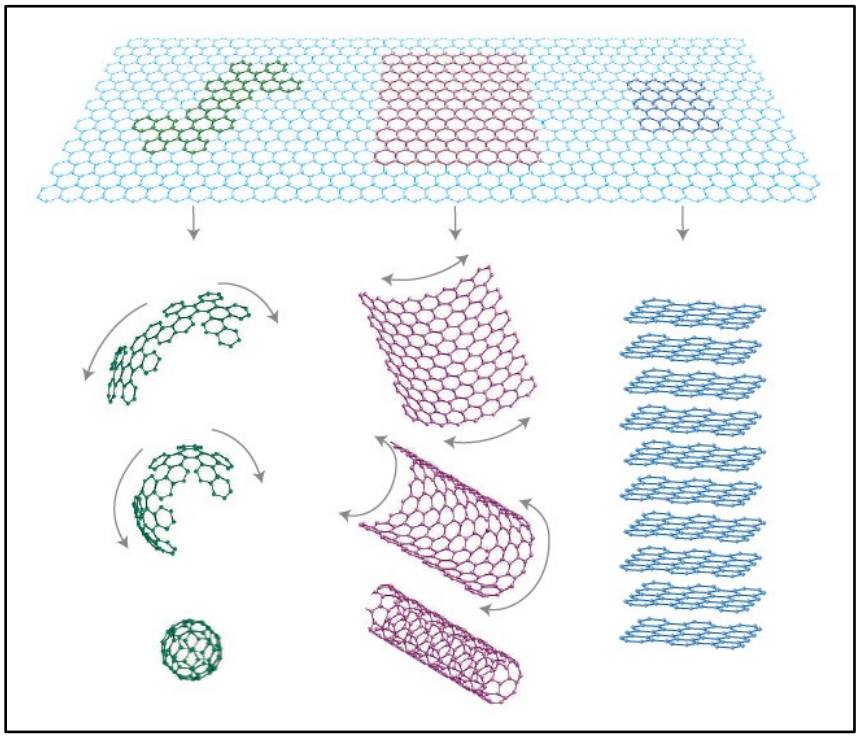

Figure 14. Graphene as a 2-D Building Material for All Other Dimensions and Shapes. Source: [52].

Table 2. Physical Properties of Graphene [50], [53].

Physical Property	Value
Young's Modulus	0.5 – 1.0 TPa
Thermal Conductivity	5000 W/mK
Surface Area	2630 m^2/g
Electron Mobility	250000 $cm^2/(Vs)$
Appearance	Transparent (97.7%)
Density	1.9 -2.2 g/cc
Melting Point	>3600°C

Graphene sheets are prepared using a micromechanical cleavage process on highly oriented pyrolytic graphite using tape and depositing the layers to a silicon substrate [54]. While this process is very exact and can provide small samples of single layer graphene, micromechanical cleavage is not scalable for large scale production of single or multilayer graphene sheets. To increase production capabilities while maintaining the physical properties of single layer graphene, other forms of synthesis of graphene are needed, leading to the production of graphene nanoplatelets.

2. Synthesis of Graphene Nanoplatelets

Graphene nanoplatelets (GNPs) are a low-cost alternative to single layer graphene. GNPs are collections of many single layers of graphene, normally ranging from 0.7 – 100 nm (roughly 2–300 layers), as seen in Figure 15 [50]. Possessing the same physical and mechanical properties of graphene, GNP particles can be found in many current and future applications such as sensors, energy harvesting adsorbents, etc., earning its place as one of the leaders in nanofiller technologies [50].

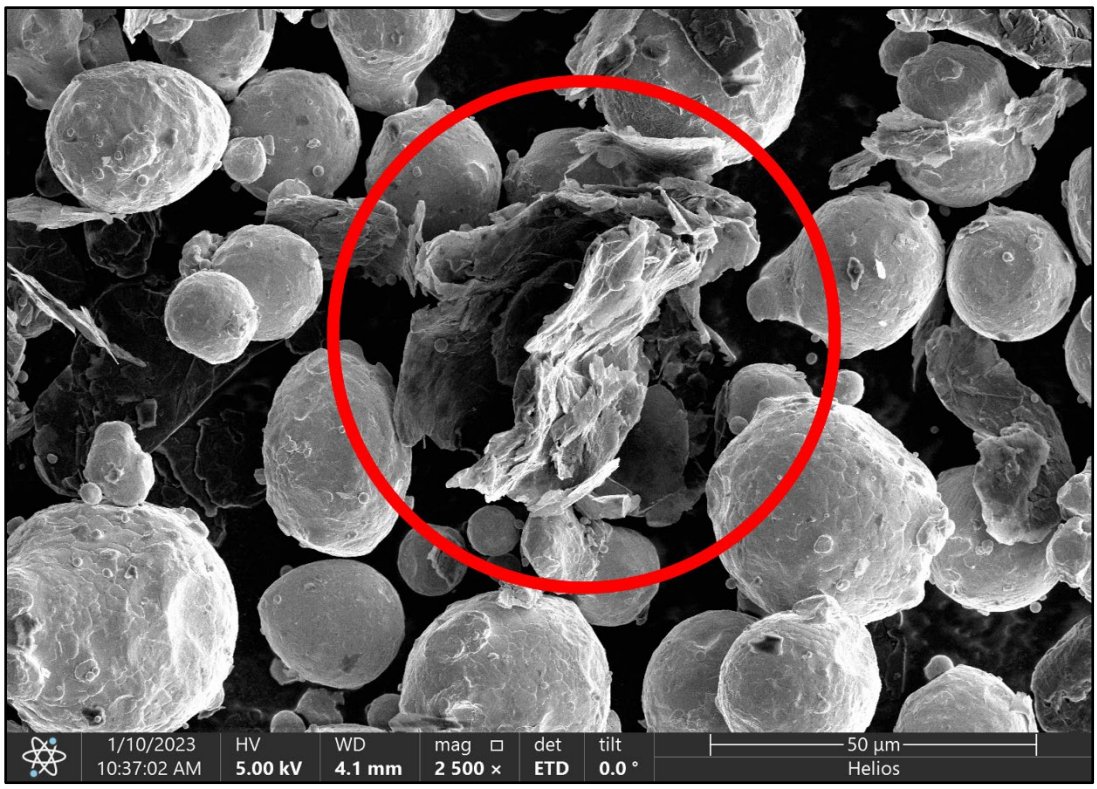

Figure 15. SEM Image of Graphene Nanoplatelet at 2500x Magnification Highlighting the Many Graphene Layers

Three methods of GNP synthesis are heavily researched to enhance and maximize the production capabilities: ball-milling graphite, water exfoliation and electrochemical exfoliation. The process of ball-milling graphite works by adding graphite and chemical reactants to a chamber. Reactions within the chamber during the milling process creates large amounts of hydrogen gas and heat, generating enough energy to break C – C bonds as well as the inter-layer bonds [55]. This process requires further research as the potential for the bonds to reform over time is greater than preferred, and this process is time-consuming and can be hazardous with the chemicals used. A secondary method to the synthesis of GNPs is utilizing an aqueous graphite solution and the process of sonication. By adding graphite powder to pure water and subjecting the solution to sonication at high power and then baked and stirred to create a slurry. This process was then repeated and then dried over 24 hours to create bulk-layered graphene nanoplatelets [55]. This method of exfoliation is successful at producing the desired size and thickness of platelets, resulting

in a low-cost and mass production potential of GNPs, with the only drawback being the requirement to repeat the sonication and drying process more than once to maximize the yield. One final method for the synthesis of GNPs is electrochemical exfoliation, like the ball mill water exfoliation method but with a higher yield. Using chemicals and mechanical stirring, a complete chemical reaction occurs over a 3- to 4-hour period, requiring washing, filtering, and drying of the graphene particles. Tests show that 100 mg of graphite can yield up to 105 mg of GNPs, a ~100% yield [56].

3. Graphene Nanoplatelets as Material Surface Modifiers

Many uses for stainless steels and other materials require the material to possess qualities that prevent corrosion, unwanted bio growth, and other potential dangers while enhancing the natural physical properties of the material. In an experiment by Hu *et al*. [57], graphene and graphene nanoplatelets were utilized for the creation of an antimicrobial paper product. The results from the experiment showed great promise, as bacterial cultures were effectively eliminated after short incubation periods on the graphene-infused paper [57]. Additionally, in an experiment by Zhou *et al*. [58], chemical vapor disposition was used to adhere graphene nanoplatelets to the surface of 316 biomedical stainless steel instruments resulting in promoted growth of bone marrow cells on the 316 biomedical stainless steel. Graphene nanoplatelets have been used in experimentation by Song *et al.* in the creation of hydrophobic surfaces using surface laser processing and polymethylmethacrylate–graphene transfers, as seen in Figure 16.

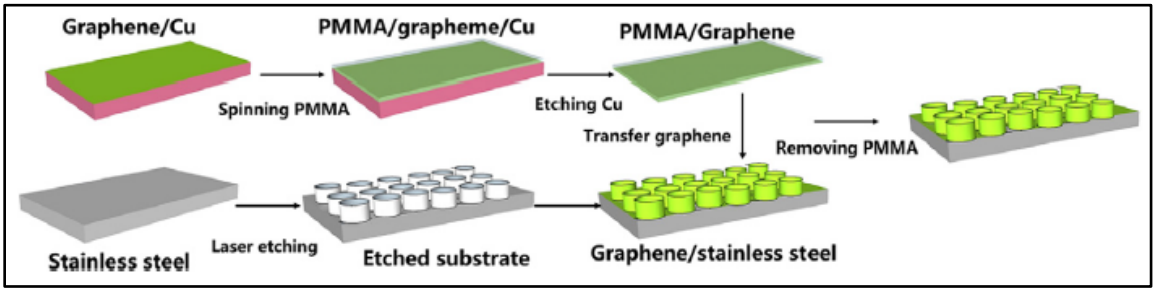

Figure 16. Transfer of Graphene Film to Create Hydrophobic Surface. Source: [59].

D. 3D METAL PRINTING

1. Metal Additive Manufacturing

Additive Manufacturing (AM) encompasses all technology used to produce objects through addition rather than the industry standard of removing material [60]. Otherwise known as 3-D printing, AM initially comprised fabrication of objects using plastic filaments extruded through heated nozzles. As technology advanced and the need for more robust parts grew, the adaptation of AM technology to cater towards metals was required. With the printing of metals, normally in powder form, there are generally no geometric limitations, allowing for increased product performance, reduced costs, improved efficiency, and more sustainable products and processes [60]. Industry has adopted many of the same forms of additive manufacturing for metal AM, ranked by prevalence in the market, with laser powder bed fusion (L-PBF) AM leading the industry [61]. While all methods of metal AM differ slightly, there is a general chain of events that must happen to process a model into a physical part, as seen in Figure 17.

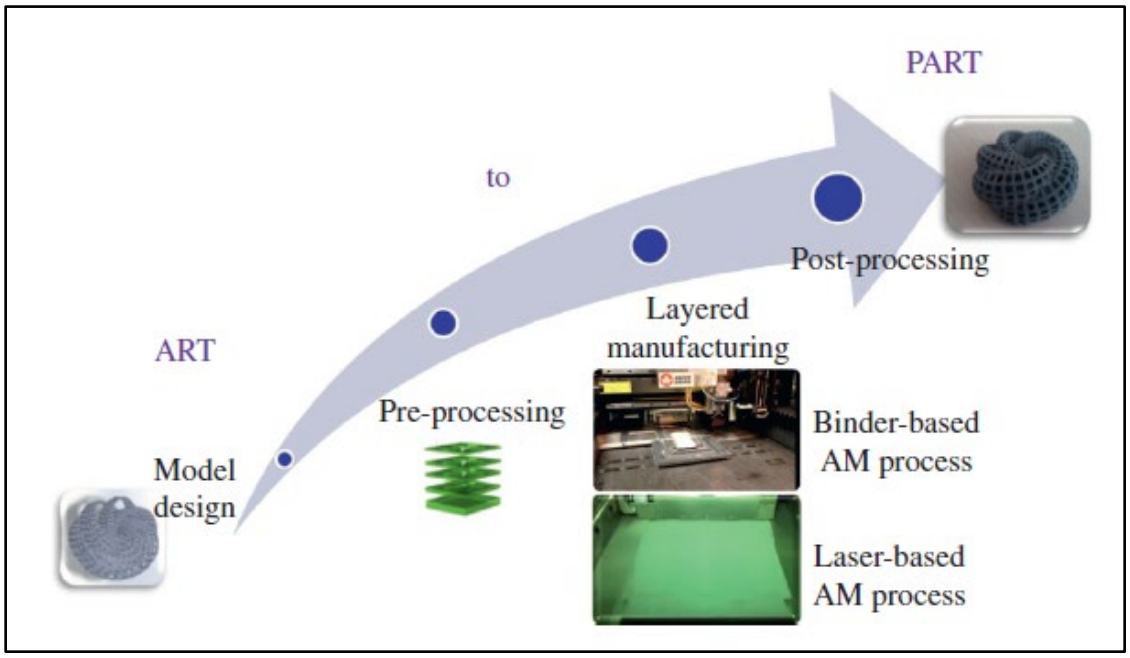

Figure 17. Metal Additive Manufacturing Chain from Design to Part. Source: [61].

As technology advances and the need for more complex objects are needed in a quicker fashion, the traditional method of creating objects through subtractive manufacturing cannot keep pace. Although it is projected that the status of AM will be unrecognizable in 5–10 years' time, the desire to understand and utilize technology now is what will drive the future success and innovation of the technology. Many motivations drive the industry forward, namely: on-demand low-cost prototyping, simplified supply chains for low-volume production, freedom of geometric complexity, lightweighting, parts consolidation, and crisis supply prevention [61]. With the power to address all the common issues found in traditional manufacturing, the presence of metal AM continues to grow globally, increasing the need to understand and be able to fully utilize the technology.

In 2019, the total additive manufacturing market was roughly $11 billion, with metal AM accounting for roughly 20% of that value at $2.4 billion [61]. Projections see the total value of the AM market to be $42 billion by 2027, with metal AM increasing to roughly $8 billion. Currently metal AM is found in many highly technical and sensitive industries, including the medical and dental industry, aerospace and national defense, communications technology, and energy and resource industries [60]. Within the United States military, there is a strong push for the adaptation of additive manufacturing within all aspects of life. From defense contractors designing equipment that can be easily repaired with 3-D printers located in military bases to naval ships being outfitted with printers to replace damaged or lost tools, the influence of metal AM is only growing within the defense industry.

2. Laser Powder Bed Fusion

Laser Powder Bed Fusion (L-PBF) additive manufacturing systems are one of the most common forms of metal AM. Most forms of L-PBF printing require the use of a laser, automatic powder depositing apparatus, a process controller, and additional support systems such as inert gas protection and a pre-heating system [62]. While there are many forms of L-PBF printing, the physical composition of all the printers is similar, as seen in Figure 18.

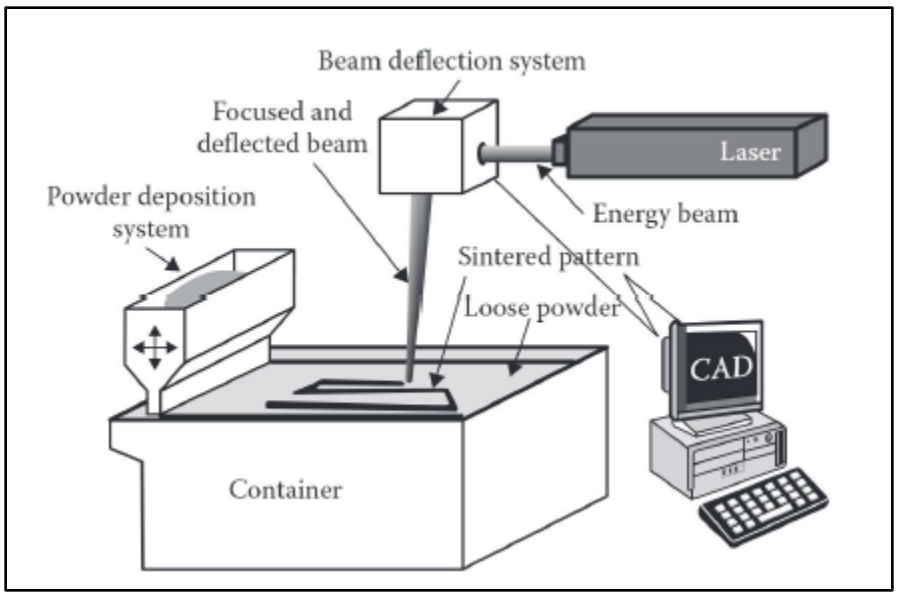

Figure 18. Laser Powder Bed Fusion Processes. Source: [62].

The most important component of a L-PBF system is the laser, as this is the direct energy source used to melt and sinter the powder into the desired part. Normally utilizing a continuous wave Ytterbium-doped fiber laser, L-PBF systems control the laser as a source of thermal energy to create the layer-by-layer geometry, creating a finished part [63]. Depending on the powder material being used and the desired quality of the finished part, the strength of the laser as applied to the powder bed may require adjusting. By adjusting one or many of the parameters used when sintering the powder within the powder bed, the energy density of the laser is modified, as defined in Equation (5) [64].

$$ED = \frac{P}{VHW} \tag{5}$$

In Equation (5), ED represents the energy density that is applied directly to the powder bed (units J/mm^3), P represents the power provided to the laser (W), V represents the velocity of the laser moving across the powder bed (mm/s), H signifies the layer height of the powder deposited after each laser raster, and W indicates the hatch spacing of the sinter weld pool formed [64]. It is important to balance all the parameters when adjusting the energy density, as too high of a power with too low of velocity could lead to keyholing, where the laser melts deeper than necessary, or a lower power value and higher velocity

could lead to incomplete sintering known as the balling effect [65]. A representation of the balancing required for a properly sintered print is provided in Figure 19.

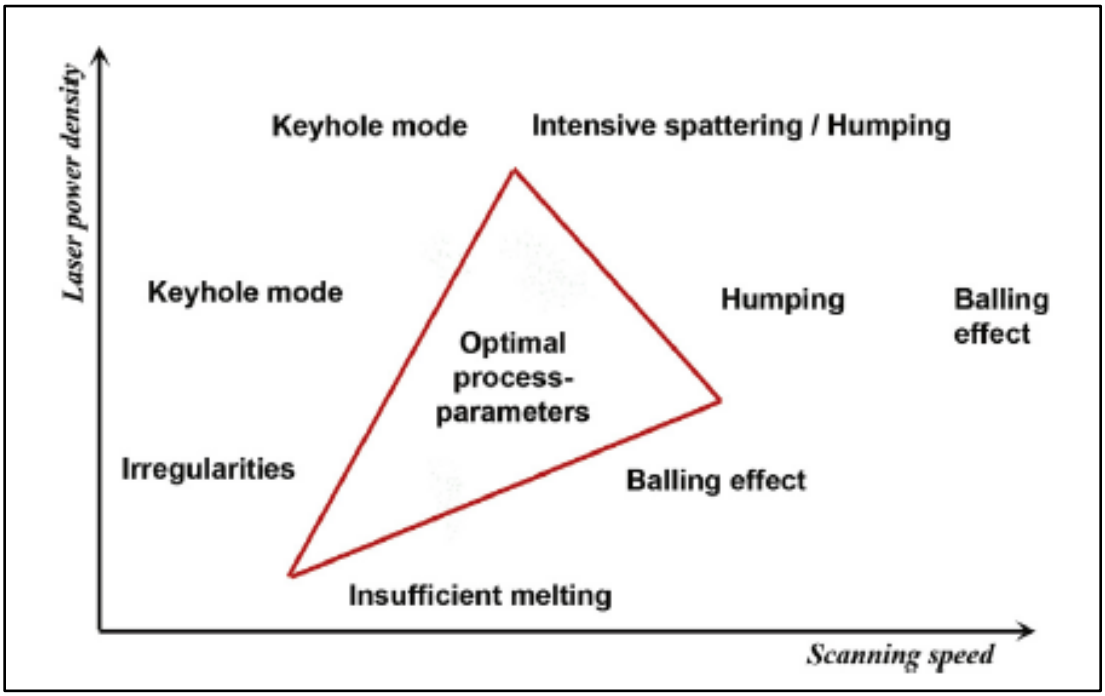

Figure 19. L-PBF Operational Parameter Processing Map. Source: [65].

THIS PAGE INTENTIONALLY LEFT BLANK

III. EXPERIMENTAL METHODS

A. HIGH ENERGY BALL MILLING PROCESS

To incorporate the graphene nanoplatelets into the stainless-steel powder to create the composite powders, the SPEX Sample Prep high energy ball mill (HEBM) machine was used. The HEBM, shown in Figure 20, operates by mixing samples using grinding elements, normally stainless steel balls, and imparting a figure-8 motion to the container [66]. For the milling process, sample canister was filled with 50g of composite powder along with 10g of 3mm diameter stainless steel balls, a ball-to-powder (BPR) ratio of 1:5. The composition of each powder that was used in the milling process varies based on the volume percent of GNPs added to the stainless steel powder, seen in Table 3 alongside the other operational parameters used. In calculations, the density of 316L stainless steel was determined to be 7.98 g/cm^3 [29] and the density for the GNPs being 2.2 g/cm^3 [53].

Figure 20. SPEX Sample Prep High Energy Ball Mill.

Table 3. HEBM Parameters for Powder Preparation

Composite Powder	Time On | Off	Number of Cycles	Ball: Powder Ratio	Mass 316L-SS	Mass GNP	Total Mass
1%-GNP SS	5 | 5 minutes	5	1:5	49.86 g	0.14 g	50 g
2%-GNP SS	5 | 5 minutes	5	1:5	49.72 g	0.28 g	50 g
3%-GNP SS	5 | 5 minutes	5	1:5	49.58 g	0.42 g	50 g

After the milling process was complete, the powders were removed and passed through a sieve to catch the stainless-steel balls and stored in glass jars to prevent moisture accumulation or contamination. To enhance the moisture prevention of the powders, the jars were then stored in a Quincy Lab Model 40 lab oven set to 75 °C, shown in 0. Samples of the powder were taken after the completion of the complete HEBM process for each composite powder and were subjected to scanning electron microscopy (SEM) to verify even distribution of GNPs throughout the stainless-steel powder.

Figure 21. Quincy Lab Model 40 Lab Oven. [A] External View of Oven, [B] Stainless Steel-GNP Powders Stored in Oven.

B. EOS M100 3D PRINTING PROCESS

1. Model Development

The two CAD geometries used for printing the stainless steel and GNP composite samples were developed during another experiment and adapted for this thesis. To create the geometries, SolidWorks computer-aided design (CAD) software was used with the limitations of the EOS M100 printer in mind. Due to the resolution limits of the M100 printer, the sample geometry was sized to prevent any printer failure due to too sharp of edges or too complicated of shape. The sample size and shape were determined to be squares with rounded edges, a larger square that is 20 mm x 20 mm and a smaller square that is 10 mm x 10 mm. The height for both samples is 2 mm. The final CAD models used, as developed in SolidWorks, are shown in Figure 22.

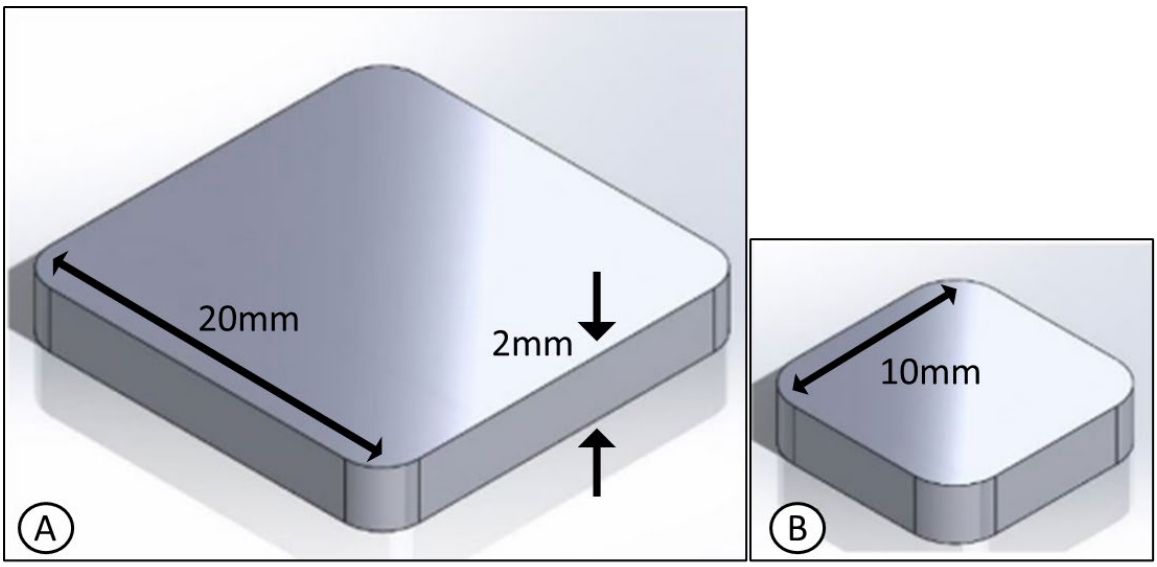

Figure 22. SolidWorks Sample Models [48]. [A] Large Sample, 20 mm x 20 mm, [B] Small Sample, 10 mm x 10 mm. Source: [48].

These chosen geometries were very successful during the printing process, maintaining the desired shape and integrity. During the machining process to remove the samples from the build plate, slight deformation in the corners of some samples was recorded. The deformation of the corners did not prevent any further experimentation. Examples of the printed samples are shown in Figure 23.

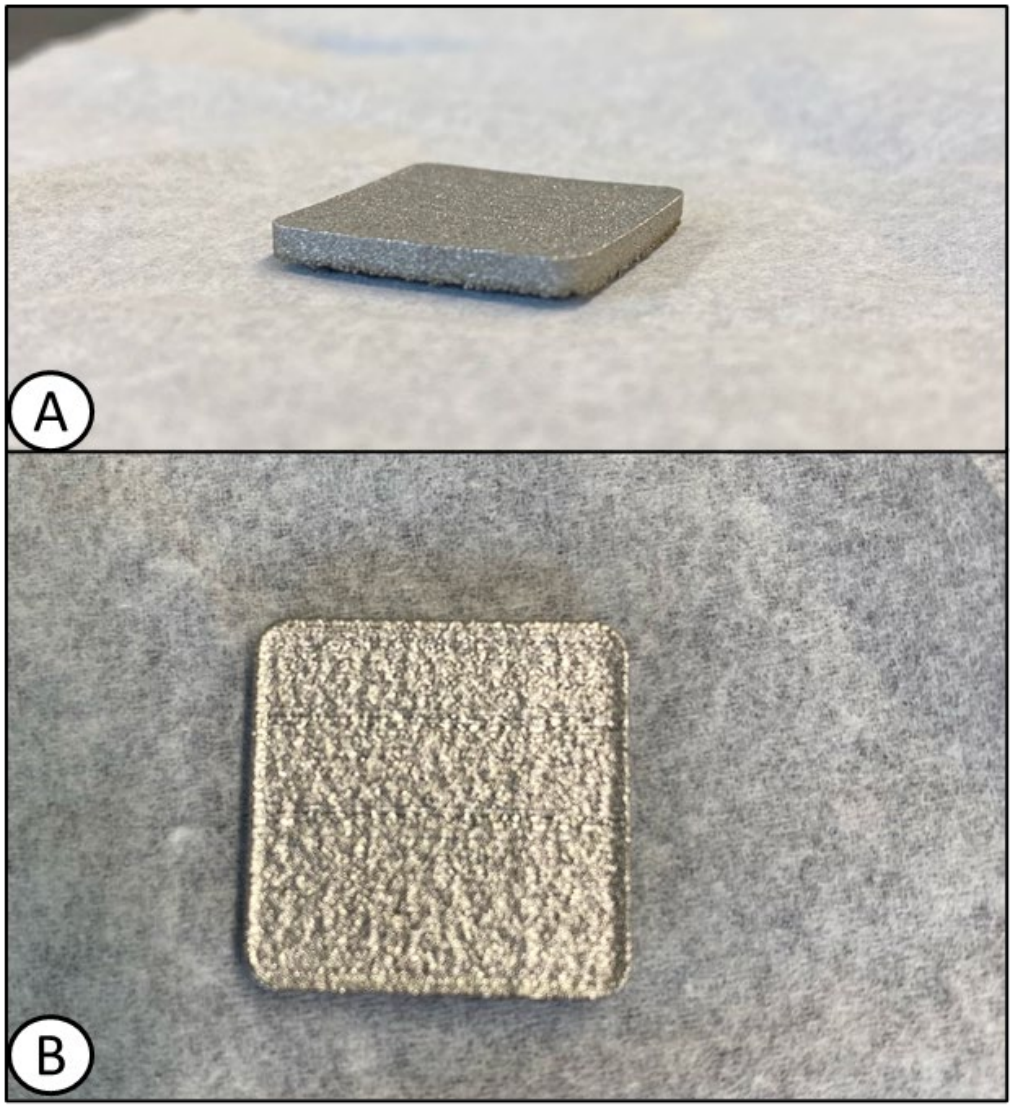

Figure 23. Successfully Printed Samples. [A] Side View, [B] Top View.

2. Materialise Magics

Due to the nature of the SLM additive manufacturing process normally requiring post-processing to remove a printed structure from the build plate, support structures were added to the build process to allow for a machining process to remove the final parts. Materialise Magics, a build preparation software program, received the imported CAD files, allowing for proper manipulation to allow for the printing process to begin. The software was configured to work alongside the EOSPrint software, providing a build area equivalent to the physical build area found in the EOS M100 printer. For each energy density selected, four samples were printed, two large squares and two small squares. To maximize the build area and limit the number of iterations of prints needed to complete all the needed samples, the build plates were optimized to fit as many samples as possible. To ensure that all samples were consistently coated with the print powder after each coating cycle, the samples were oriented to be placed closer to the left end of the build area where the recoating blade originated. With the number of samples chosen and arranged to ensure there was no overlap or overhang, supports were added to lift the sample off the build plate to allow for post-processing. In addition to automatically generated supports, cone supports were added to provide a greater adherence to the build plate and support future layers to prevent drooping. As seen in Figure 24, up to four sets of different energy density samples were able to be printed at a time, with the standard supports highlighted in blue and the cone supports found equally spaced throughout the samples. The build area in the software is oriented the same as the EOS M100 printer, where the left-hand side of the build area is the front/beginning of the build process.

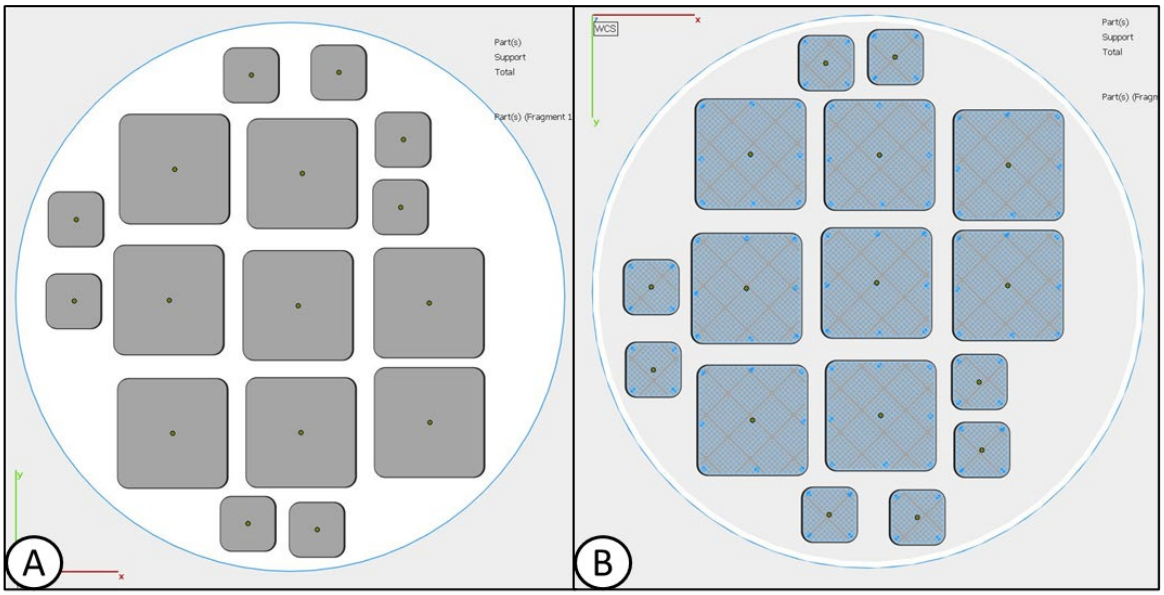

Figure 24. Materialise Magics Build Preparation Area. [A] Top-view of samples within the build area, [B] Bottom-view of supports and cones.

After failures during the print process due to the recoating blade catching the edge of the prints, further modifications to the sample orientation were implemented. To prevent the blade from catching the print, a five-degree tilt was added to the samples and supports, shown in Figure 25.

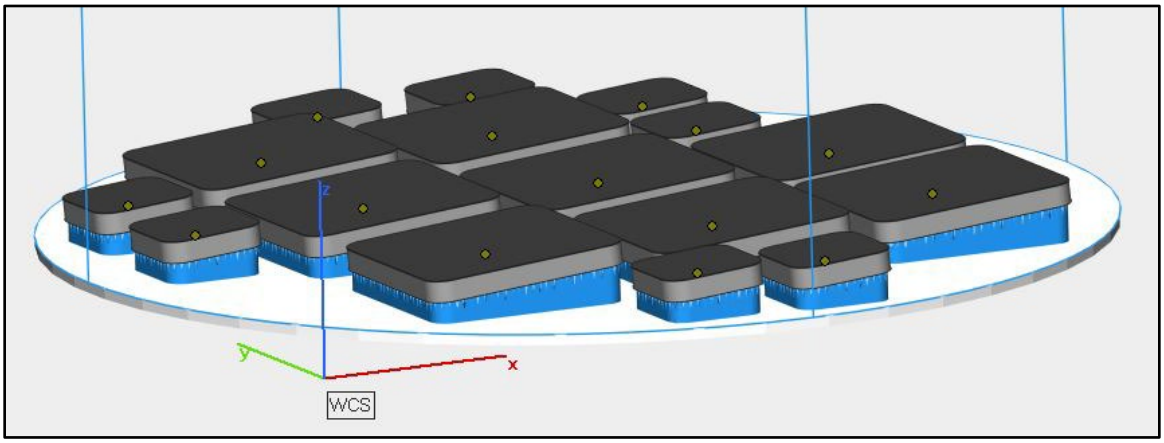

Figure 25. Materialise Magics Build Preparation Area Showing 5-degree Tilt of Samples.

3. EOS Software

After the modifications needed for the samples and supports were completed in Materialise Magics, the EOSPrint software was utilized to finalize the parameters needed for the printing process. The default settings for energy density for printing 316-L stainless-steel on the EOS M100 printer was found to be 67 J/mm^3. For testing differences in the print quality, samples on the same build plate were printed at different energy densities ranging from 60 J/mm^3 to 100 J/mm^3. The parameters modified to create each of the different energy densities are shown in Table 4, calculated using Equation (5).

Table 4. Laser Energy Density Parameters

Energy Density [J/mm^3]	Power [W]	Speed of laser [mm/s]	Hatch Spacing [mm]	Thickness [mm]
60	77.1	917	0.07	0.02
67 (Default)	77.1	827	0.06	0.02
80	76.8	800	0.07	0.02
90	76.8	711	0.06	0.02
100	79.8	665	0.06	0.02

These values were applied to two of three laser parameters used when printing a part: stripes and upskin. By altering these parameters, the print process ensured that the base and top layer of each sample was printed at the required energy density. The parameter that was not modified, downskin, applies to the initial support structure and was unchanged as there was not a necessity for higher quality support. When the downskin parameters were altered for experimental purposes and a print process was started, the print began to fail starting at the supports and would not continue to the actual part.

One last important step that was taken while using the EOSPrint software was found within the 'Job Parameters' section. To ensure that the support structures would print as required, it was necessary to modify the arrangement of files that determine when each component of a part is printed. Within each part, three files were created by the Materialise Magics software: the part, the support wall file, and the support volume file. To ensure that

the supports would print, providing a base for the parts to be printed, the order of files had to be rearranged to ensure that the support files were both placed before the part file.

4. EOS M100 Printer

The SLM metal printer used for this experiment was the EOS M100, a product of Electro Optical Systems. The technical data for the EOS M100 include a Ø100 x 95 mm build volume with a ytterbium (Yb) fiber laser with a maximum power of 200 W and a laser scanning speed up to 7.0 m/s [67]. The EOS M100, seen in Figure 26, is capable of printing with special EOS brand cobalt chrome, titanium, tungsten, and stainless steel 316L powders [67].

Figure 26. EOS M100 Printer.

Within the casing are the components needed to complete a print, as seen in Figure 27. Each of the labeled components are critical to the smooth operation of the printer and a successful print.

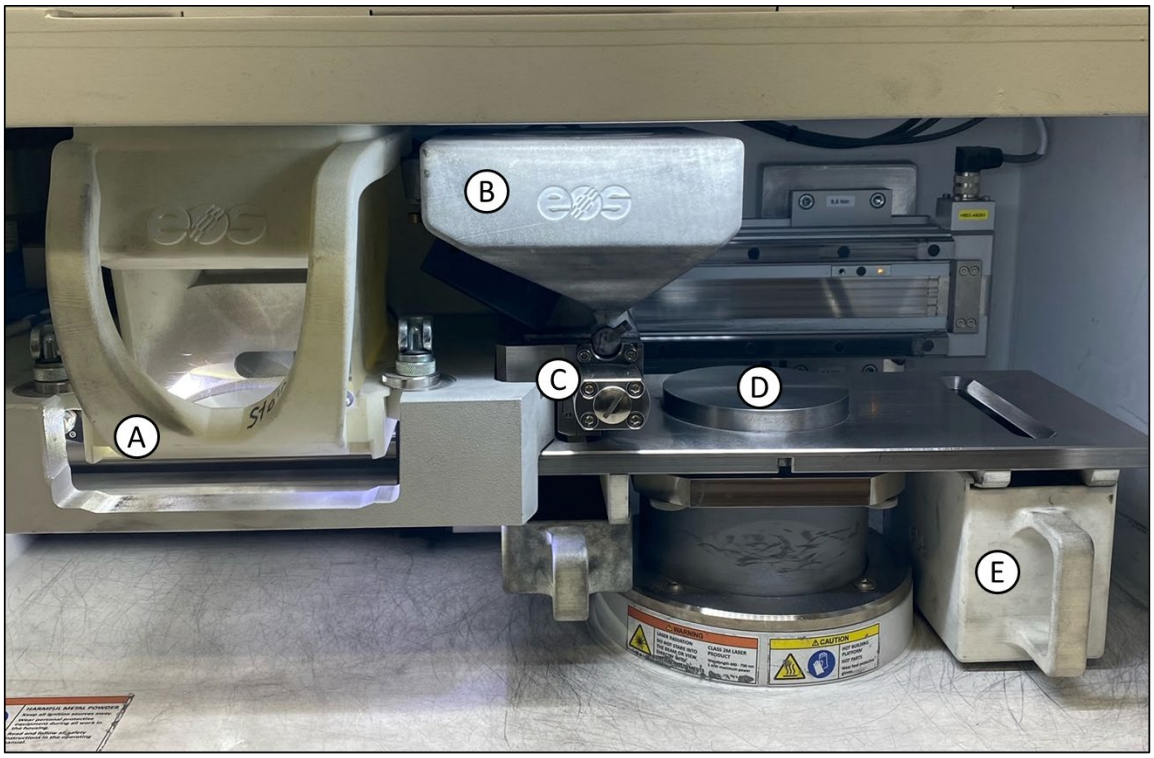

Figure 27. Internal Components of EOS M100 Printer. [A] Air Guiding Flow Box, [B] Powder Hopper, [C] Powder Distribution and Recoater Blade Assembly, [D] Build Plate, [E] Excess Powder Collection Containers.

The air guiding flow box [A] is necessary during the laser sintering process, as the exhaust ports pull a suction over the build plate using the argon supplied to the printer to remove any burned metal particles or other contaminate byproducts resulting from the sintering process, ensuring a high-quality print. To supply the powder for the print, the hopper [B] is utilized. Within the powder distribution assembly [C], the powder dispensed by the hopper travels through a revolving set of containers that are rotated and poured in front of the recoating blade as the print process requires. The recoater blade travels across the build plate, leaving a very thin layer of powder for the metal powder sintering process. After each iteration of the sintering process, the build plate lowers roughly 0.02 mm into the build volume cylinder to control the layer height of powder that coats the top layer of the sinter process. To collect unused and reusable powder, the collection containers [E] are located on each end of the print area, ensuring that powder is collected during the forward and backward travel of the recoater blade.

In preparation for a print to begin, the recoater blade and build plate height needed to be set to ensure the print would be a success. It was determined that using a build plate height of 30 µm with a recoater blade height of 32 µm above the base of the printer area resulted in consistent successful prints. To do this, as seen in Figure 28, a dial indicator was used to set the build plate to 32 µm above the base, where the recoater blade was then adjusted by setting it to the base of the build plate. After this, the build plate was lowered 1–2 µm to allow for the slight initial gap, resulting in a high-quality print.

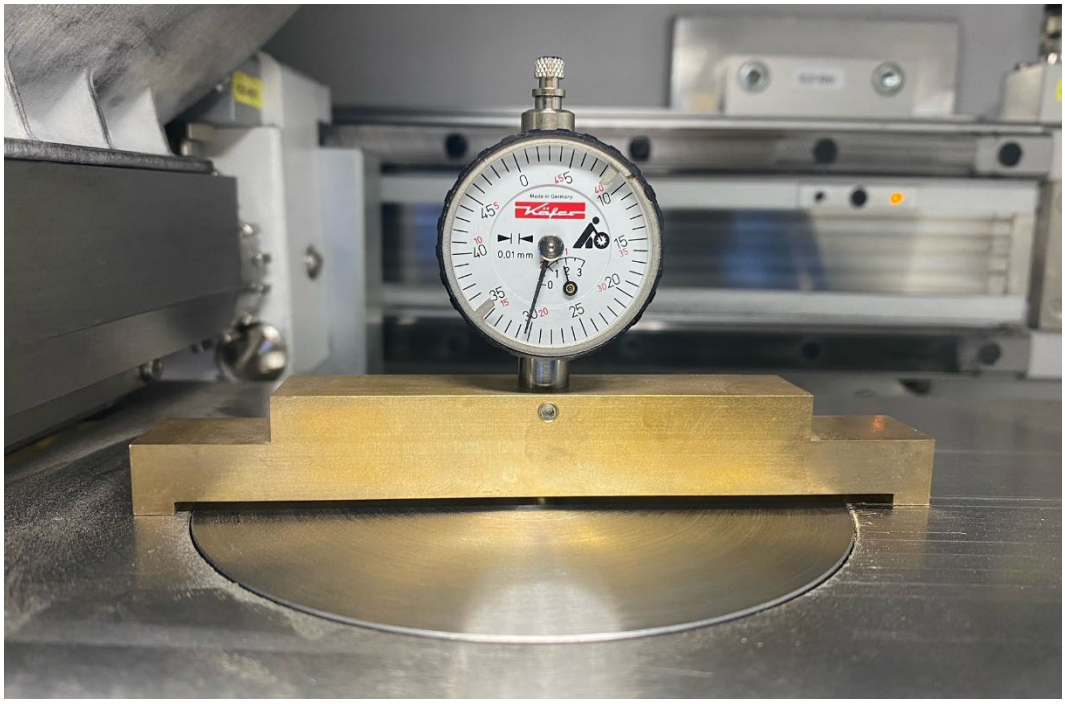

Figure 28. Dial Indicator for Setting Build Plate and Recoater Blade Height.

Due to the difficulties faced with the agglomeration of the GNPs with the 316-L stainless steel powder, modifications to the powder hopper were needed to ensure a smooth and consistent distribution of powder during the print process. The first set of modifications were completed for printing the 316-L and CNT samples that this thesis is an extension of. To assist the powder funneling down through the hopper, a small vibration rocker motor was attached to the side of the hopper. In addition to the external motor, the hopper required something else to provide a consistent distribution while filled with 2vol% GNP-SS

powder. To provide a smoother surface as compared to the standard plastic hopper, the sides were lined with aluminum foil. While the motor and aluminum foil additions were useful for the 1- and 2vol% GNP-SS powders, the 3vol% GNP-SS powder required more modification, resulting in an additional motor being added inside the hopper to directly agitate the powder, resulting in consistent powder distribution and successful prints. The modifications to the hopper can be seen in Figure 29.

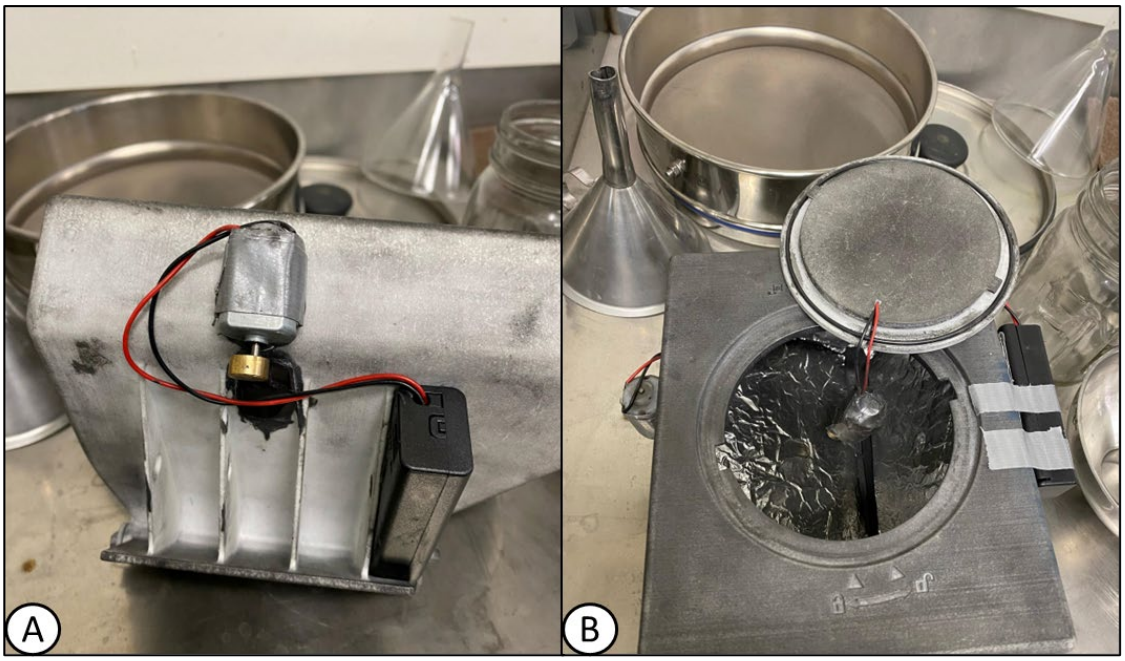

Figure 29. EOS M100 Powder Hopper Modifications. [A] External Vibration Rocker Motor, [B] Hopper with Aluminum Foil-Lined Walls and Direct Interaction Vibration Motor.

Once all previously outlined steps were completed, the print process could begin. After initiating a print, the EOS M100 printer would lock and begin the purge process. To prevent rapid oxidation of the metal during the sinter process, the inside chamber of the printer had to be void of nearly all oxygen. To do this, the printer is supplied with argon (Ar) gas to purge the chamber initially and then continuously supply gas during the print process at a pressure of 5 bar. During the purge, up to 1 m^3 of Ar gas can be used, with an

additional 0.06 m^3/hr used during the print process. Once the oxygen purge was able to reduce the oxygen content below 0.15% in the chamber, the print could begin.

5. Print Sample Variations

As stated before, four composite powder variations and five energy density variations were used, resulting in a total of 18 unique samples for testing. The powder and energy density combinations are seen in Table 5.

Table 5. Composite Powder – Energy Density Print Matrix

Energy Density [J/mm^3]	**Stainless Steel-GNP Powder Composition**			
	Pure SS	1vol% GNP-SS	2vol% GNP-SS	3vol% GNP-SS
60	X	X	Unsuccessful	Not Attempted
67	X	X	X	X
80	X	X	X	X
90	X	X	X	X
100	X	X	X	X

Few issues were met with the printing process when operating at energy densities at and greater than the default 67 J/mm^3. When attempting to print the 2vol% GNP-SS samples at the 60 J/mm^3 energy density, issues were met with proper adhesion to the build plate and within the part itself. The print was attempted twice more with just the 60 J/mm^3 prints on the built plate with the same issues resulting in print failures. It was assumed that the issue arose due to the GNP concentration, as the higher concentration with the lower energy density resulted in poor sintering and fusion. Because of this, the 3vol% GNP-SS powder was not printed at the 60 J/mm^3 energy density to prevent issues with the other energy density prints on the same build plate.

C. CHARACTERIZATION METHODS

1. Scanning Electron Microscopy

To verify an even distribution of the GNP particles within the 316-L stainless steel powder after the HEBM process and ensure the 316-L stainless steel powder was not pulverized during the milling process, composite powder samples were observed under the Thermo-Scientific Helios 5 UX SEM, shown in Figure 30.

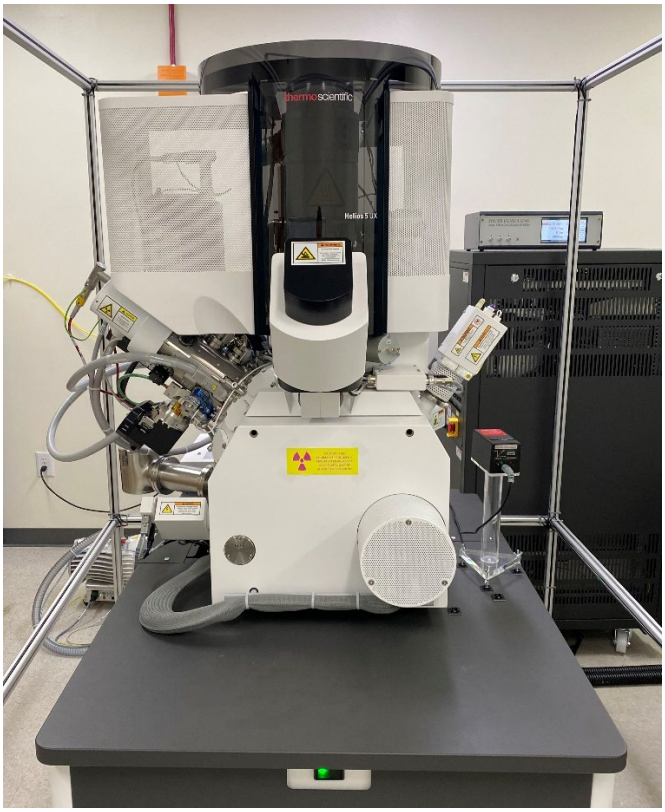

Figure 30. Thermo-Scientific Helios 5 UX Scanning Electron Microscope.

After placing powder on a SEM sample mount using double sided conductive carbon tape, the SEM was vented from vacuum to allow the door to be open and the sample placed inside. The internal chamber of the SEM is very sensitive and susceptible to damage, so to prevent contamination or moisture from entering, pressurized air was sprayed over the sample to remove any loose particles and the sample mount was placed in a small oven just before placing in the chamber to remove any accumulated moisture.

Once in the chamber, the vacuum that allows for the proper operation of the electron beam was initiated. After the proper vacuum value was reached, the samples could be observed and imaged. To record the composition of the powders, pictures were taken of the sample at various magnifications, ranging from 1000–5000x magnification.

For verification purposes to ensure that the stainless-steel powder particles were not flattened or otherwise destroyed during the milling process, comparisons were made with the un-milled powder. As seen in Figure 31, a comparison of milled and un-milled powder, there were no obvious deformations of the powder when observed under the SEM. This was desirable, as the standard powder is sold in the specific size and shape range for optimal printing in the EOS M100 printer. View comparing the two images in the figure, it is obvious that the general shape of the stainless-steel particles is spherical, not flattened, split, or crushed as could have happened with incorrect HEMB parameters. Furthermore, it can be seen in the second image of the composite powder with 3%vol GNP that the GNP's are evenly distributed within the powder, highlighted with red circles seen in picture [B]. If any random area on the sample stage did not show an even distribution of GNP particles or all the particles were agglomerated in one large mass, the powder would need to be milled again and the HEBM parameters may have required alternations. For all the powder samples taken for SEM observation, even distribution of the GNP particles was found consistently with no large masses of GNPs in the powder.

Cross sections of printed sample were taken for SEM observation. A Struers Secotom-20 high-speed saw was used to cut across the midsection of printed samples, creating two equal halves. One half was set in an epoxy puck for grinding and polishing using an Ecomet Variable Speed Grinder-Polisher. One half cross section was observed under a Nikon Epiphot 200 optical microscope. The other half was mounted to an Al stub with double sided carbon tape adhered to it. This sample was imaged in the SEM; the Helios 5-UX SEM.

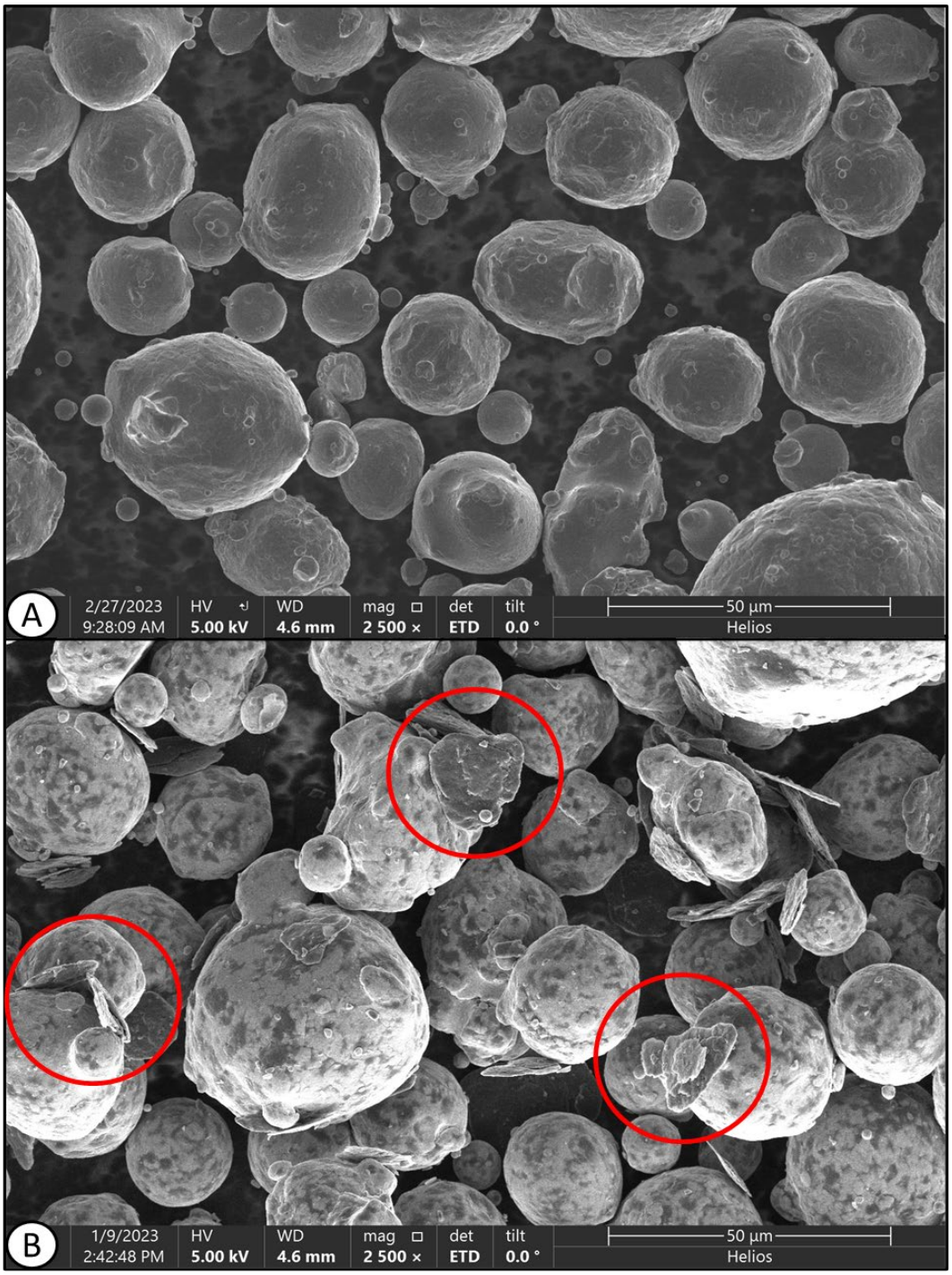

Figure 31. SEM Images showing Un-Milled vs. Milled Powders at 2500x Magnification. [A] Un-Milled Pure Stainless-Steel Powder from EOS, [B] Milled 3vol% GNP-SS Composite Powder.

2. Optical Profilometry

To measure the surface roughness of the printed samples, A Zygo New View 7100 optical profilometer was used, seen in Figure 32. Located in a level 10,000 clean room to prevent environmental interference such as vibration, and physical contaminants, this machine conducts non-contact and three-dimensional scans utilizing white light interferometry [68]. Interferometry works based on the principle of superposition, where a sample is illuminated with white light and the different wavelengths of light reflect and intersect, combining as the detector receives the reflected wavelengths. Based on the reflections and knowing the initial height of the light source and the scanning depth from start to end, a computer software creates a 3-D map of the sample for each iteration of the process [69].

Figure 32. Zygo New View 7100 Optical Profilometer.

The Zygo optical profilometer is operated by manually determining the focus range of the sample to be measured. By moving the objective lens and illuminator unit vertically, the lower and upper bounds of focus are determined when the sample is out of focus and the fringes are at the corner of the viewing screen. Fringes, shown in Figure 33, are areas of interference that indicate that the sample is still potentially in focus, and tend to move toward the edge of the viewing screen when the objective lens is in the correct position. Once the focus bounds are determined, the range of the scan is provided to the software. Following the range determination, the light level must be adjusted to prevent the detector from receiving faulty data, as too much or too little light can prevent the whole surface from being mapped. Finally, a scanning area is determined, with all samples used in this experiment being scanned over a 3 mm x 3 mm square.

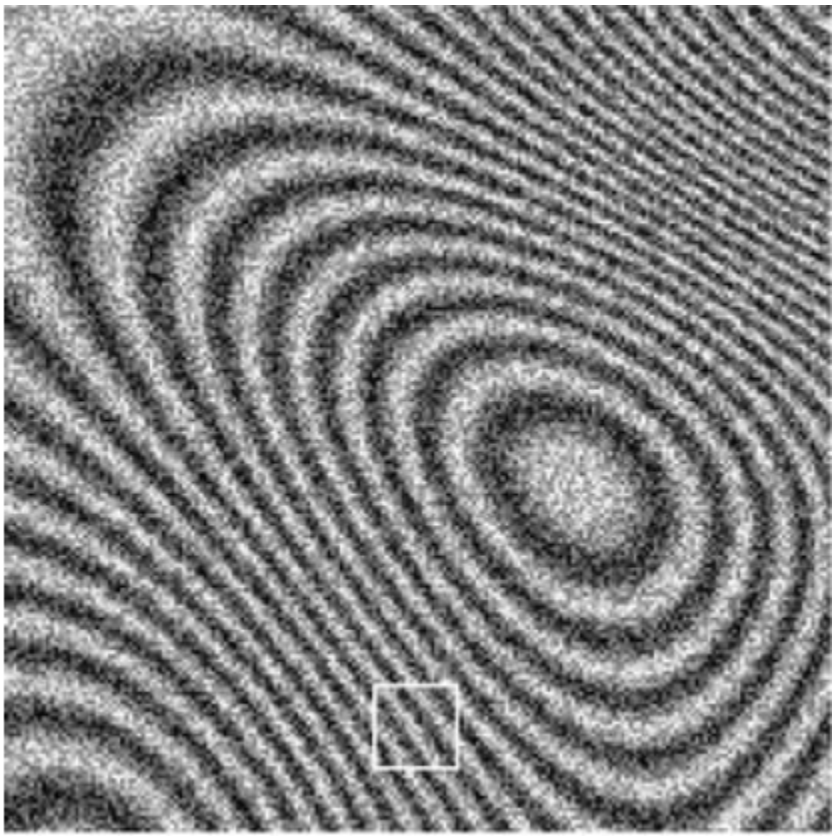

Figure 33. Fringe Pattern Across a Viewing Screen, Showing Focus Limits. Source: [70].

3. Krüss MSA Water Drop Analysis

A Krüss mobile surface analyzer (MSA) was used to measure the contact angles of measured water drops on the sample surfaces. The Krüss MSA, seen in Figure 34, operates using small liquid dispensers, a backlight, and a camera that connects directly to the Krüss Advance software. When the MSA is placed over a sample and water is dispensed on the surface, the water drop is located between the light source and the camera, providing a quality outline of the water drop sides parallel to the camera. The computer software superimposes two rays on each side of the water drop, matching one ray from each side to the sample surface and one to the edge of the water drop, creating an angle measurement. Due to variability in the data when the software was determining the position of the surface, manual placement of the sample surface was used, with the software still fitting the other line ray to determine the angle. The angle measurement is shaped by the fitting model chosen, decided to be ellipse-tangent for this experiment, meaning that the ray fitted to the water drop was tangent to the drop and the overall shape of the drop was likely an ellipse. An example of a measurement taken by the Krüss MSA may be seen in Figure 35.

Figure 34. Krüss Mobile Surface Analyzer.

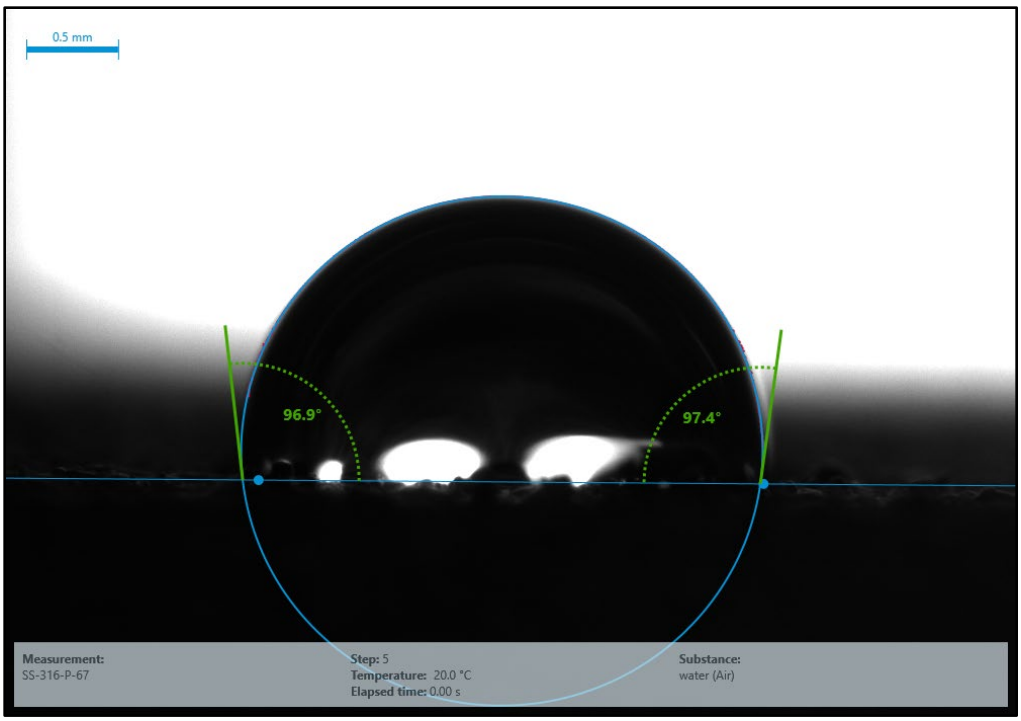

Figure 35. Krüss MSA Contact Angle Measurement of Pure Stainless-Steel Sample.

Due to malfunctions with the MSA, the application of water droplets had to be manually dispensed using a micro-pipette. For all samples, a Fisherbrand micro-pipette, seen in Figure 36, was set to dispense 2 microliters on the sample surface. Attempts were made to dispense each water from a uniform height, but this was unsuccessful as the water would keep attached to the pipette tip until touching the sample surface. The MSA was placed over the sample immediately after the water drop was dispensed to limit data error.

Figure 36. Fisherbrand Elite Micro-Pipette.

THIS PAGE INTENTIONALLY LEFT BLANK

IV. SCANNING ELECTRON MICROSCOPY

In this chapter, SEM images of the 316-L stainless-steel and GNP composite powder and the resulting print plates will be investigated to verify presence of the nanomaterials within the printed samples.

A. MICROSCOPY OF 316-L STAINLESS STEEL AND GRAPHENE NANOPLATELET COMPOSITE POWDER

After the HEBM process to evenly distribute the GNP nanoparticles throughout the stainless-steel powder, SEM images were taken of the 1 vol% GNP, 2 vol% GNP, and 3 vol% GNP composite powders to verify the mixing process was successful. In addition to verification of the presence of GNP particles, the SEM was used to ensure that the stainless-steel particles were not deformed during the milling process. Spherical particles are needed for efficient powder jetting during the 3-D metal printing process. Oblong or deformed particles could prevent a steady flow of powder to the build plate during printing. As a form of control, micrographs of the pure stainless-steel powder were also taken, as seen in Figure 37. In Figure 37, with images taken at 1000 and 5000x magnification. The uniform shape of the stainless-steel powder can be seen. Barring a small number of deformed particles highlighted by a red circle within image [A], the powder was determined to be fit for use as there were no visible contaminants or other apparent issues with the powder.

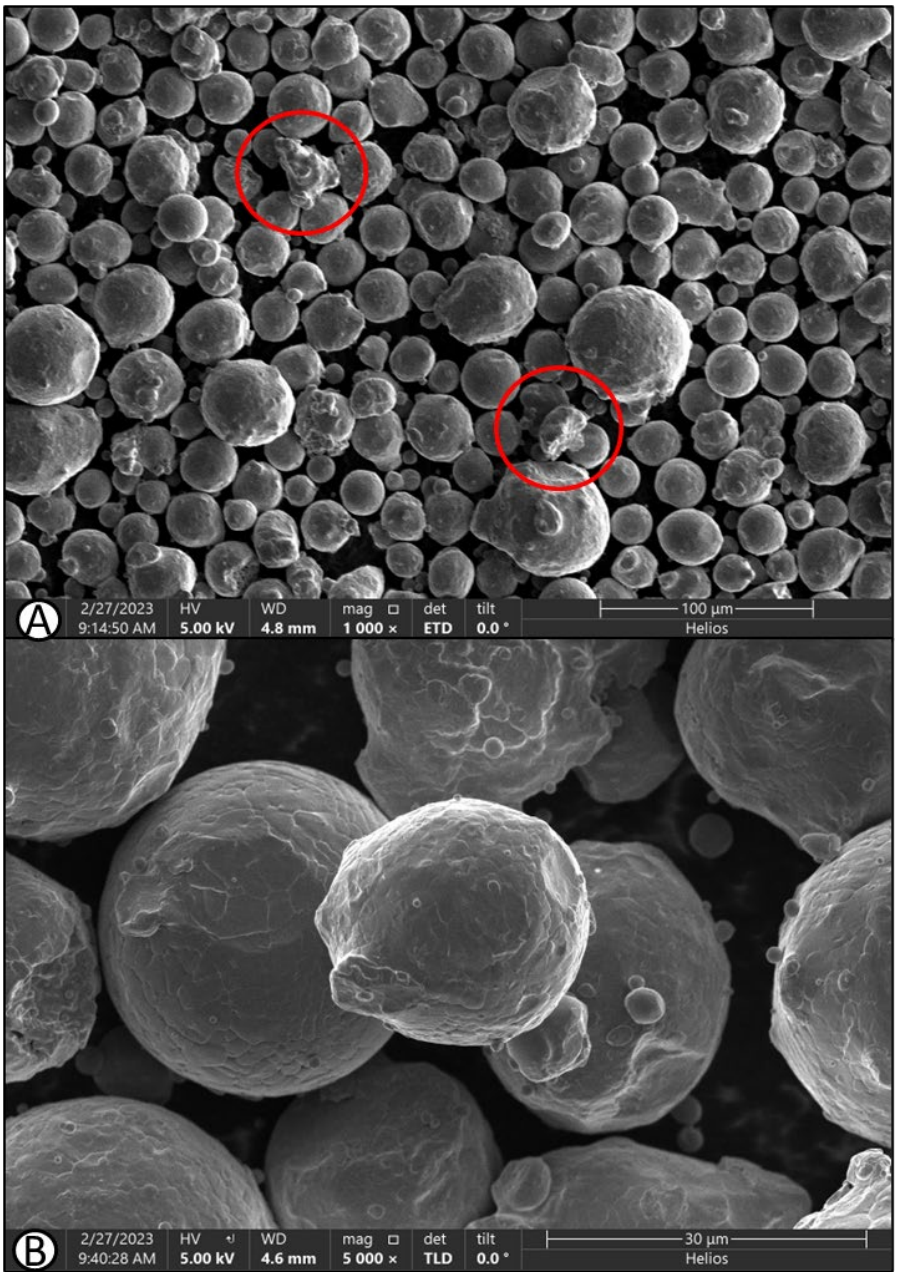

Figure 37. SEM Images of Pure Stainless-Steel Powder. [A] Un-Milled Pure Stainless-Steel Powder from EOS at 1000x Magnification, [B] 5000x Magnification

The presence of GNP particles and the preservation of the stainless-steel particles was easy to determine for all three composite powders, beginning with the 1 vol% GNP powder, seen in Figure 38. Within Figure 38, the red circles in image [A] are utilized to show the GNP particles within the powder, proving that there was an even distribution

during the milling process. Image [B], taken at another location of the prepared powder SEM sample, was taken at 5000x magnification to show detail of the GNP's, characterized by the flakey appearance signifying the many graphene layers held together within a GNP stack.

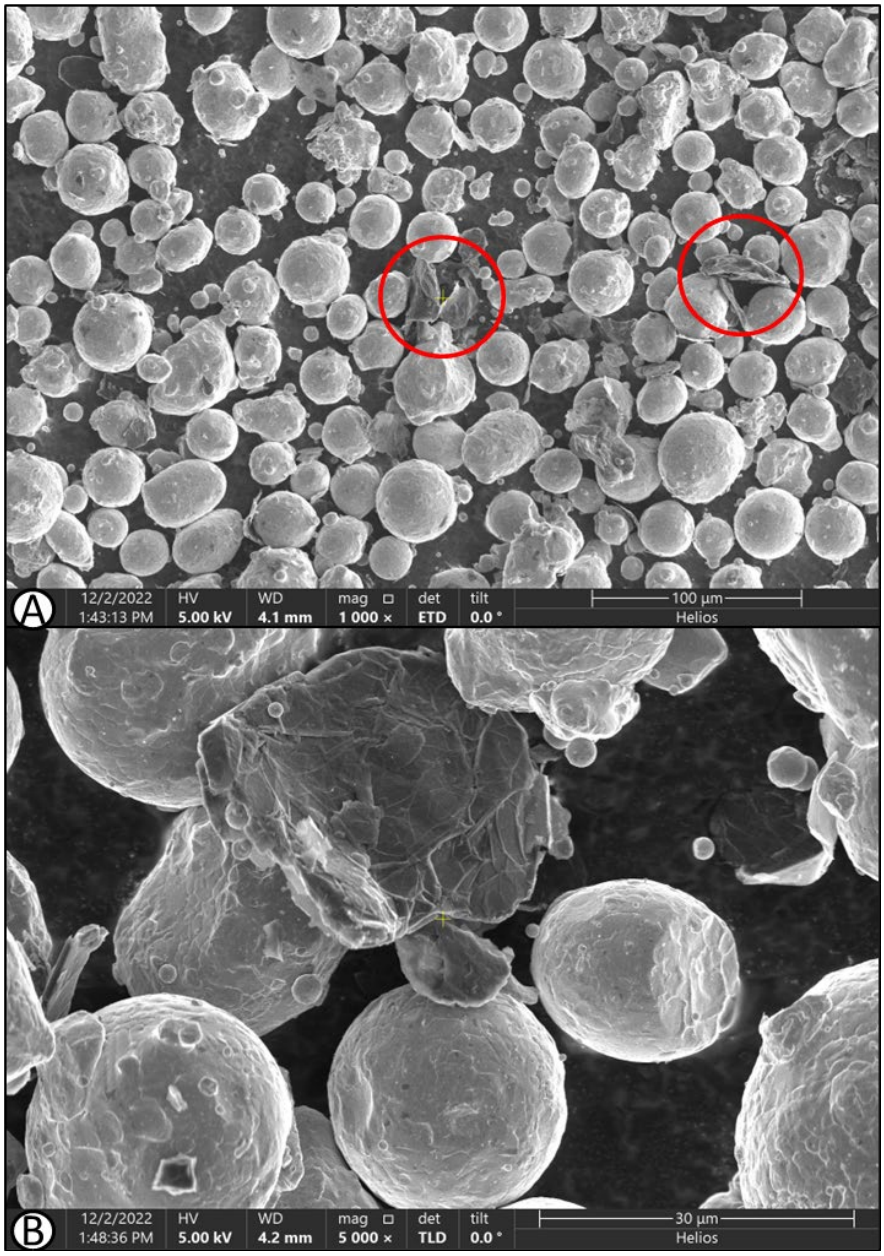

Figure 38. SEM Images of 1 vol% GNP Stainless-Steel Powder. [A] Milled 1 vol% GNP Stainless-Steel Powder at 1000x Magnification, [B] 5000x Magnification.

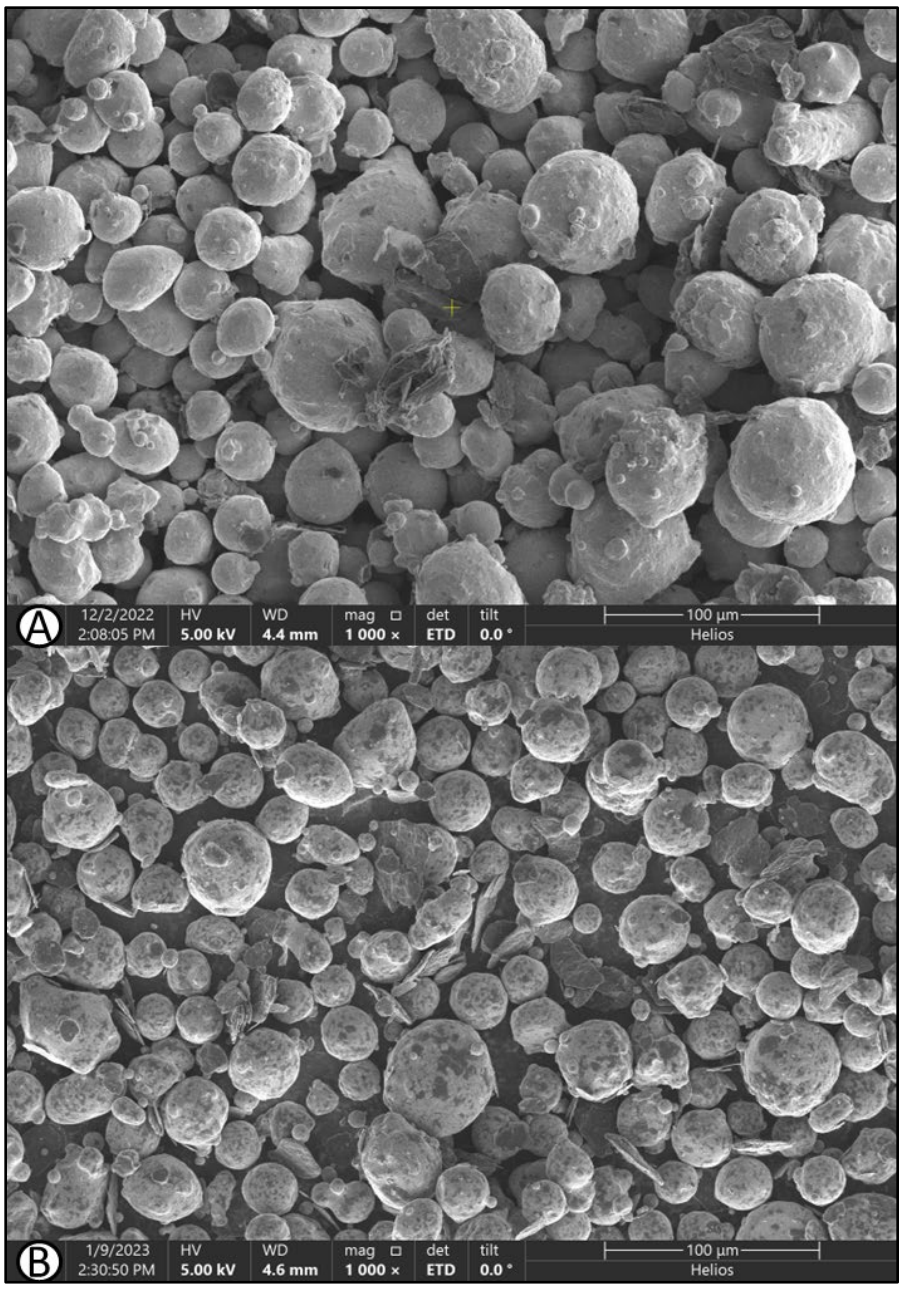

Figure 39. SEM Images of Milled Composite Powder. [A] Milled 2 vol% GNP Stainless-Steel Powder at 1000x Magnification, [B] Milled 3 vol% GNP Stainless-Steel Powder at 1000x Magnification.

Looking at the images presented in Figure 38 and Figure 39, there is a uniform distribution of GNP particles within the stainless-steel powder, creating a uniform composite powder. When comparing the two figures, which between the two show all three

composite powder mixes, there are distinct differences in the material composition showing an increase in the concentration of GNP particles. The 1 vol% GNP powder was used as a baseline for observing the powders with increased GNP concentration to ensure that what was being observed was what was to be expected. Beginning with image Figure 39 [A], the 2 vol% GNP powder, the irregular and layered particles of graphene are seen in greater numbers than the 1 vol% GNP powder as expected, and the metal particles appear to have maintained spherical shape. The GNP particles appear to have begun to breakdown on the surface of some of the metal particles, providing a darker shadow on the surface of the stainless-steel particles. The 3 vol% GNP powder, seen in Figure 39 [B], shows that the regularity of the GNP breakdown across the metal particles appears to have increased, indicating that the powder is now thoroughly combined, and the GNP particles may have even been milled to the point where the many layered stacks began to delaminate and spread through the powder.

After the successful print of all the samples, from pure stainless-steel up to the 3 vol% GNP composite powder, samples were prepared for SEM imaging and analysis to verify the presence of the GNP particles within the printed sample after the L-PBF print process.

B. MICROSCOPY OF PURE STAINLESS STEEL AND 3 VOL% GRAPHENE NANOPLATELET PRINT SAMPLES

There were concerns that the GNP particles could have been sifted out of the composite powder to the top of the powder hopper during printing. Due to the lower density of the GNP particles compared to the stainless-steel particles, there was a possibility that the GNP particles would be displaced towards the top of the composite powder. This was due to the movement of the build plate. Additionally, the vibration motors mounted on the powder hopper provided additional agitation. To; one, verify the presence of GNP particles within the final printed samples; and two, confirm reasonable distribution of the GNPs, cross sections of the smaller 10 mm x 10 mm plates were taken and observed under the SEM.

Due to print complications with the 3 vol% GNP powder, it was determined that samples of each print density from that powder would be examined for the presence of GNP particles in the print. This action also provided a chance to observe the microstructure of each print, at each energy density, to understand if any notable changes were seen in the microstructure of the prints or if the effect of energy density was only found on the surface of the samples. Because of issues with the 2 vol% GNP powder when printing the 60 J/mm^3 energy density samples, it was decided not to attempt the same energy density with the 3 vol% GNP powder, resulting in samples printed using 67, 80, 90, and 100 J/mm^3 being observed under the SEM.

With the samples inserted in the SEM, observation began using the secondary electron detector. It was apparent that there were unknown particles embedded in the sample surface with indications that the particles were GNP particles or even single graphene sheets that had become delaminated from its original GNP stack. As seen in Figure 40, a cross section of the 3 vol% GNP sample printed at 67 J/mm^3, the unknown particles were found across the sample cross section, indicating that the GNP particles were maintained throughout the composite powder mix when traveling through the powder hopper and undergoing the L-PBF process to create the sample. Seen in the image are many lines appearing to cut into the surface of the sample, which are hypothesized to be the layers of the print sample as the image is being viewed from section view profile. Additionally, the potential GNP particles do not appear as in the powder, rather they appear to be dark shadowy spots in the sample. This is indicative that the particles were fragmented when hit by the laser during the print process, ensuring a more even distribution of the particles throughout the metal matrix.

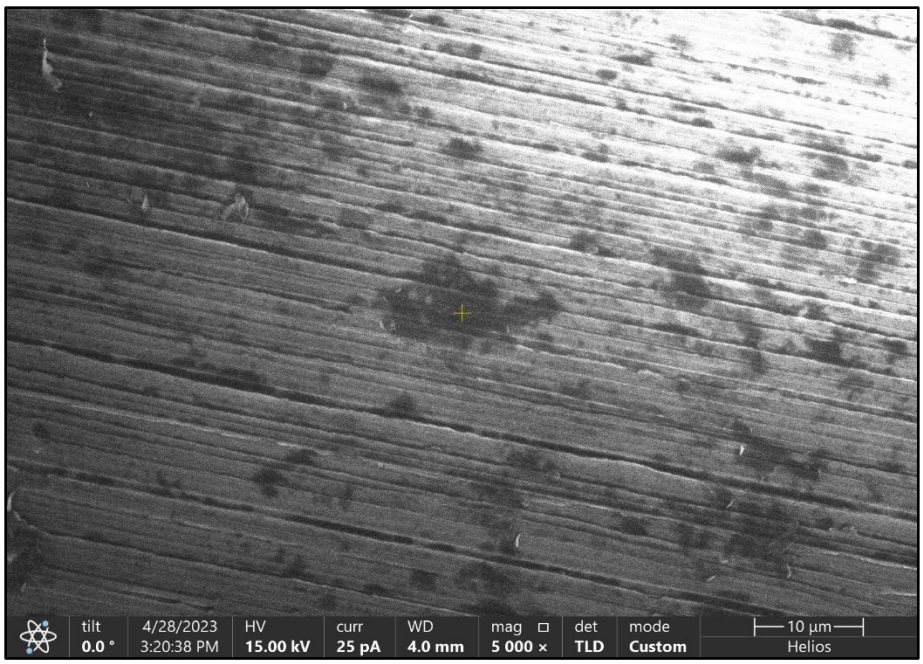

Figure 40. SEM Image of 3 vol% GNP Sample Printed at 67 J/mm^3 at 5000x Magnification.

Seen in the middle of Figure 40 is a darker particle thought to be a GNP. To verify, as the process was standard throughout observation of each sample examined under the SEM, greater magnification images were taken to identify common features to the GNP particles when in the composite powder, seen in Figure 41. In the figure, the unknown particle was determined to be a GNP, due to the flakey appearance and contrasting appearance to the background material. To further verify, a secondary method of observation of the sample was taken, using an electron backscatter probe (ABS). While an Everhart Thornley (EHT) detector can also collect back scattered electrons, an ABS probe is specifically designed to collect backscattered electrons from the initial electron beam used to image the sample. Due to the collection efficiency of backscattered electrons being much lower than what can be collected with secondary electrons, the use of an ABS probe and the wide collection face ensures that the sample being observed is properly shown. An ANS probe operates by collecting back scattered electrons from the sample surface, where heavier and denser elements reflect more electrons, producing a bright image on the screen. In contrast, less dense elements, in this case carbon being much less dense than the stainless-steel compound, reflect less backscattered electrons, resulting in a darker surface.

The contrast between the two elemental compounds found in the print plates is seen in Figure 42, which is the same area as in Figure 41 but uses the ABS probe collecting back scattered electrons instead of secondary electrons. The inconsistency in Figure 42 indicates that the GNP particle being shown is integrated with the surrounding environment, confirming the fact that the printed samples are fully combined stainless-steel and GNP composites.

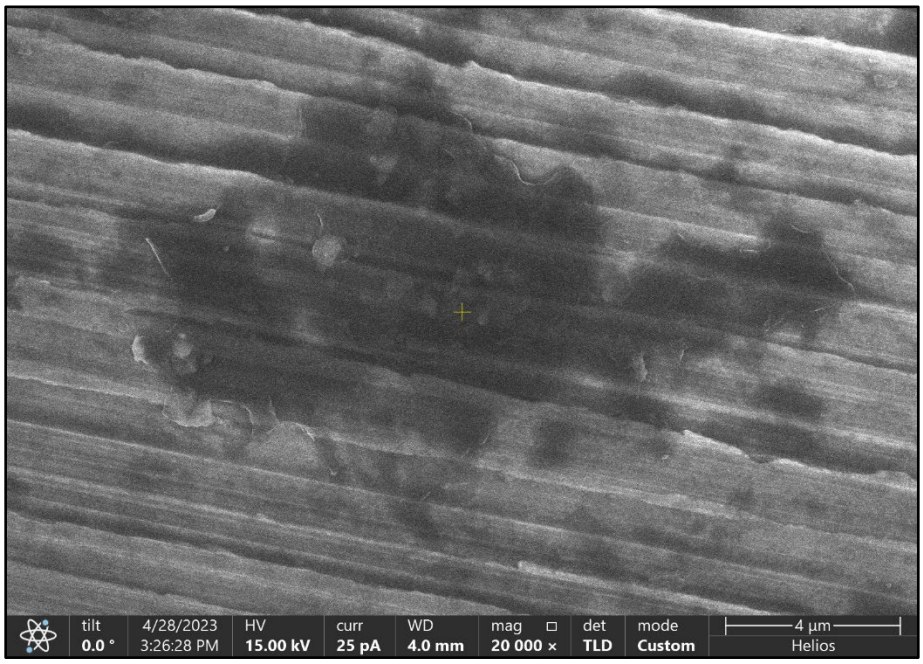

Figure 41. SEM Image of 3 vol% GNP Sample Printed at 67 J/mm^3 at 20000x Magnification.

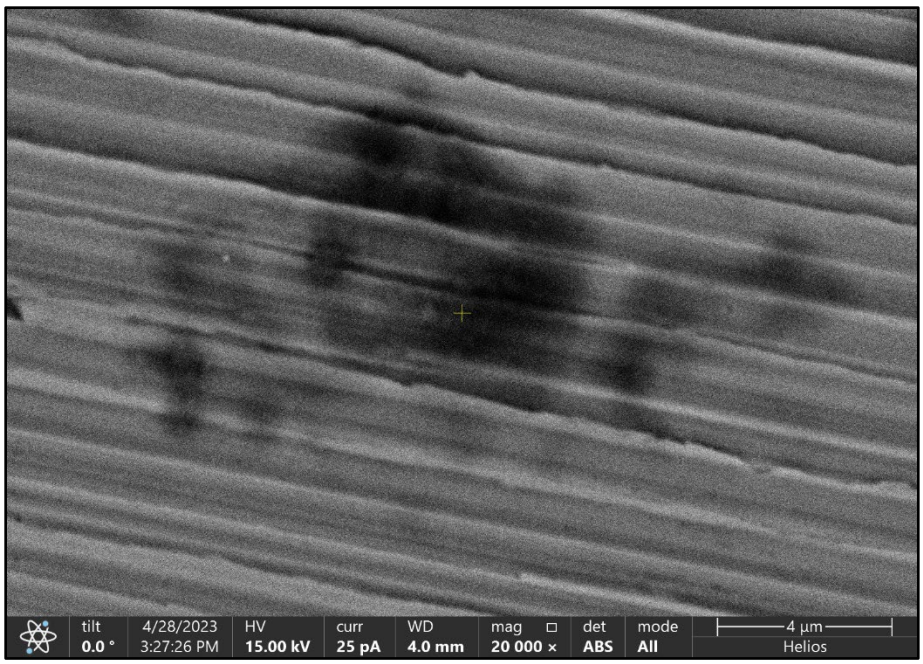

Figure 42. SEM Image of 3 vol% GNP Printed Sample at 67 J/mm^3 Using ABS Backscatter Probe at 20000x Magnification.

It is important to note that samples printed using the 3 vol% GNP powder and different energy densities were also observed with the SEM. The figures shown in the previous sections were chosen as they provide the clearest images and provide the greatest insight. Samples printed using the 1 vol% and 2 vol% GNP composite powders were not observed using the SEM.

THIS PAGE INTENTIONALLY LEFT BLANK

V. WETTABILITY CHARACTERIZATION

A. SESSILE DROP CONTACT ANGLE MEASUREMENTS

1. As-Printed Plates

To characterize the wettability of the samples after printing was complete, sessile drop contact angle measurements were recorded using the Krüss MSA mobile surface analyzer. When operating the MSA, the shape profile for angle measurement was chosen to be ellipse-tangent while the baseline determination was switched to manual from automatic due to high fluctuations in the measurements due to the highly irregular surfaces of the printed plates. Choosing a different shape profile would have resulted in varied contact angle measurements, but ultimately the ellipse-tangent method was chosen as the method typically provides median values across all other methods. Figure 43 shows several examples of the MSA droplet images and measurements taken.

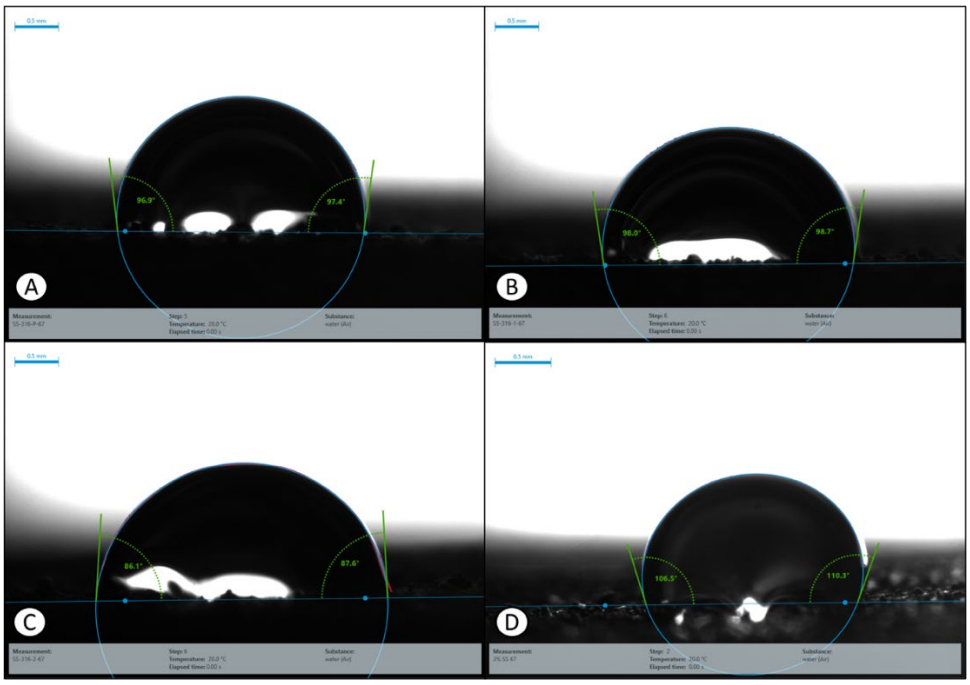

Figure 43. Krüss MSA Measurements of Samples Printed at 67 J/mm^3. [A] Pure Stainless Steel, [B] 1 vol% GNP, [C] 2 vol% GNP, [D] 3 vol% GNP.

For each powder type, five different print densities were used to create the print samples with the exception for the 60 J/mm^3 energy density for the 2 vol% and 3 vol% GNP powder. For each print plate, with eighteen samples total, five sessile drop measurements were taken across the surface, with one center and one near each corner of the sample surface. All measurement data by print energy density to observe trends in the contact angle as the surface finish varied (i.e., rough printed surface versus a smoother polished surface) are shown in Figure 44.

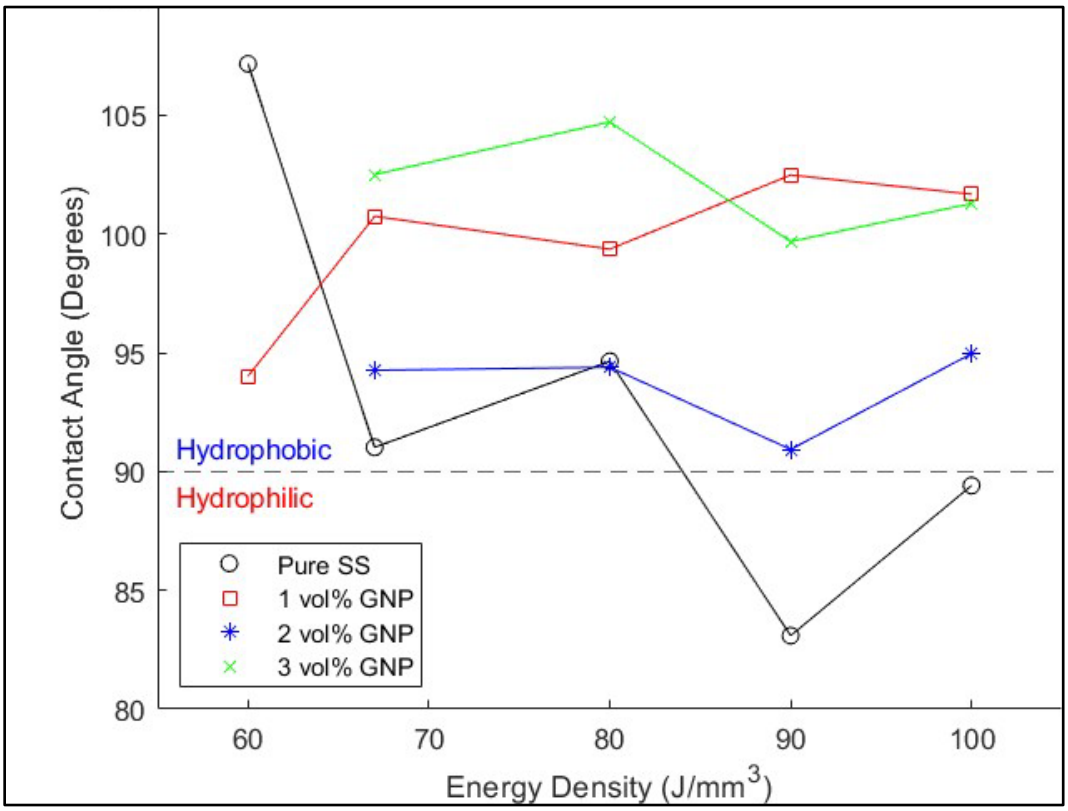

Figure 44. Contact Angle Measurements for All As-Printed Sample Plates.

The plot shown in Figure 44 shows several trends corresponding to both the effect of energy density of the sample as well as the effect of the concentration of GNP particles on the overall contact angle measured. Beginning with the effect of the energy density that each sample was printed with; the clearest trend can be seen with the pure stainless-steel samples indicated by the black hollow circles. Changes to the energy density with an

unaltered powder normally results in a smoother, finer print finish throughout a sample, meaning that ranging from 60 to 100 J/mm^3, the former would create the roughest sample surface while the latter energy density would result in the smoothest surface. This is proven accurate regarding the pure stainless-steel sample, where the average contact angle dropped roughly 17° across the range of energy densities, as seen in Figure 45. Each box and whisker plot contains five measurements that were taken across the surface of each sample, with a water drop placed in the middle and then each corner of the sample. Within the figure, it is seen that the range of the measurements decreased as the energy density increased, indicating a smoother and more uniform surface for consistent sessile drop measurements.

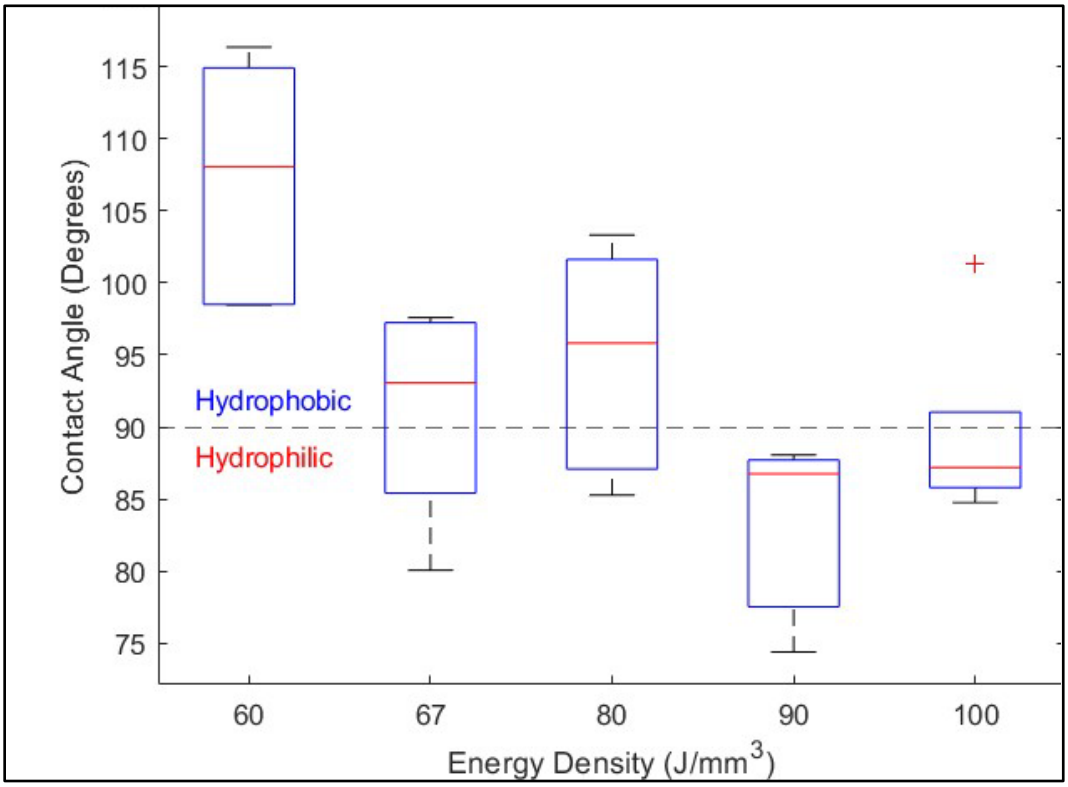

Figure 45. Contact Angle Measurement by Sample Energy Density for As-Printed Pure Stainless-Steel Sample Plates.

When taking the other composite powder samples into consideration, the trend does follow the expected decrease of contact angle as the surface finish would be assumed to be smoother. Contrarily, the 1 vol% GNP and 2% vol GNP sample average contact angle appears to increase as the energy density was increased, indicating that the presence of the GNP particles had a role, either creating a rougher surface or creating a more hydrophobic surface with graphene's natural hydrophobicity. When viewing the figure with regards to the GNP concentration, another positive trend is seen with respect to the contact angle measurements. As the energy density increased for the pure stainless-steel samples, the average contact angle dipped and remained below the hydrophobic-hydrophilic threshold. In contrast to this, all the composite powder samples maintained contact angle measurements over 90°, meaning that the samples were definitively hydrophobic on the surface. To further resolve the possible roles of the GNPs in increased contact angle measurements and potential hydrophobicity, tests were conducted on the ground and polished surfaces of each powder type and energy density. Seen in Figure 46, the 3 vol% GNP samples all averaged contact angle measurements surpassing the 90° hydrophobicity threshold. It is interesting to note that the box and whisker plots for the 3 vol% GNP had a greater range than the pure stainless-steel samples shown in Figure 45. It is speculated that the presence of GNP particles created microscopic spatter during the print process, sending print particles randomly, creating some smoother regions and others rougher than the average, causing a wider range of contact angle values measured. The remainder of the box and whisker plots for each sample material composition can be found in Appendix D.

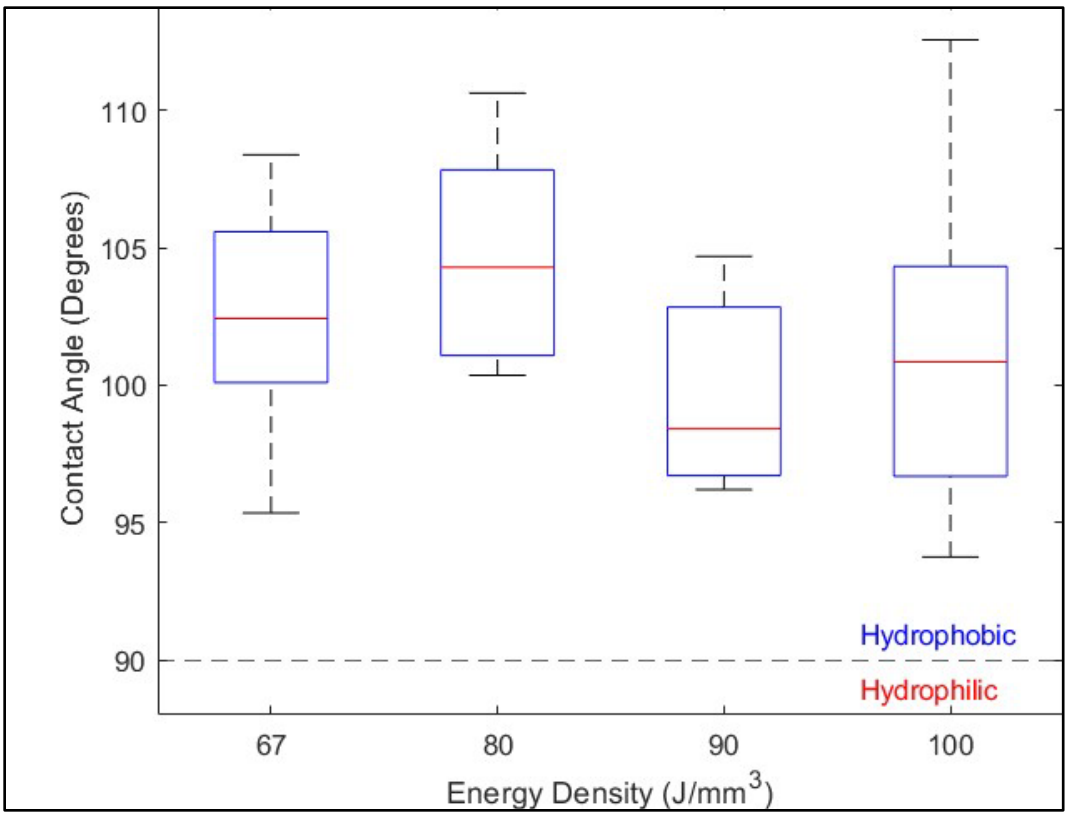

Figure 46. Contact Angle Measurement by Sample Energy Density for As-Printed 3 vol% GNP Stainless-Steel Sample Plates.

2. Polished Print Plates

To eliminate the surface roughness variable for the contact angle measurements to measure the true effect of the added GNP particles, the samples had to undergo a grinding and polishing procedure using an Ecomet Variable Speed Grinder-Polisher. To still utilize the mounting chuck, the samples were ground by hand using a 320-grit paper until there was a uniform and flat surface on the bottom of the sample. Once flat, a heat gun was used to heat a mounting epoxy to its melting point which was then poured onto the bottom of the sample and a puck pressed on top to create an externally mounted sample puck, as seen in Figure 47. To ensure the samples were properly adhered to the puck while maintaining the contact with the flat surface the samples were placed on, the pucks were pressed on to the sample through the mounting chuck which was laid flat on the table. Once secured to

the puck, the samples were subjected to a series of grinding and polishing papers, as seen in Table 6.

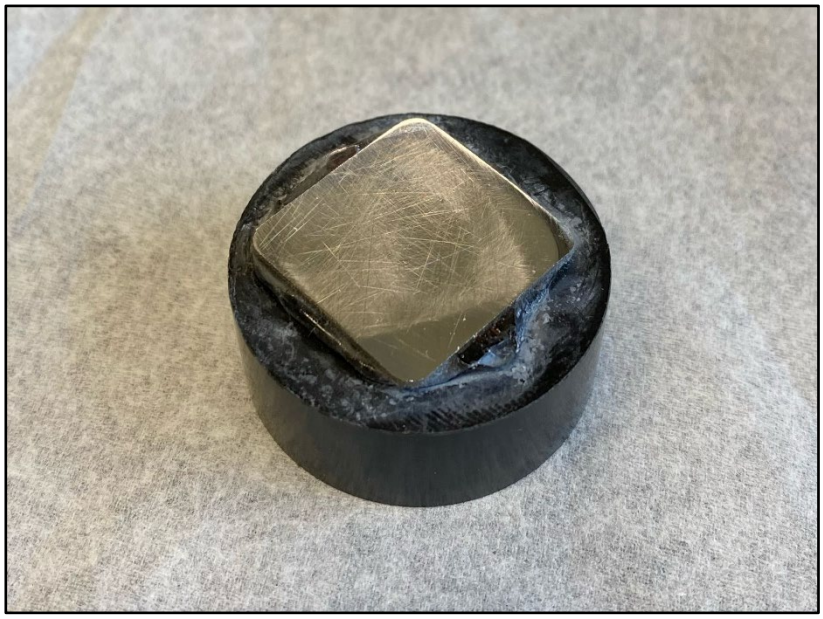

Figure 47. Externally Mounted Print Sample for Grinding/Polishing Process.

Table 6. Grinding and Polishing Procedure for Polished Sample Plates

Polishing Paper Grit Size	Time Required (Minutes)	Force (Lbs.)
320	90	8
600	60	5
800	60	5
1200	30	5
Micro-cloth (0.5 μm Alumina Powder)	30	5

The time and force applied for each polishing paper was determined to ensure that the sample would be sufficiently ground down to a uniform surface well below the initial surface. This was to ensure that there would be no as-printed surface that would be tested again when conducting the contact angle test. When using the micro-cloth with the alumina powder, the goal was to not create a perfectly polished surface but rather act as a final cleaning to ensure the surface finish was uniform, not necessarily perfectly smooth. After polishing, the samples were cleaned with ethanol and dried using a heat gun to prevent any

ground particles or alcohol residue from affecting the contact angle measurements with the Krüss MSA.

After all the samples needed were properly ground down and polished, the same Krüss MSA contact angle measurements were taken. Because the samples were now mounted on plastic pucks, the testing setup had to be slightly modified. The MSA was set on top of additional pucks, as seen in Figure 47, to ensure the MSA was slightly higher than the surface of the samples to ensure the camera could capture the drops on the highly reflective polished surface.

Figure 48. Krüss MSA Measurement Setup Modifications for Polished Surfaces.

Following the same procedure as was conducted with the as-printed samples, the polished samples were tested at five locations across the surface. Figure 49 shows examples of the MSA measurements across the polished surfaces, again of the samples printed using an energy density of 67 J/mm^3. Additional contact angle images with the measurements are shown in Appendix B.

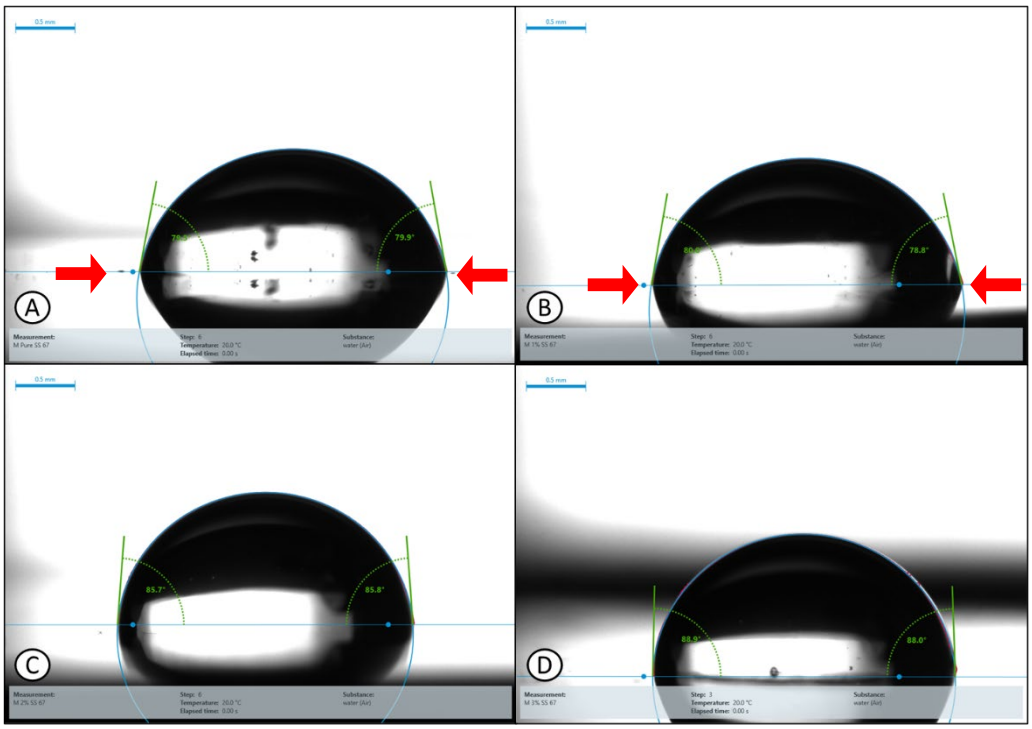

Figure 49. Krüss MSA Measurements of Polished Samples Printed at 67 J/mm3. [A] Pure Stainless Steel, [B] 1 vol% GNP, [C] 2 vol% GNP, [D] 3 vol% GNP.

The measurement process for the polished samples was more difficult with regards to determining the location where the water drop was fully in contact with the surface due to the higher reflectivity of the polished surfaces versus the rougher, as-printed surfaces. With images in Figure 49 [C] and 49 [D], the darker parts of the images with a water drop having a greater contact angle made the water drop appear to be rounder and less in contact with the sample surface, whereas the samples with a lower contact angle like in Figure 49 [A] and 48 [B] were easier to identify due to the sharp point as the reflection

point, shown with red arrows in the figure. Plots of the data recorded were made to identify any trends between the print energy density as well as the material composition.

Contact angles as a function of printing energy density is presented in Figure 50. The plot shows a strong trend regarding the presence of GNP particles within the printed metal matrix. Beginning with a comparison between the pure stainless steel and the 1 vol% GNP samples, there is an almost exact relationship with each energy density with the composite powder samples having a 5–10° greater average contact angle. While both sets of data are well below the hydrophobic threshold, the presence of GNPs clearly created a less hydrophilic surface when compared to the pure stainless-steel surface. Taking the higher concentration samples into account, there again is an increase in the average contact angle measurement as the GNP concentration increases, with the 3 vol% GNP plates having an average of 10–15° greater value than the standard stainless-steel plates. These trends are interesting as the surface roughness variable was essentially removed from consideration through the polishing process. With only one variable to contend with, conclusions can be made about GNP particles having a direct influence on the hydrophobicity of the samples, as discussed in the following section.

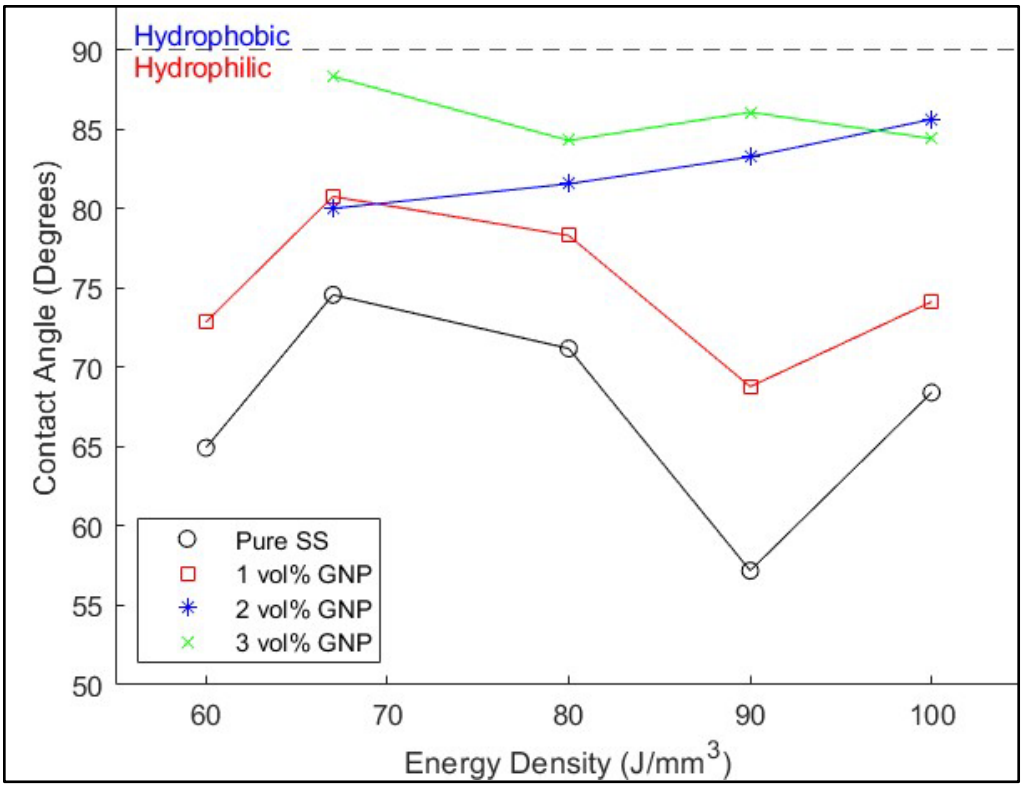

Figure 50. Contact Angle Measurements for All Polished Sample Plates.

3. Trends When Comparing As-Printed Plate and Polished Plate Contact Angle Data

A strong connection between the measured contact angle and the sample material composition can be found in both the as-printed and polished plate graphs shown before. To further analyze the data, both plots of data have been combined and can be seen in Figure 51.

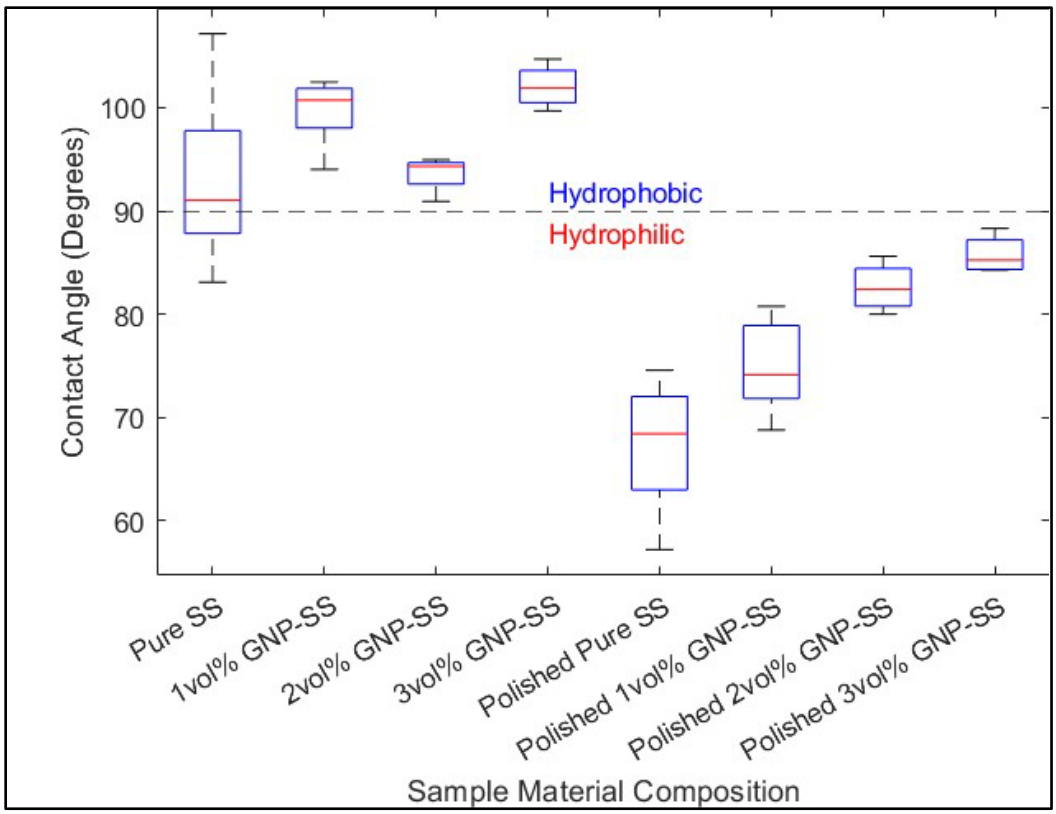

Figure 51. Contact Angle Measurements for All Samples.

Displayed as box and whisker plots, the data shown is the overall average of all the respective print densities that each sample material composition was printed at, from 60 to 100 J/mm^3. Beginning with the overall range of measurements, the standard stainless-steel samples of both varieties of surface sample had the greatest range of values. There is a possibility that the additional energy density value of 60 J/mm^3, which was only used for the pure stainless-steel and the 1 vol% GNP samples could have skewed the data and increased the range. However, when the data for only the 67 – 100 J/mm^3 was plotted, the size of the box and whisker plots did not change dramatically, eliminating the possibility of troublesome data from the additional energy density, i.e., no outliers observed. As the volume concentration of GNP particles increases, there is a clear increase in the measured contact angle. The 3 vol% GNP samples for both the as-printed and polished category have the tightest range of data as well as the greatest average value for the contact angle measurement. This relationship suggests that for those samples, printed from 67–100

J/mm^3, the energy density of the print was less important for the creation of a hydrophobic surface than the volume concentration of GNP particles. When only looking at the polished data in Figure 51, the 3 vol% GNP samples have the greatest average contact angle, bringing the measurement values almost to the hydrophobic threshold.

By removing the surface roughness variable with regards to measuring the contact angle of water drops, the only potential influence could be the GNP particles. Through the polishing process, the surface roughness of each sample was reduced to a level near perfectly smooth. Without the presence of peaks and valleys, especially on such a microscopic scale, the ability for water a water drop to be repelled is reduced drastically, seen in Figure 51, where the contact angle measurements between the as-printed and polished samples differed by approximately 20°, with every polished sample measuring below the 90° hydrophobic threshold. The end of the polishing process, where the samples were polished with using the micro-cloth and 0.5μm alumina powder, lowered the surface roughness of the samples to below one nature's best hydrophobic surfaces, the lotus leaf, previously shown in Figure 10. With such a fine surface, without the peaks to support the water drop and the valleys to trap air for further support, the only feasible source of increasing the hydrophobicity of the polished samples had to be from the GNP particles. This is confirmed when the progression of GNP concentration within the stainless-steel powder is plotted against the measured contact angle as in Figure 51.

B. SURFACE ROUGHNESS MEASUREMENTS

The conclusions made in the previous section regarding the role of GNP particles as the main enhancement towards the creation or improvement of hydrophobic surfaces are confirmed when taking surface roughness measurements of the test surfaces. Using the Zygo New View 7100 Optical Profilometer, three data points were averaged across a 3 mm x 3 mm region of each sample plate. An example of a data profile produced using the Zygo optical profilometer can be seen in Figure 52. The first data point gathered was the peak-to-valley (PV) range of the sample, where the value recorded was the difference between the height of the highest peak and lowest valley within the measurement area. The second data point collected was the surface roughness (Ra), being the average height of the

peaks and valleys across the evaluated area. The last data point recorded for each sample was the root mean square (RMS) surface roughness value, the average deviation from the mean line of the sample surface. To show the most accurate and effective correlation between the surface roughness of the surfaces, the RMS surface roughness value will be discussed as the deviation better indicates the likely surface roughness for the remainder of the sample. After the evaluated area has been mapped, a surface profile is produced in a 2-D and 3-D map showing the surface roughness using a color gradient for the height of each peak and valley. All other surface profiles can be seen in Appendix C.

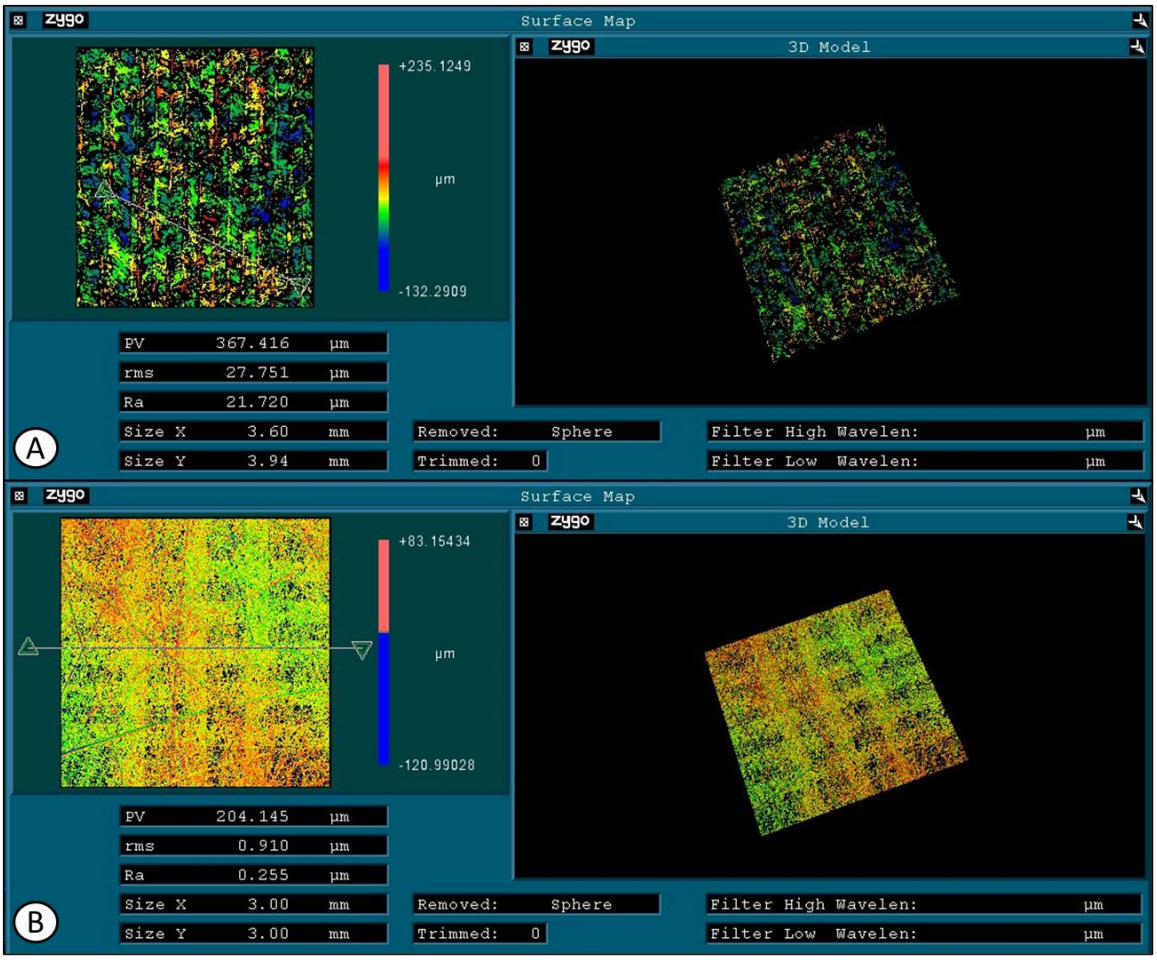

Figure 52. Surface Profile Maps From Zygo Optical Profilometer.
[A] As-Printed Pure Stainless-Steel Plate at 67 J/mm^3 Energy Density,
[B] Polished Pure Stainless-Steel Plate at 67 J/mm^3 Energy Density.

The as-printed sample profile map is not fully colored, indicated by the black voids. These voids are not voids in the sample (although the voids could be a result of a real volumetric defect at the surface) but voids in the data that is collected during scanning. This is due to the measuring process of the optical profilometer, which moves a set distance from the sample to move through a range of focus on the sample. Although the sample was measured across a range that far exceeded the expected focus range, the likely reason for gaps in the image is due to the inability of the scanning light and processing software to focus on those locations. Next to the 2-D map is a color scale that corresponds to the range of heights measured during the scan, with any red spots indicating the tallest microstructures that came into focus and the blue spots indicating the deepest valleys in the evaluated area.

1. As-Printed Plates

All the measurements collected for the as-printed sample plates were separated by the subset of data and plotted by the energy density that was associated with the print. Beginning with the peak-to-valley data, highlighting the greatest height differences across the evaluation area, a summary of the data can be seen in Figure 53. Generally, an upward trend in the peak-to-valley gap was observed with an increase in energy density. This increase was observed for both pure and composite samples with the largest increase in the gap occurring for the 3 vol% samples.

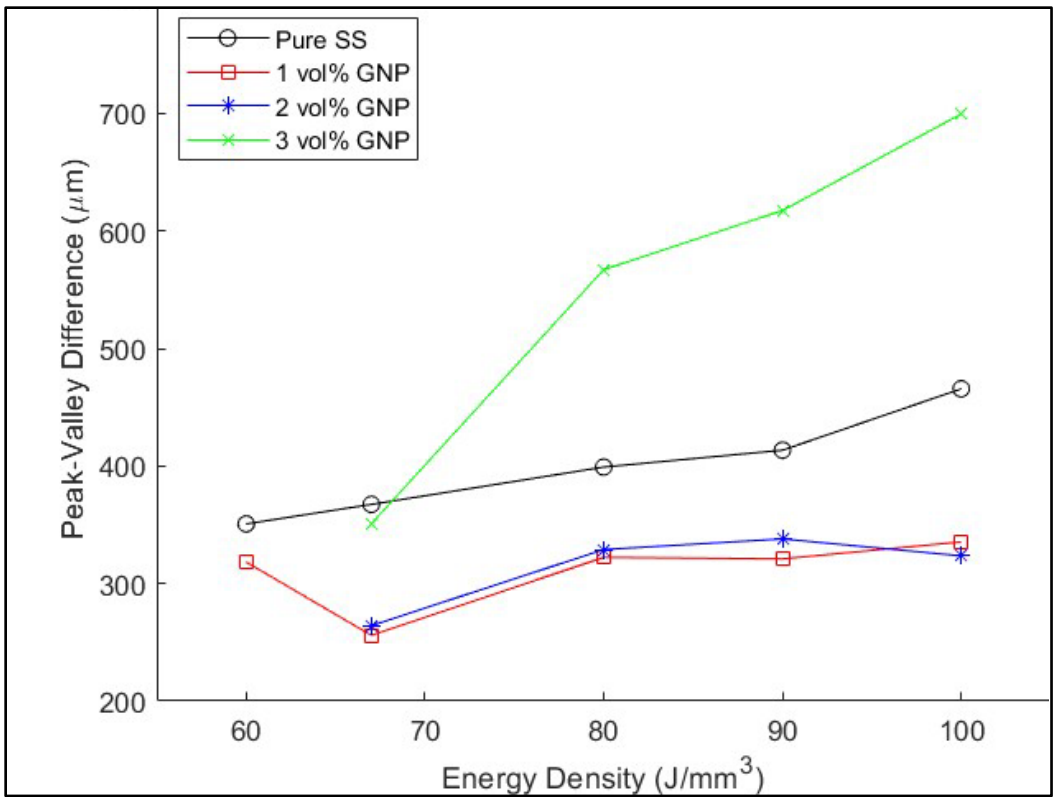

Figure 53. Peak-Valley Distance by Energy Density for As-Printed Samples.

The data shown provides an insight into the relationship between the 3-D metal printing process with a composite powder and the surface roughness of the final print sample. The 3 vol% GNP composite powder was the most difficult powder to print with due to the higher powder agglomeration within the powder hopper, restricting powder flow and reducing the probability that the print would successfully finish. Although the issues were corrected, the agglomerated powders could have led to larger void creation during the laser sintering process, resulting in a rougher surface with a greater peak–valley range on the final surface. To provide the most useful and accurate measure of surface roughness, the RMS roughness value must be analyzed, as seen in Figure 54.

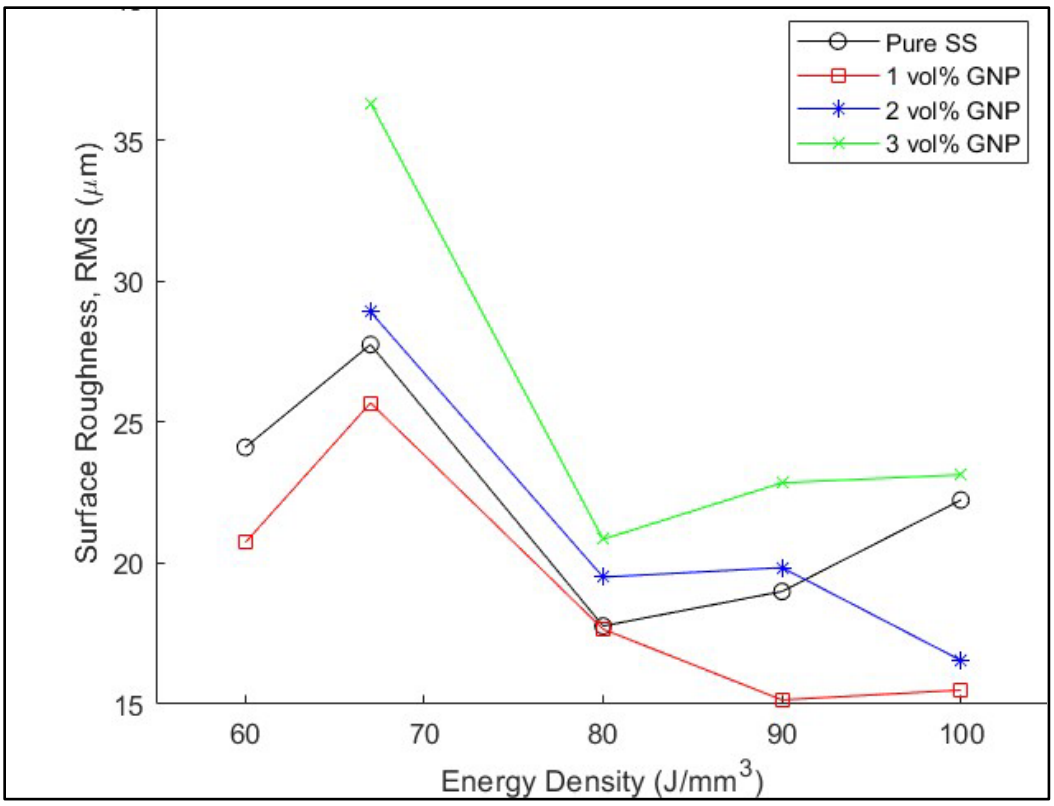

Figure 54. RMS Surface Roughness Measurements by Energy Density for As-Printed Samples.

As seen in the figure, the general trend for the RMS values appeared to decrease as the energy density increased, solidifying the earlier assumption that the higher energy density created a smoother surface as the sintering process likely affected a wider region with each pass, creating a smoother and more uniform surface. Comparing Figure 53 and Figure 54, it is clear with the 3 vol% GNP samples that even though the peak-valley value increased with the higher energy density, the true measure for the surface roughness decreased. This relationship is true for the other material composition samples as well. While the relationship for the other material composition samples is not as definitive as the 3 vol% GNP samples, there is an upward trend between the peak-valley value for the pure, 1 vol% GNP, and 2 vol% GNP samples in Figure 53. Contrary, as the relationship maintains, the surface roughness values decrease as the energy density increases, shown in Figure 54.

2. Polished Plates

All the polished plates were subjected to surface mapping to measure the surface roughness. The results for the peak-to-valley measurements and RMS surface roughness can be seen in Figure 55 and Figure 56, respectively.

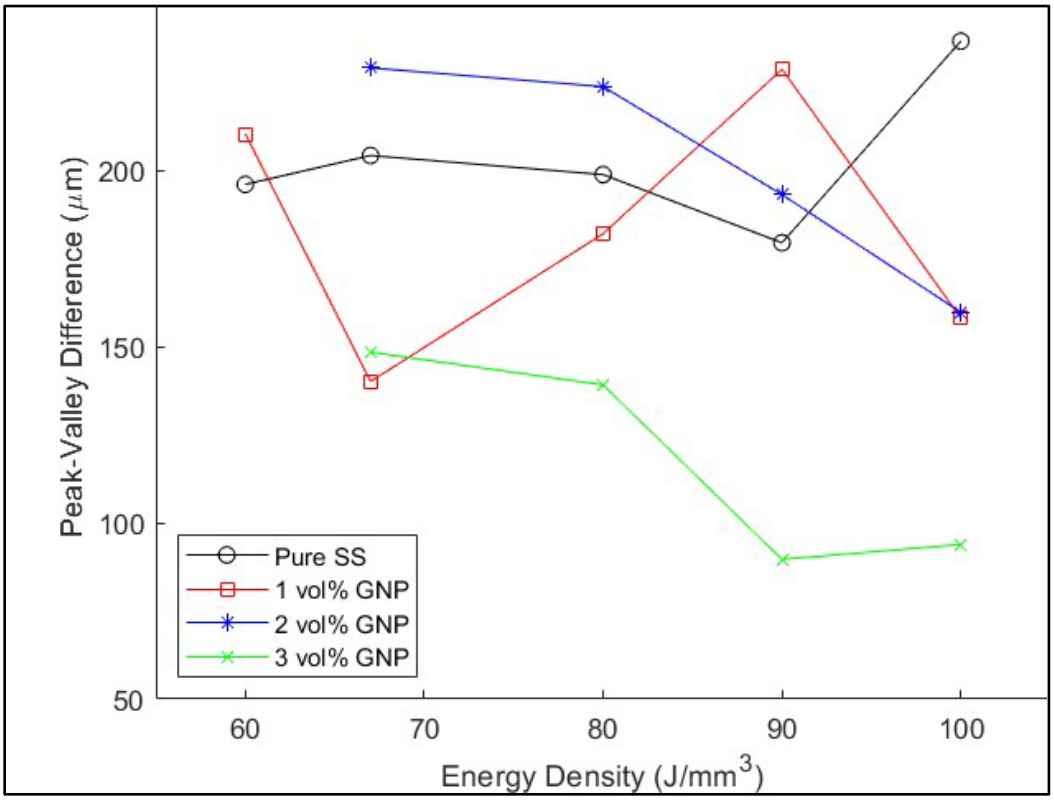

Figure 55. Peak-Valley Distance by Energy Density for Polished Samples.

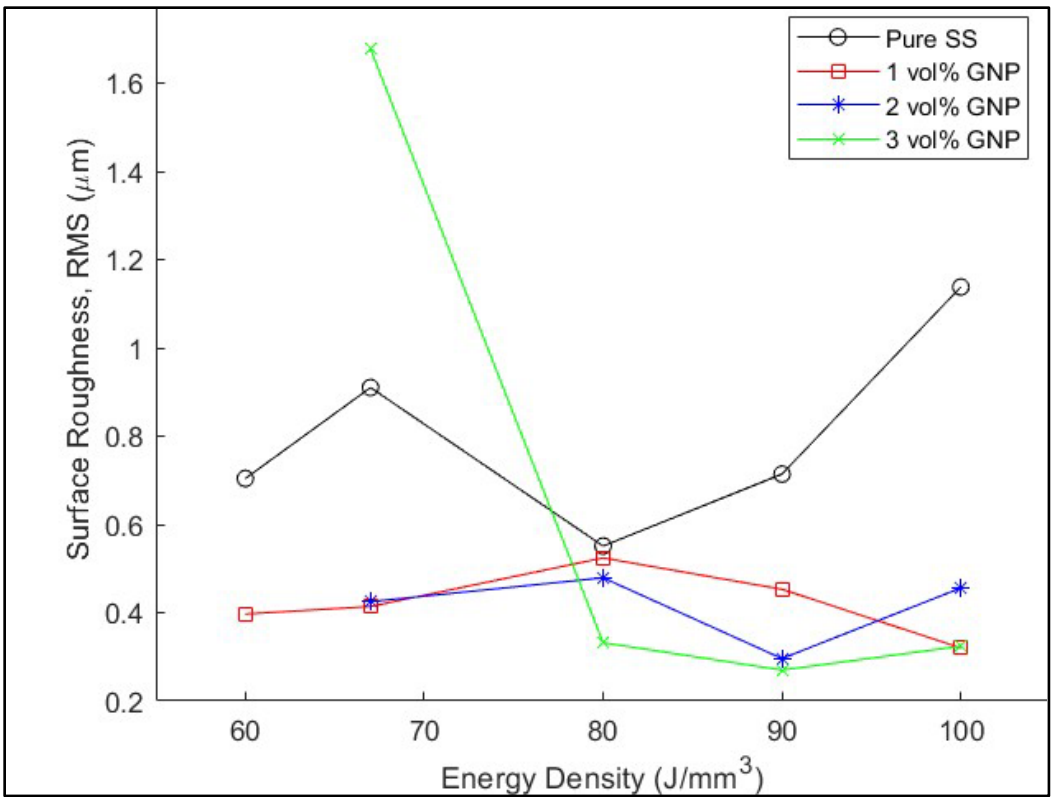

Figure 56. RMS Surface Roughness Measurements by Energy Density for Polished Samples.

The relationship between the peak-valley value and the RMS surface roughness measurements is not particularly strong for the polished samples until the scale of the values are taken into consideration. The range of values for the peak-valley measurement is might tighter than typically expected, with all the values under 250 µm. With the operation principle of the optical profilometer, the level of reflectivity of a sample surface can negatively affect the scanning light and camera, as there is a greater chance that a region on the sample does not effectively reflect the light in the right angle, leading to a false peak or valley being recorded. Because of this, the estimated maximum value for the peak-valley difference is set at 100 µm, roughly where the 3 vol% GNP samples were averaging. The RMS values gathered have a higher degree of confidence when considering the polishing process. The recorded values for the RMS surface roughness are what was expected, averaging roughly 0.5 µm. This expectation is generated from the polishing process, as the sample plates were polished using a micro-cloth with 0.5-µm abrasive

alumina powder being added during polishing to create a unform 0.5-µm surface for testing.

C. SUPPORTING TRENDS BETWEEN CONTACT ANGLE AND SURFACE ROUGHNESS MEASUREMENTS

When combining the data collected from the sessile drop contact angle test and the optical profilometer surface roughness measurements, a definite correlation between the material composition and the contact angle measured appears. The combined data can be seen in Figure 57.

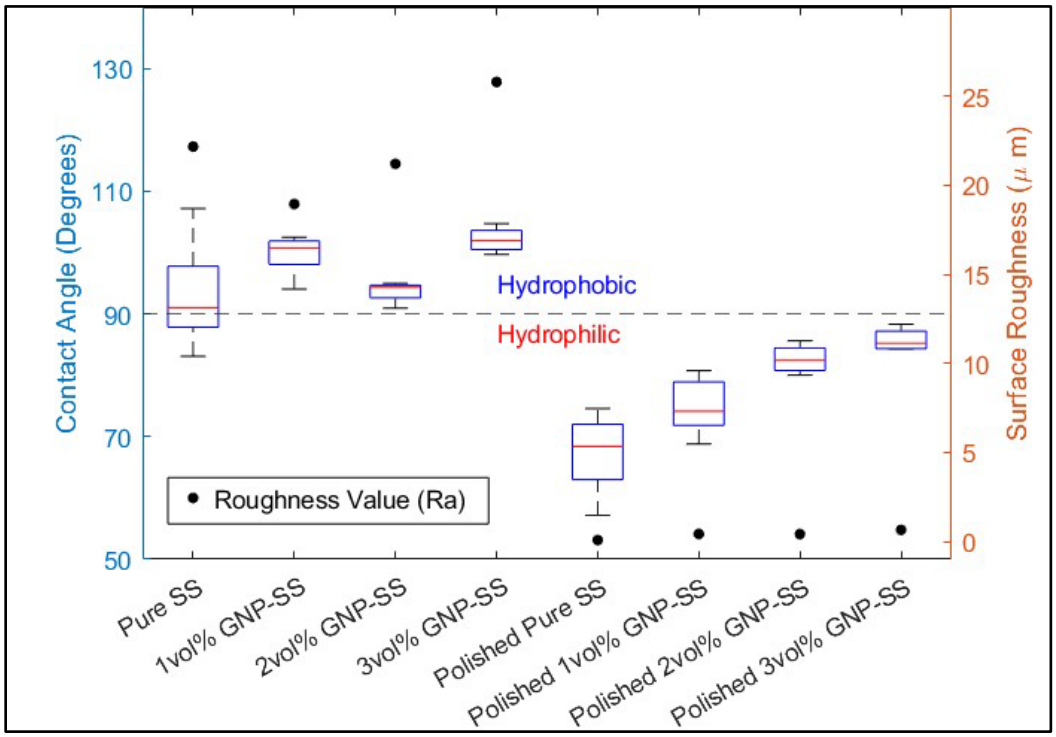

Figure 57. Contact Angle and RMS Surface Roughness by Material Composition.

Beginning with the as-printed data shown on the left half of the plot, the data suggests that there is a relationship between the surface roughness and the contact angle measured, but that the material composition is a stronger driving force in altering the contact angle of a surface. The box and whisker plots in Figure 57, contain the averages of

all the energy density prints of each material composition, ranging from 60 to 100 J/mm^3 and the plotted points are averages of the RMS roughness values for each energy density. When analyzing the right half of the plot, of the polished samples, the relationship between the surface roughness and the contact angle measured begins to falter, where the surface roughness for each sample was essentially removed and a smooth surface was attained. With the polished surface eliminating the surface roughness variable by ensuring that each surface was basically the same, the only variable remaining was the material composition with the volume concentration of GNP particles. Because of this, it can be determined that the GNP particles were the driving factor in increasing the contact angle in all the printed samples.

The data gathered can be compared to the Wenzel equation (2) with the determination of a hydrophobic or hydrophilic surface. One outcome of the Wenzel equation pertains to the behavior hydrophobic and hydrophilic surfaces as it relates to the surface roughness. For a hydrophobic surface, an increase in contact angle measurement is observed as the surface roughness increased. In contrast, a hydrophilic surface would have a lesser contact angle as the surface roughness increased. This principle stems from the assumptions made when applying the Wenzel equation, where the water drop is assumed to fully envelop the area it is placed upon, without an air pocket. A better equation to compare the data to is the Cassie-Baxter equation (4), where surface roughness and the interface between entrapped air bubbles are taken into consideration. The as-printed samples, as seen in Figure 57, have a surface roughness great enough to support a water drop and prevent wetting of the surface seen by the average contact angle exceeding the 90° hydrophobic threshold, a clear sign of hydrophobicity.

When the surface roughness variable is removed, as in the case of the polished samples, the baseline contact angle was within the hydrophilic region, well below 90°. However, contrary to the principle of hydrophilicity, the contact angle measure increased as the sample material composition was altered even with a surface roughness smooth enough to have a clearly hydrophilic surface. Although the contact angle measured for the 3 vol% GNP polished sample did not break the hydrophobic threshold, the roughly 20° average contact angle improvement indicates that the GNP particles were critical in the

creation or enhancement of a hydrophobic surface. These results stem from the assumptions made when applying the Wenzel equation, where the water drop is assumed to fully envelop the area it is placed upon, without an air pocket. With a smooth polished surface with the surface roughness effectively reduced to zero, the chance of a supportive air pocket is significantly lower than the as-printed samples.

THIS PAGE INTENTIONALLY LEFT BLANK

VI. CONCLUSIONS

The goal of this thesis was to investigate the possibility of creating a hydrophobic surface by adding graphene nanoplatelets (GNP) into a 316L stainless steel metal matrix. After experimentation, the data indicates that the addition of GNP particles did enhance the hydrophobicity of as-printed samples while also increasing the average water drop contact angle of the polished samples to a near-hydrophobic level.

Beginning with the high energy ball mill, the GNP particles were found to be evenly distributed throughout the stainless-steel particles, reducing deleterious effects of nanoparticle agglomeration. The composite powders did prove challenging during printing, as the relatively large and flakey GNP particles appeared to cluster while trapping the stainless-steel powder, requiring modification to the powder hopper to ensure smooth flow during printing. To ensure the presence of GNP particles within the printed samples, SEM imaging of print plate cross sections was conducted, showing a large presence of particles throughout the stainless-steel metal matrix. Sessile water drop contact angle testing showed that the inclusion of GNP particles in the standard stainless-steel powder did increase the average contact angle measurements for both the as-printed and polished samples, with the possibility of further improvements to the hydrophobicity with alternations to the powder composition or print procedure. Optical profilometry showed that while the increased surface roughness did improve the contact angles measured; but the surface roughness was not the only driving factor. As shown by the polished samples, with an average surface roughness of approximately 0.5 μm, the greatest influence on the contact angles measured was the material composition with the highest volumetric concentration of GNP particles reaching an almost hydrophobic state as compared to the standard stainless-steel samples which measured more than 20° less. The results gathered coincide with the Wenzel equation, where a greater surface roughness would lead to a greater contact angle when dealing with a hydrophobic surface.

With this information, it is plausible that stainless-steel and nanocomposite materials can be modified and experimented with for the creation of hydrophobic surfaces. Specifically, regarding GNP composite materials printed using the laser powder bed fusion

additive manufacturing technique, the baseline has now been established with the possibility to further improve upon the research in the future.

VII. FUTURE WORK

This chapter will outline a few potential experimental modifications that could improve and allow for the work with GNP composite materials with additive manufacturing technology to continue. The modifications presented have all been chosen with the understanding of the limitations and potential scope of the machinery currently available for use.

(1) Increased concentration of GNP particles within stainless steel powder

To further push the contact angles measured using sessile water drop testing, it is suspected that further increases in the concentration of GNP particles will be required. For the purposes of this thesis, the volumetric concentration of GNP particles was limited to 3 vol%. The potential for GNP and stainless-steel composite materials has not been fully explored, with higher concentrations needing to be tested to discover the true limitations of the carbon-based nanoparticle. Expected concerns with increasing the concentration of GNP particles revolve around the AM process used to create the samples, as the issues encountered with the 3vol% GNP composite powder would presumably increase as the concentration increased. Nevertheless, this should not be a barrier to further experimentation as methods for ensuring smooth distribution of powder during the printing process are numerous but have not yet been tested.

(2) Subject GNP particles to High energy ball milling prior to mixing with stainless steel powder

During the high energy ball milling process, the GNP particles and stainless-steel powder were added to a canister with 3 mm stainless steel balls to mix the powders together. The result of this was unnecessarily milled stainless-steel powder, which ultimately led to deformed stainless-steel particles. It is hypothesized that if the GNP particles were milled separately with the same operating parameters as were used in this thesis that the graphene stacks would break apart into thinner individual layers which could then be added to the stainless-steel powder, where the graphene could then evenly coat every stainless-steel particle. The goal of this modified high energy ball milling method

would be to expectantly coat every particle which would then remove the issues faced during the printing process.

(3) Introduce another nanomaterial to the gnp and stainless-steel composite mix

Graphene based nanomaterials have been greatly researched for the inherent hydrophobic tendencies. While GNPs have already shown great promise in the improvement and creation of hydrophobic surfaces, there is a potential that the addition of another nanomaterial could reinforce any shortcomings of GNP particles. Potential additions to the GNP and stainless-steel composite mix include carbon nanotubes or Buckminsterfullerene nanospheres both of which are different molecular configurations of carbon molecules. In addition to this, the implementation of silicon-based nanoparticles could also be researched.

APPENDIX A: EOS INSTRUCTIONS FOR USING MANY ENERGY DENSITIES WITHIN THE SAME PRINT

This appendix serves to clarify the instructions provided for printing parts with multiple laser parameters using the EOS M100 3-D metal printer. The set of instructions that this modifies is originally titled "Multiple Different Laser Parameters in a Single Print," found in the instruction booklet for the EOS M 100 printer.

1. Load Parts into EOSPRINT.

   Group parts by the exposure parameters that each will be printed under, writing down where the samples are located relative to the front of the printer and the name of each file. This will help in further steps and will prevent confusion when removing the build plate and wondering which samples have been printed at each print density.

2. Process → Exposure Parameters

3. Under "Exposure Type," select **_Default_DirectPart**

4. In "New Exposure Type," type name of your new exposure parameter (i.e., EnergyD_80_Direct)

   It is recommended to include the exposure type (Direct) in the name of the new parameter to ensure the print is successful.

5. Select **New** (your previously created parameter will appear in the **ExpPar** list.

6. Repeat steps 3–5 for each new exposure parameter desired.

7. Click **Apply**, **OK**

8. Under "Exposure Type," select **_Default_OuterSkin_DirectPart**

9. In "New Exposure Type," type name of your new exposure parameter (i.e., EnergyD_80_Skin)

   It is recommended to use a similar name as used for the direct exposure parameter.

10. Select **New** (your previously created parameter will appear in the **ExpPar** list.

11. Repeat steps 8–10 for each new exposure parameter desired, ensuring to match one new skin exposure parameter for every direct part exposure parameter.

12. Click **Apply**, **OK**

13. Process → Job Parameters

14. Create groups for each new energy density, adding the part and support wall, and support volume files. **Click Apply.**

    To make each group, right click below the last part file, and select group. To add files to each names group, click on each file, right click, "Cut,' right click on the group name, "Paste." Alternatively, files can be added to groups by dragging each file to the group, knowing that after the first file has been added to the group, subsequent files must be dragged below the previous file to ensure the file is added to the correct group. For each part to be printed, three files are created: "**PartName_SupportWalls_0m**," "**PartName_p**,' and "**PartName_SupportVolumes_p**." The order of files under each group must follow the preceding order, or there is a likelihood that the supports generated will not print, causing a process failure. See image below for example.

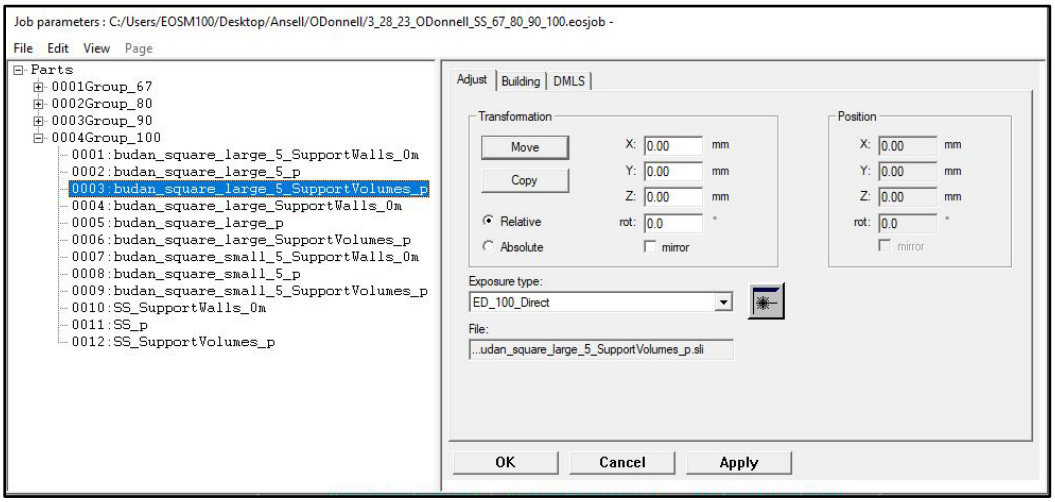

15. Select one of the energy density groups created, (i.e., 0001Group_80). Under **Exposure Type**, select the corresponding Direct exposure parameter previously created.

    This applies the same exposure type to each file in the group. Click the [+] box for each energy density group to expand and verify the exposure type has been applied to each file. For every "PartName_SupportWalls_0m" file, the exposure type must be manually corrected to "**_Default_ExternalSupport**" to ensure generated supports successfully print.

16. Click on a "**PartName_p**' or "**PartName_SupportVolumes_p**" file, and next to Exposure type, click the  button.

17. For each direct exposure parameter, under "**Skin/core**," the exposure types should match the following image, ensuring that the Skin exposure type is the same as created to match the direct exposure parameter. Click **Apply** after each direct exposure parameter is fully adjusted to match the image.

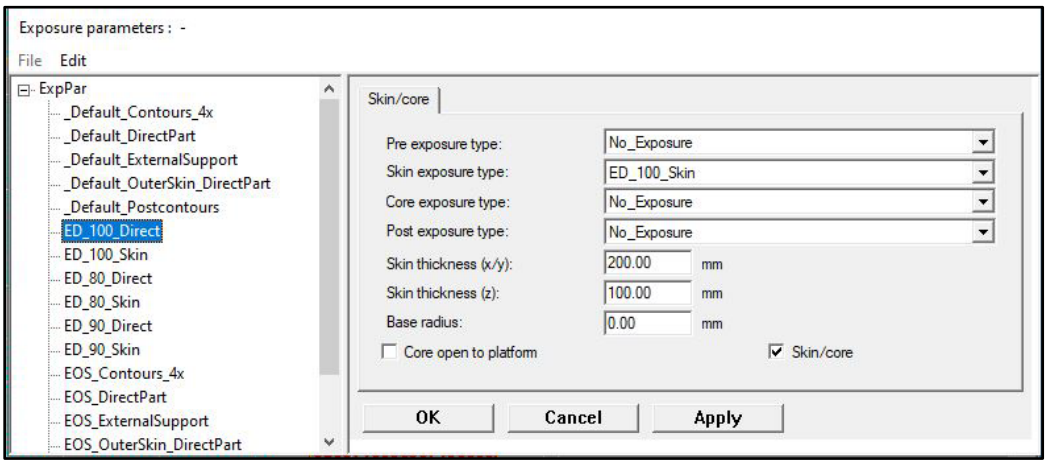

18. Once done with each direct exposure parameter, click on the Skin parameter that corresponds to each direct exposure parameter.

19. Under the **Stripes** tab, adjust the energy density parameters desired. Click **Apply**. See the following image for example.

    For the best results, ensure that the **X** and **Y** hatching options as well as **Alternating** are checked under the Stripes tab.

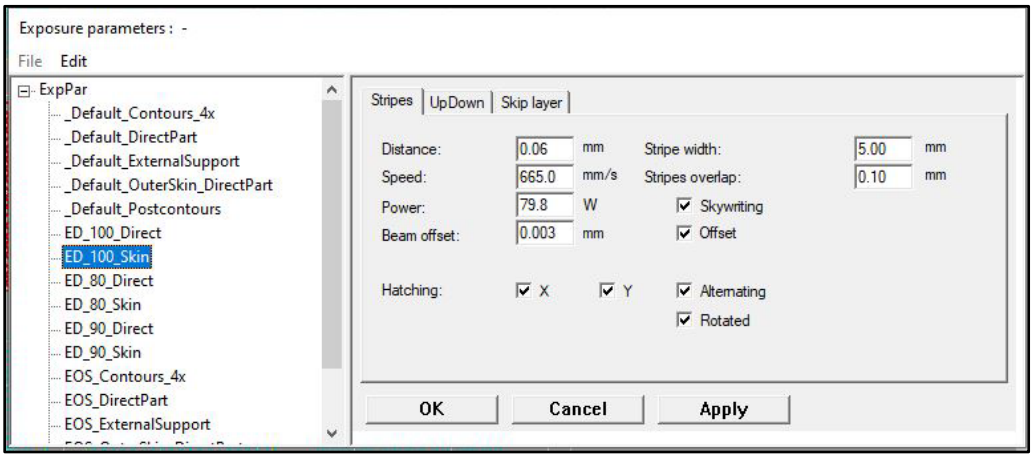

20. Under the **UpDown** tab, adjust parameters as needed. See image below for example. It is recommended to adjust **Upskin** values to the same as **Stripes**, while leaving the **Downskin** parameters as originally set.

    For best results, the **Alternating** option should be unchecked for the **Upskin** parameters and checked for the **Downskin** parameters.

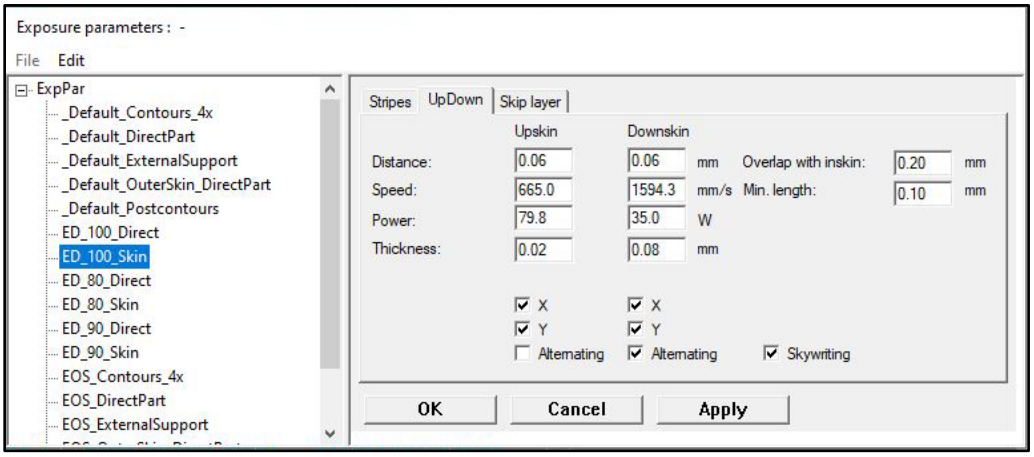

21. Click **Apply**, **OK**.

When this is complete, the normal uploading process to the printer can continue.

APPENDIX B: SESSILE WATER DROP PHOTOS

Standard Stainless-Steel (60 J/mm^3) Energy Density

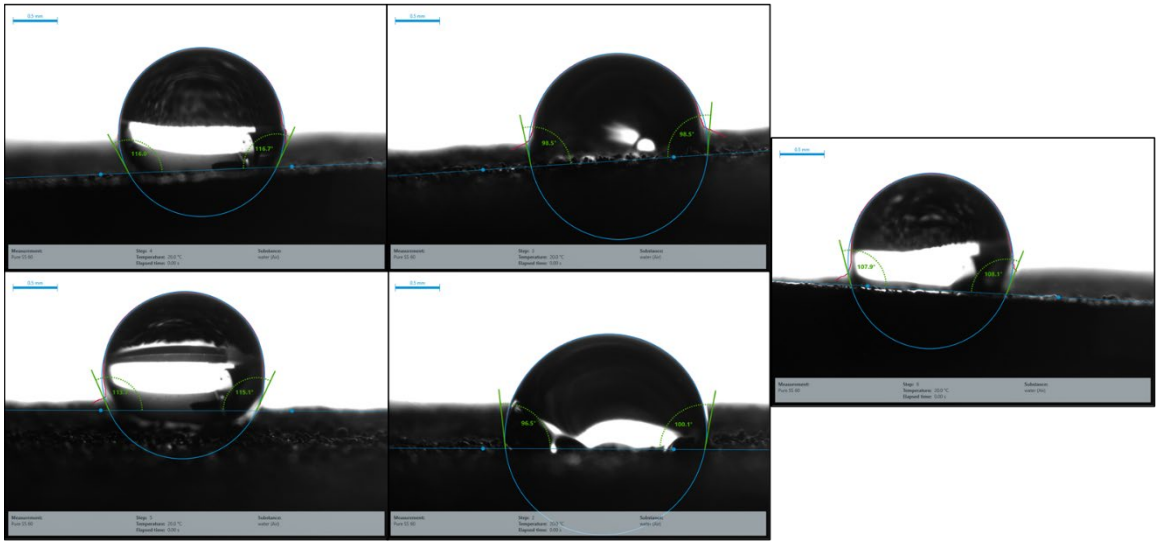

Standard Stainless-Steel (67 J/mm^3) Energy Density

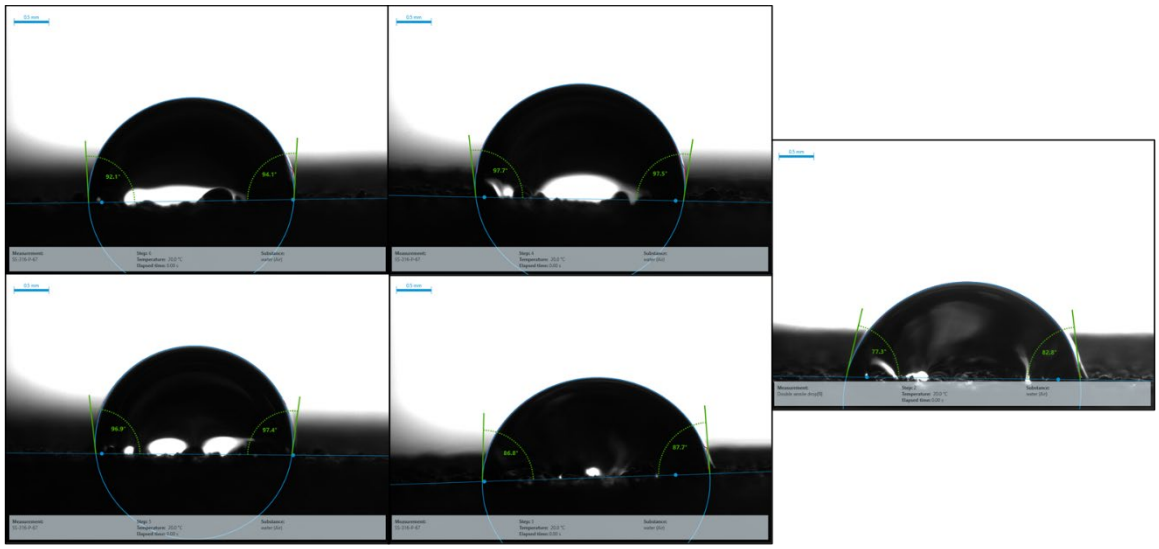

Standard Stainless-Steel (80 J/mm^3) Energy Density

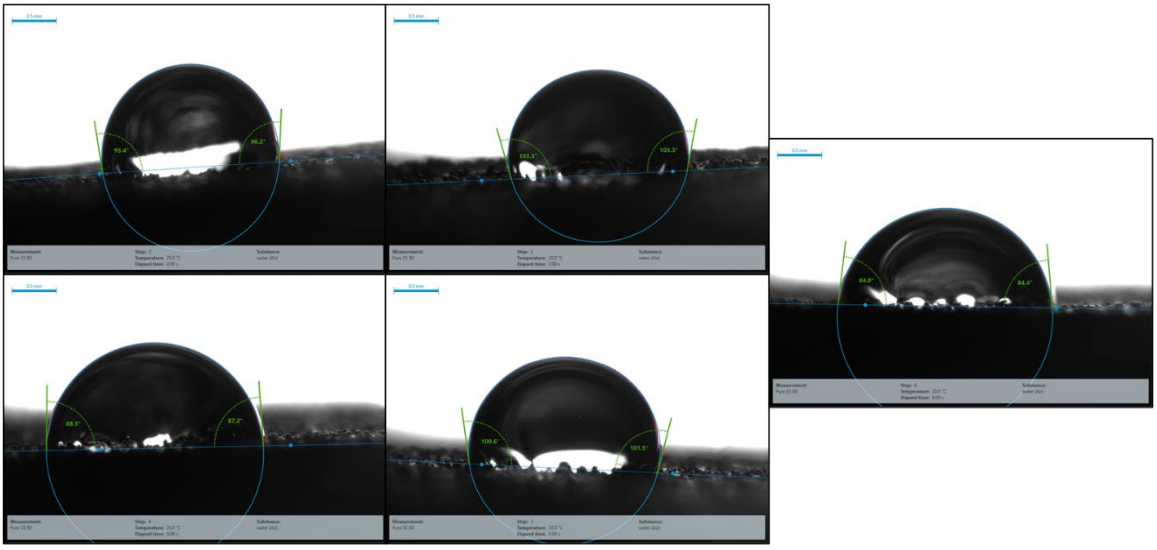

Standard Stainless-Steel (90 J/mm^3) Energy Density

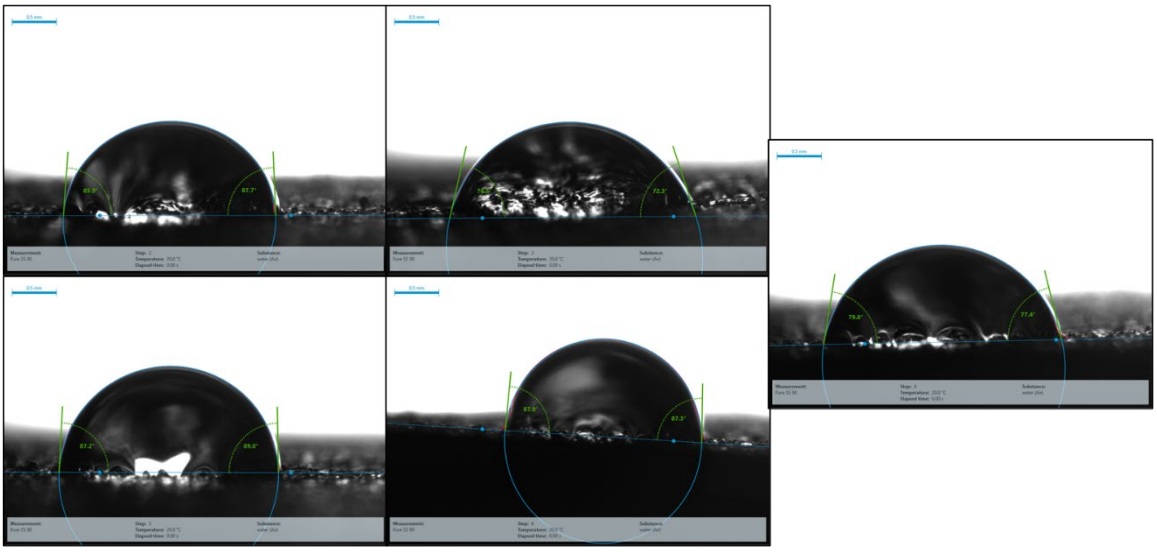

Standard Stainless-Steel (100 J/mm^3) Energy Density

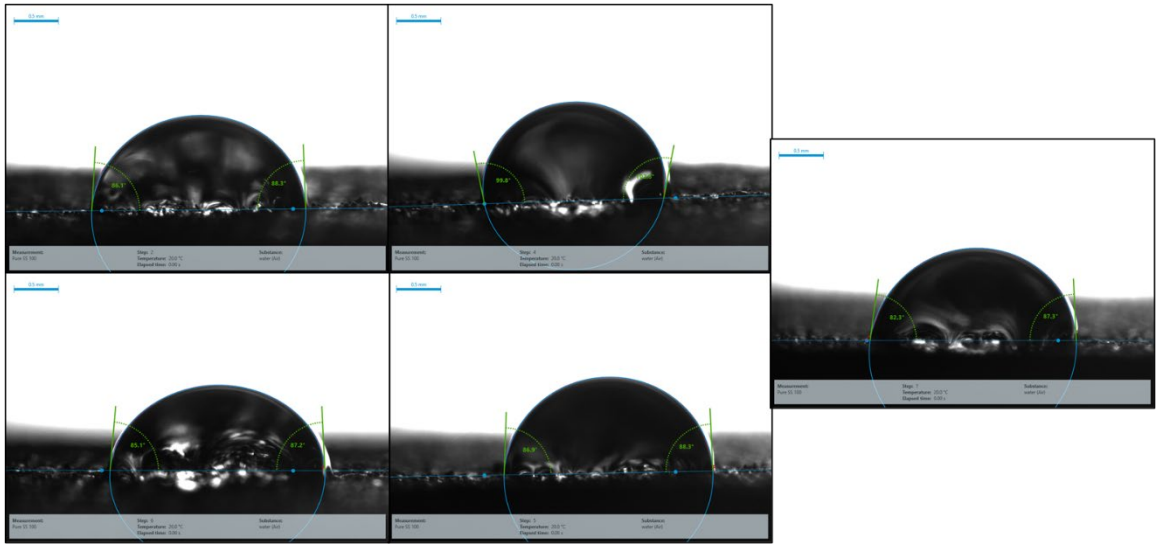

1 vol% GNP Stainless-Steel (60 J/mm^3) Energy Density

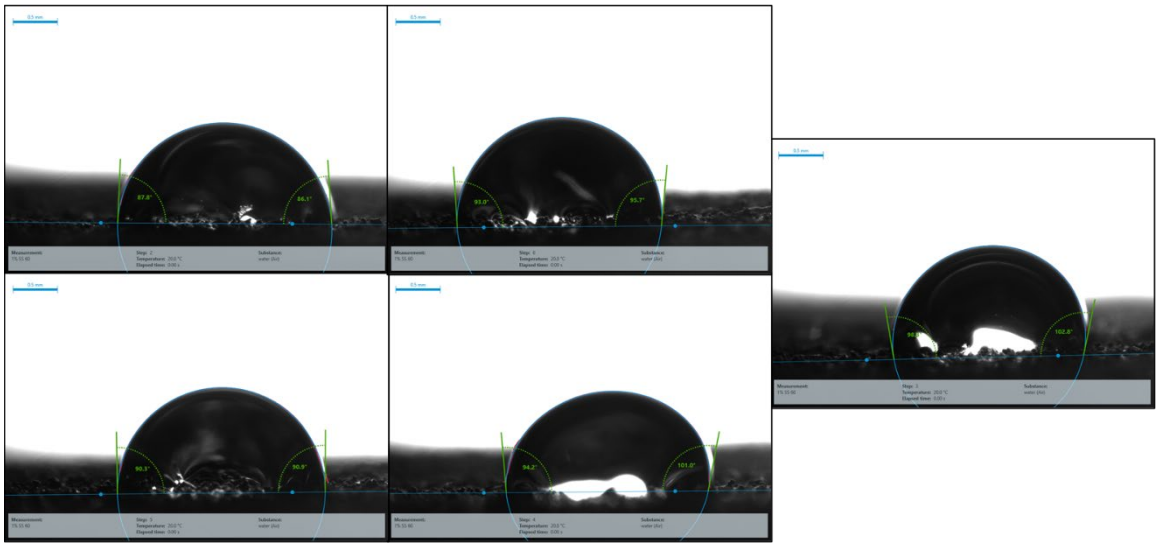

1 vol% GNP Stainless-Steel (67 J/mm^3) Energy Density

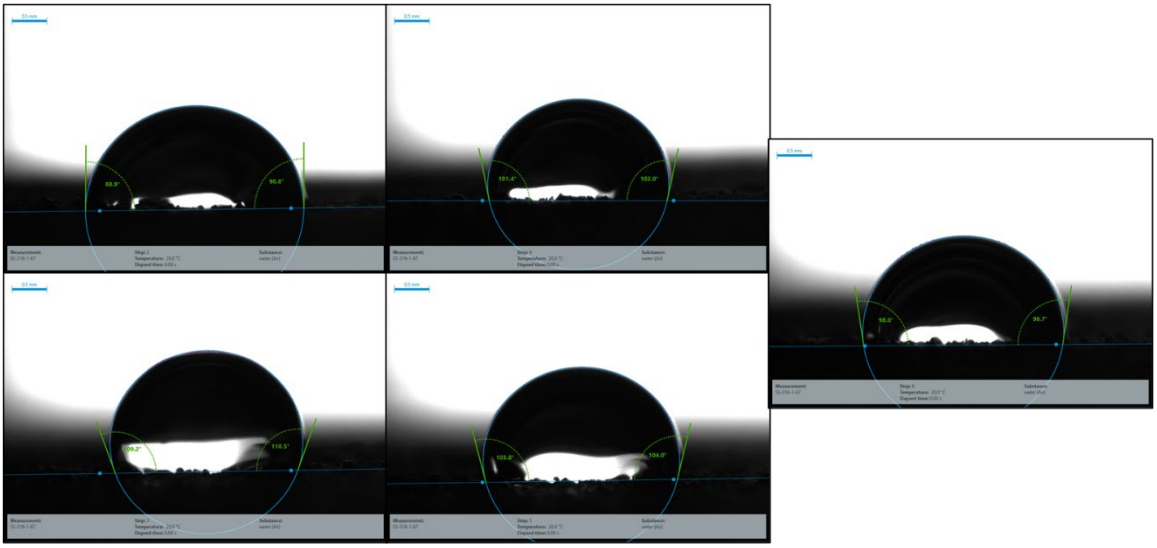

1 vol% GNP Stainless-Steel (80 J/mm^3) Energy Density

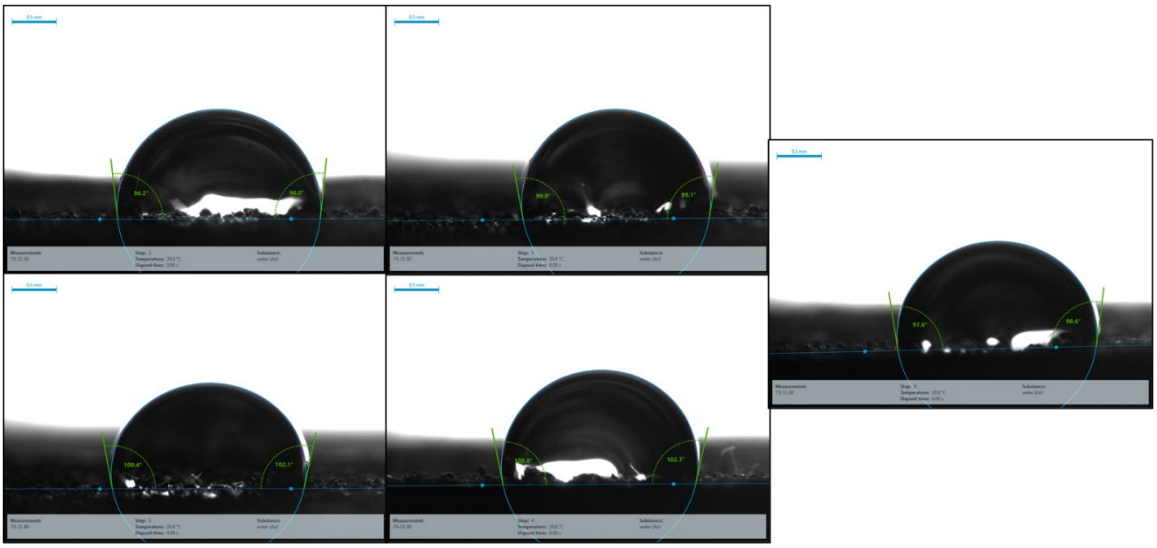

1 vol% GNP Stainless-Steel (90 J/mm^3) Energy Density

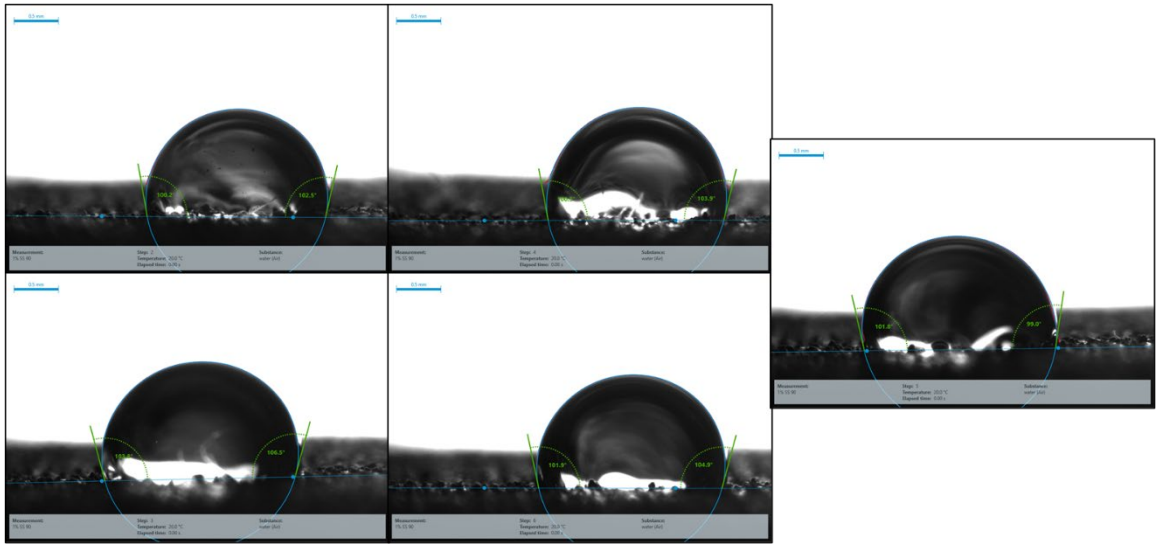

1 vol% GNP Stainless-Steel (100 J/mm^3) Energy Density

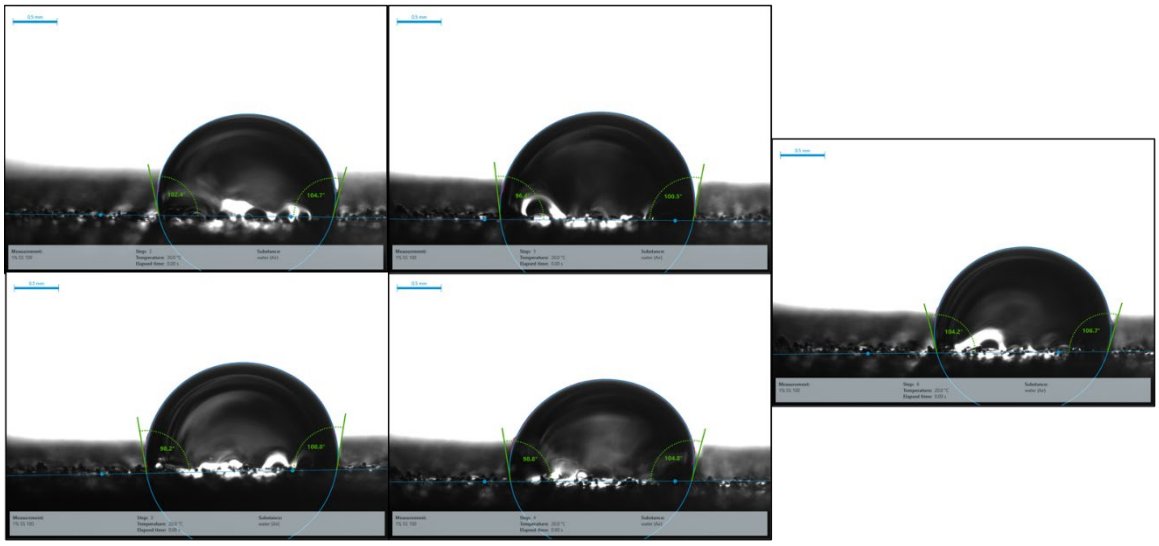

2 vol% GNP Stainless-Steel (67 J/mm^3) Energy Density

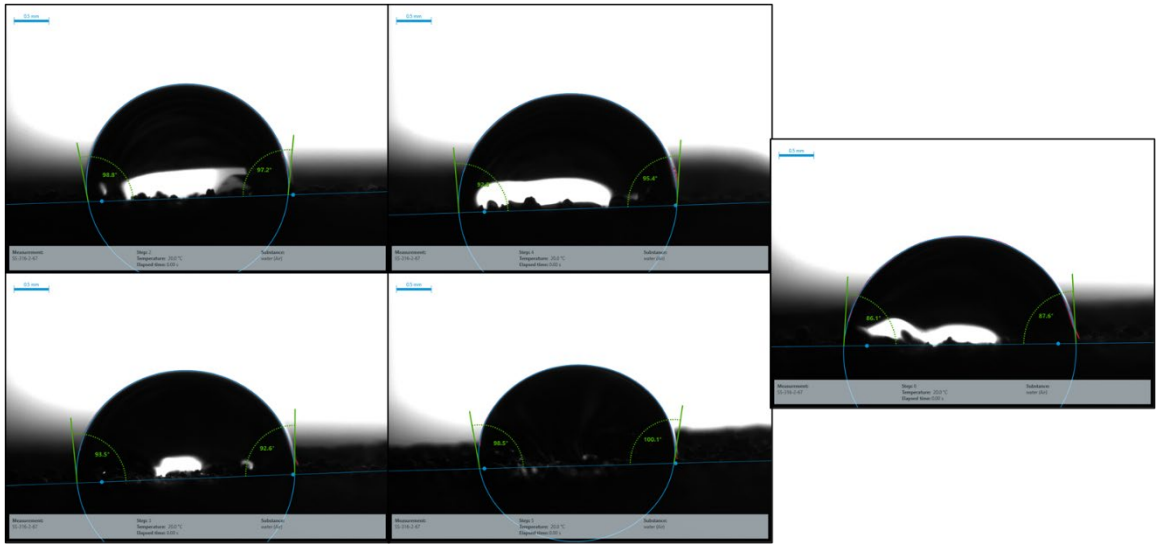

2 vol% GNP Stainless-Steel (80 J/mm^3) Energy Density

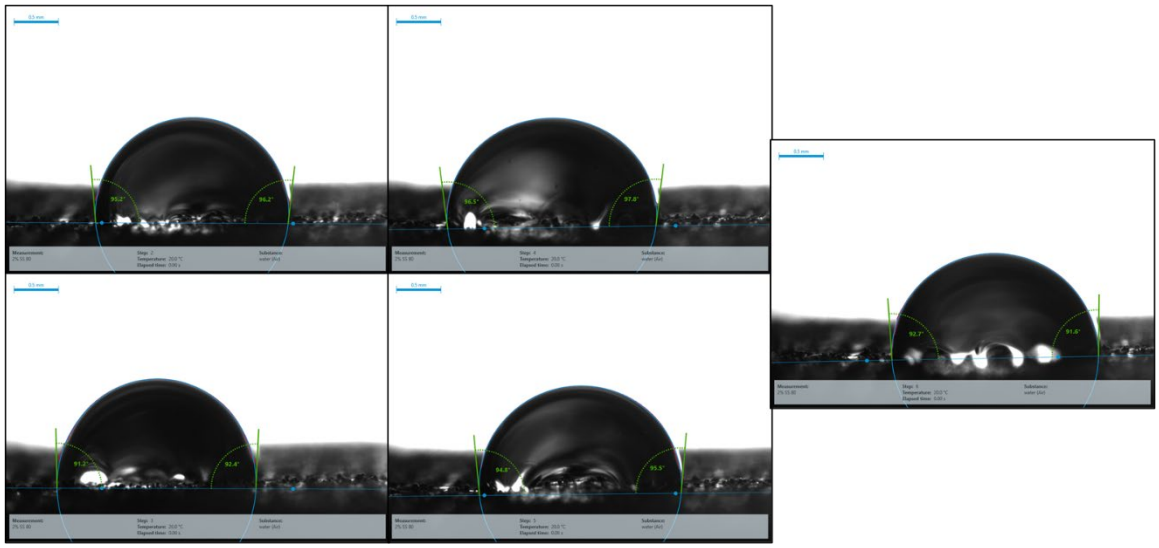

2 vol% GNP Stainless-Steel (90 J/mm^3) Energy Density

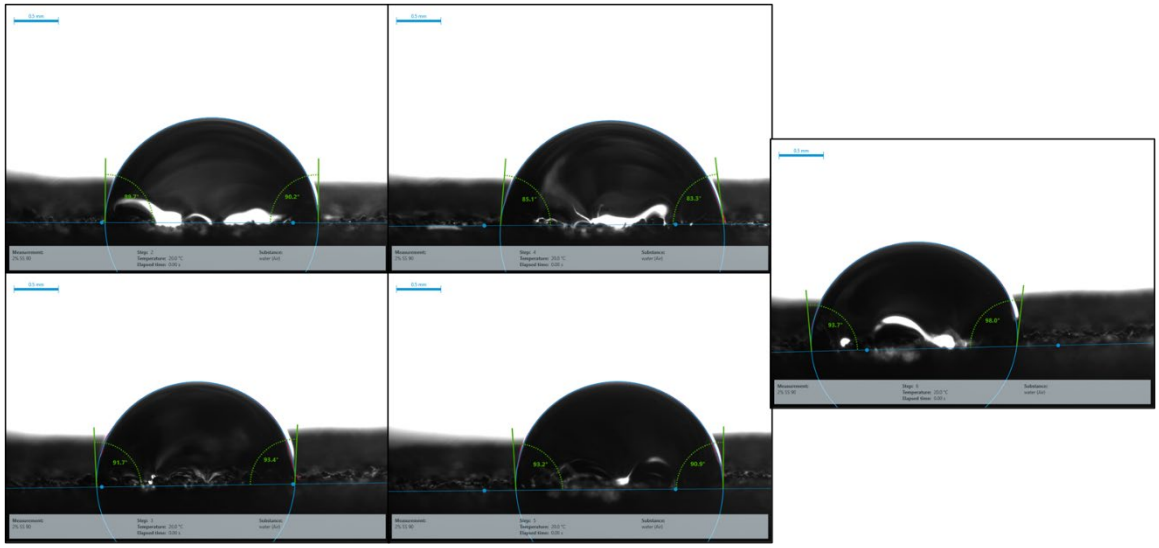

2 vol% GNP Stainless-Steel (100 J/mm^3) Energy Density

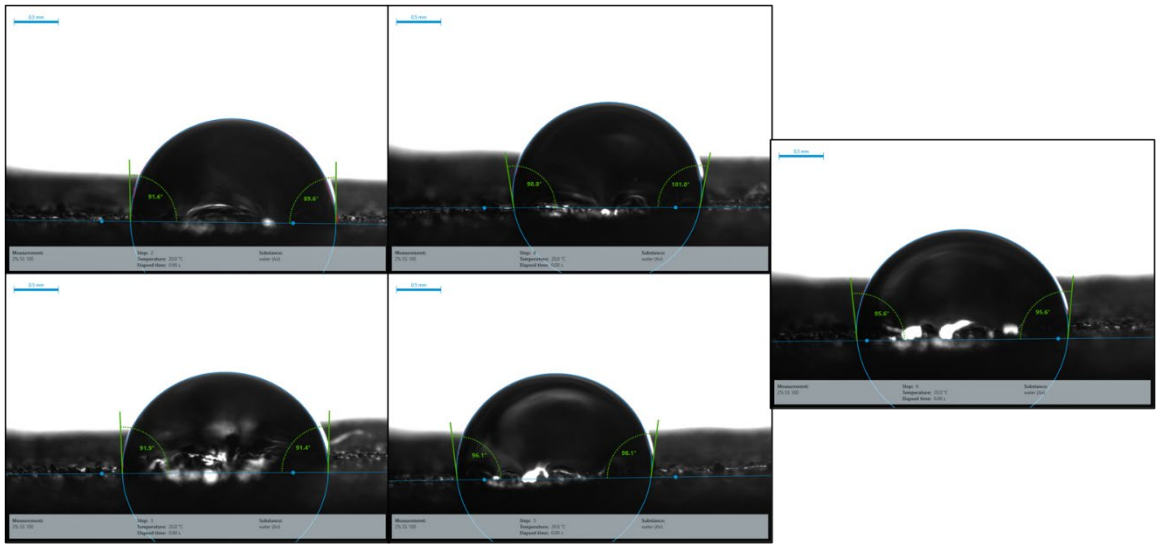

3 vol% GNP Stainless-Steel (67 J/mm^3) Energy Density

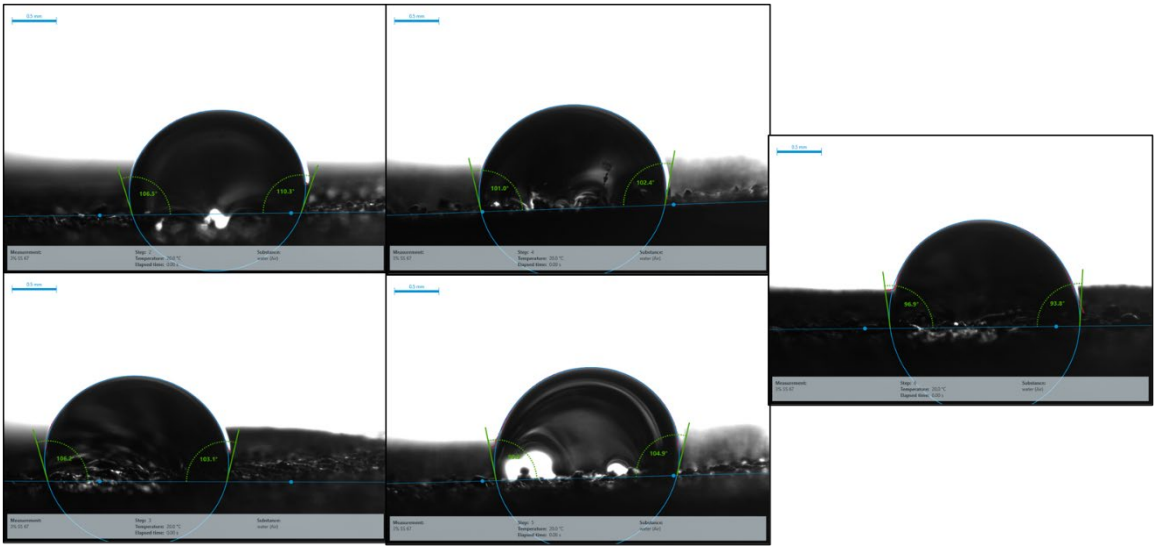

3 vol% GNP Stainless-Steel (80 J/mm^3) Energy Density

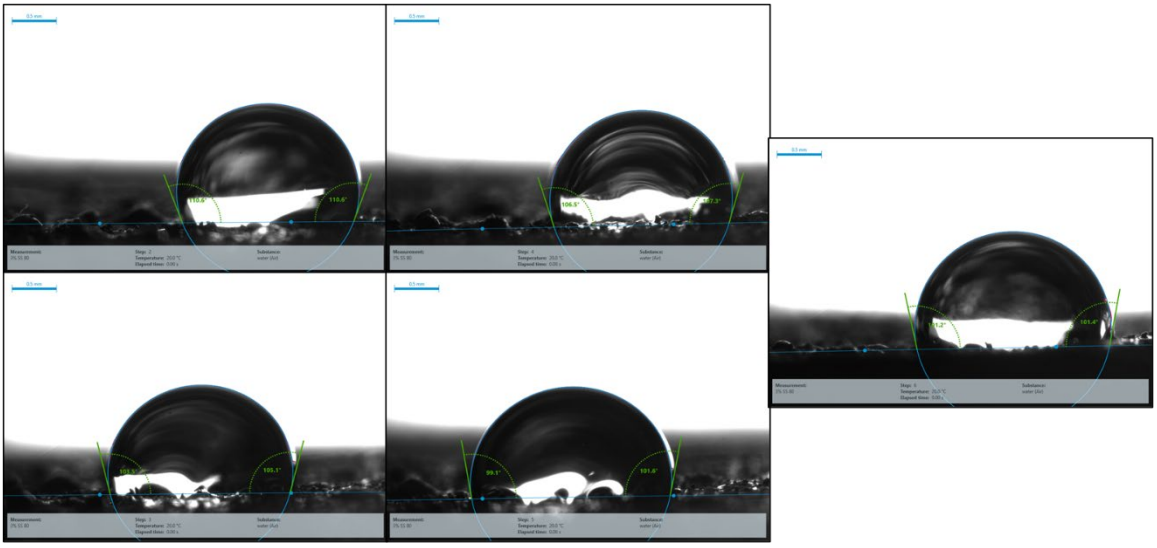

3 vol% GNP Stainless-Steel (90 J/mm^3) Energy Density

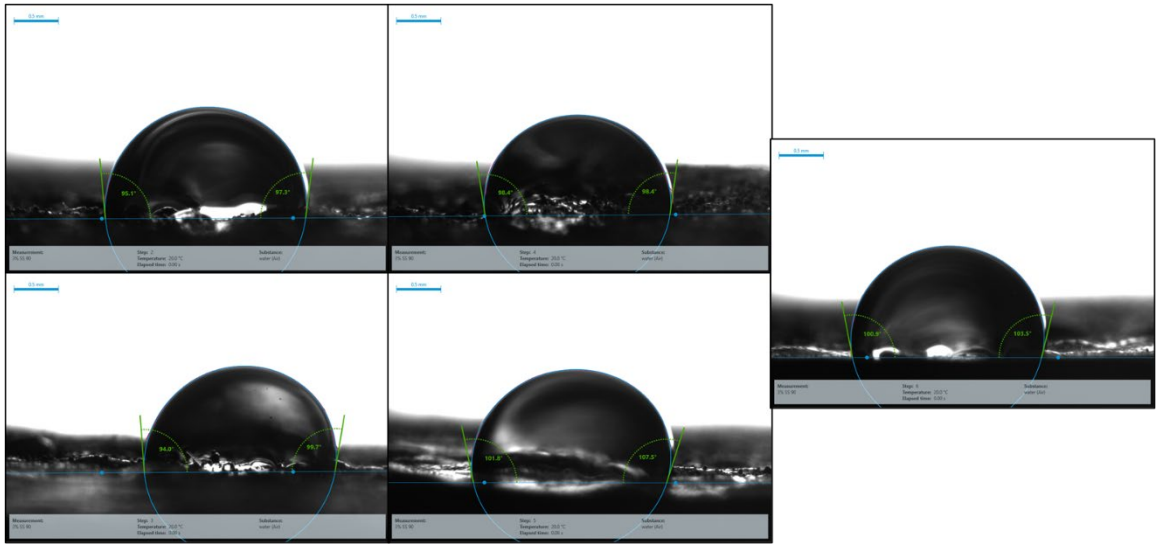

3 vol% GNP Stainless-Steel (100 J/mm^3) Energy Density

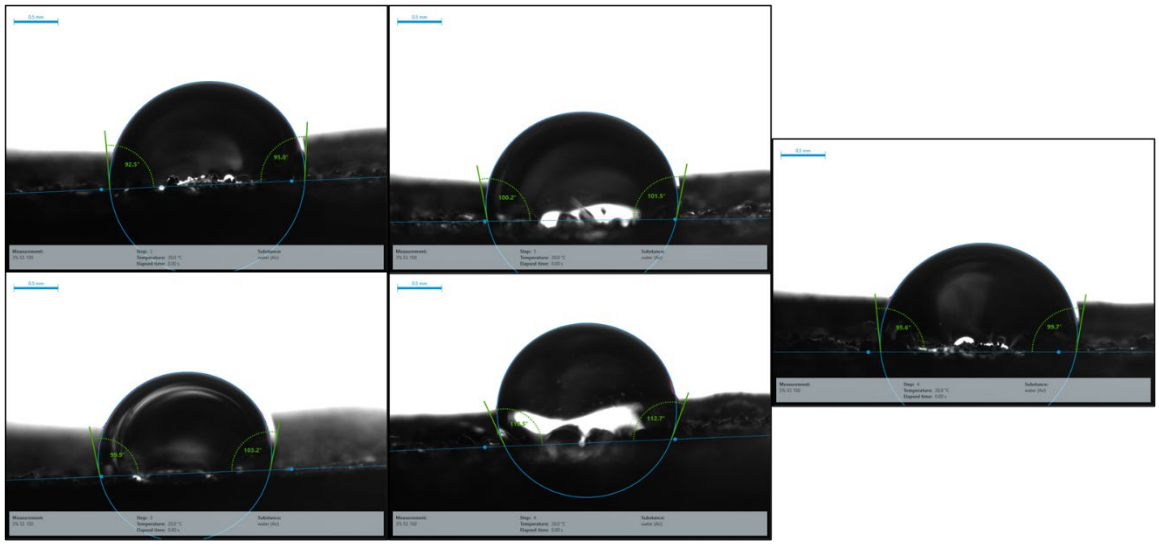

Polished Standard Stainless-Steel (60 J/mm^3) Energy Density

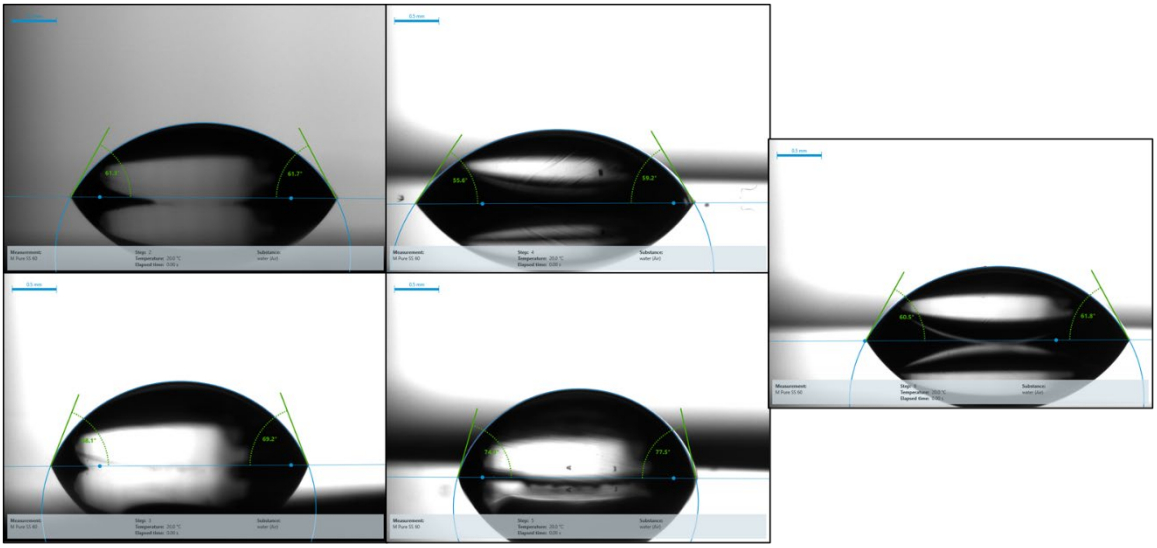

Polished Standard Stainless-Steel (67 J/mm^3) Energy Density

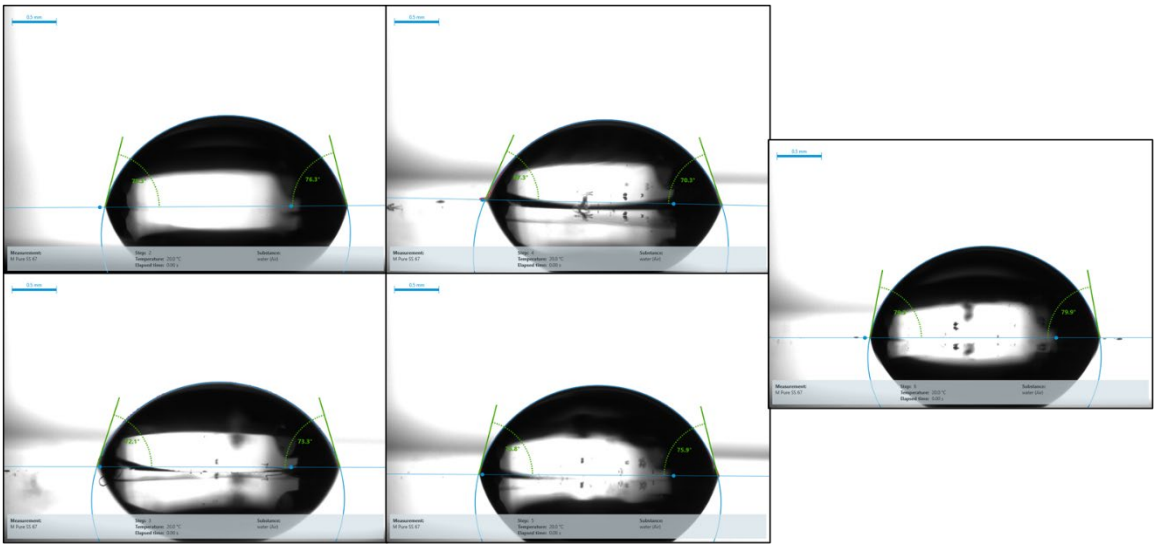

Polished Standard Stainless-Steel (80 J/mm^3) Energy Density

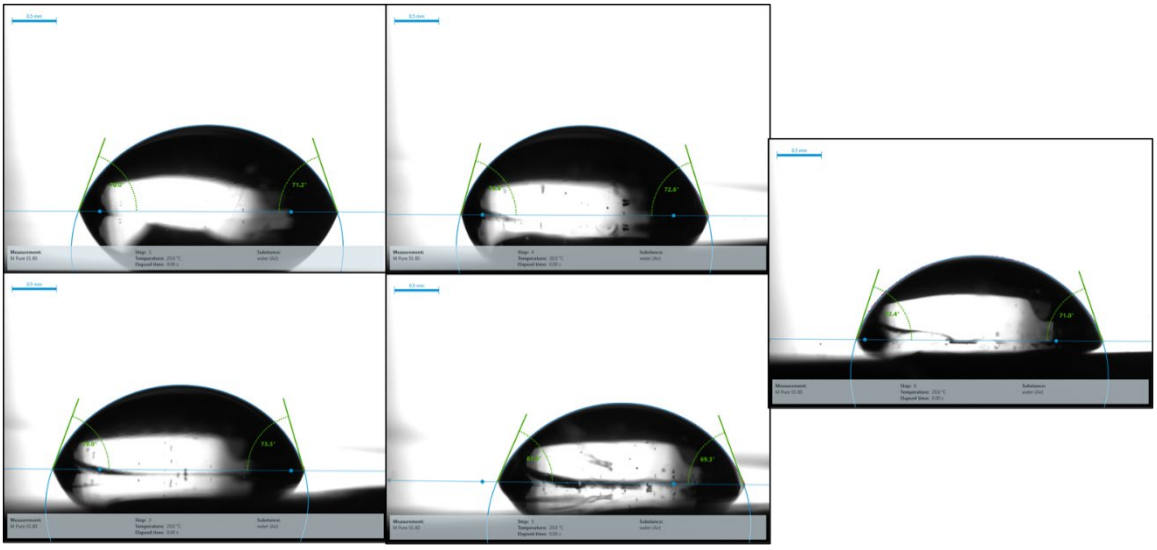

Polished Standard Stainless-Steel (90 J/mm^3) Energy Density

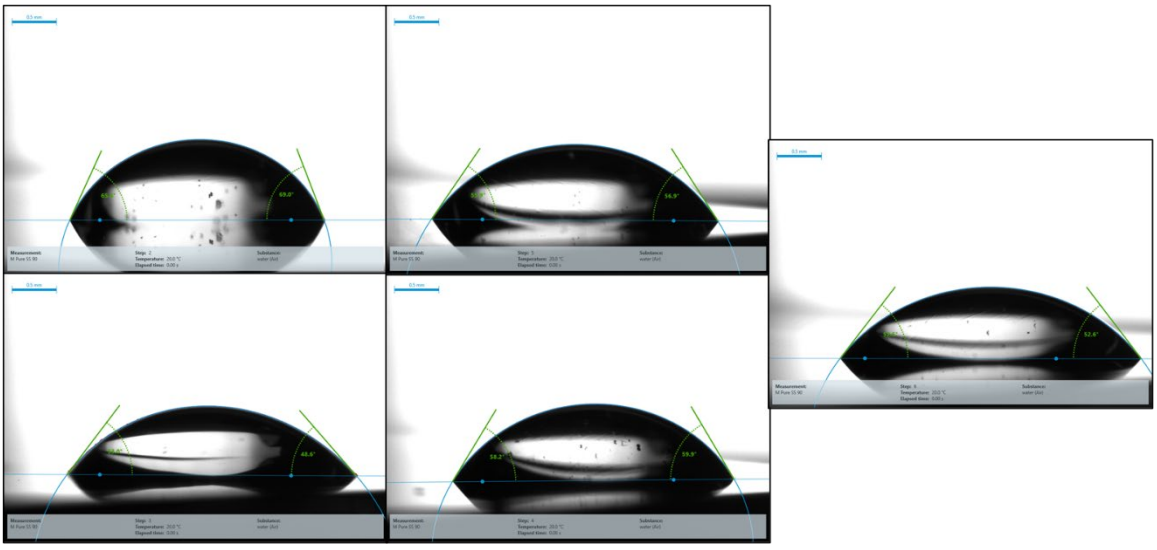

Polished Standard Stainless-Steel (100 J/mm^3) Energy Density

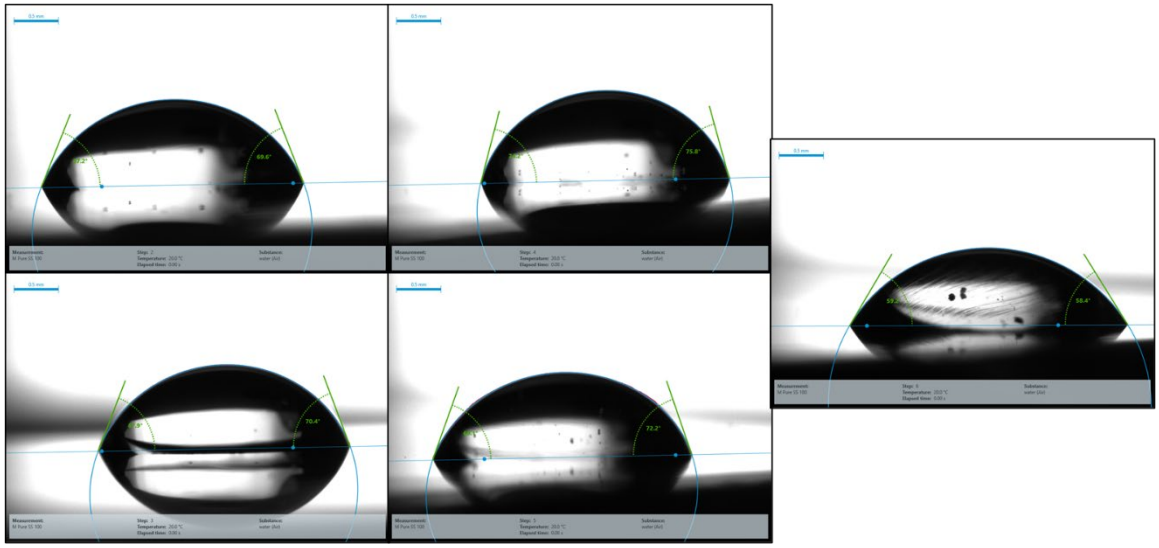

Polished 1 vol% GNP Stainless-Steel (60 J/mm^3) Energy Density

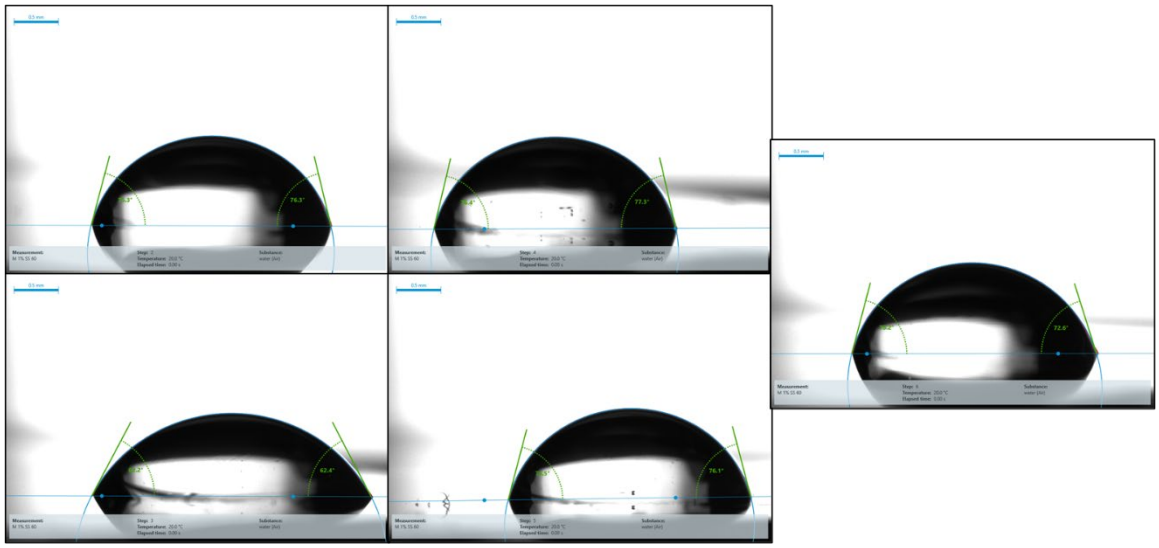

Polished 1 vol% GNP Stainless-Steel (67 J/mm^3) Energy Density

Polished 1 vol% GNP Stainless-Steel (80 J/mm^3) Energy Density

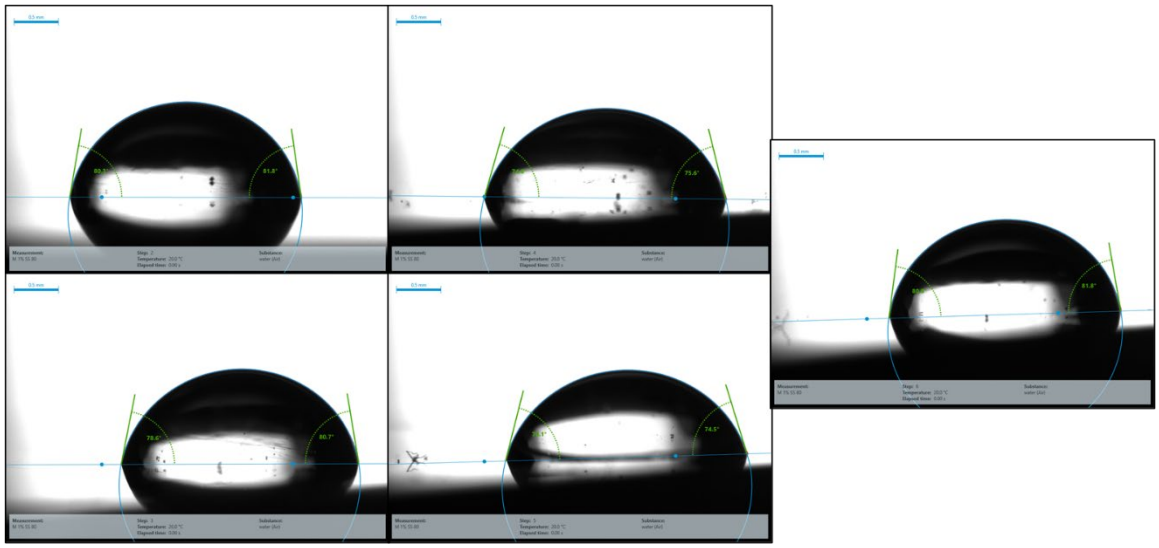

Polished 1 vol% GNP Stainless-Steel (90 J/mm^3) Energy Density

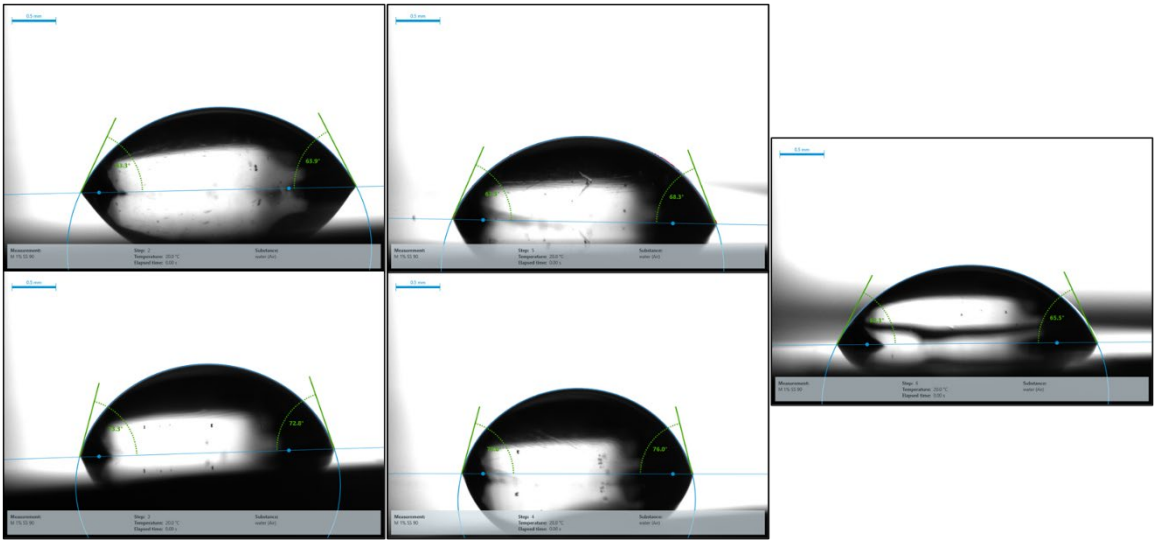

Polished 1 vol% GNP Stainless-Steel (100 J/mm^3) Energy Density

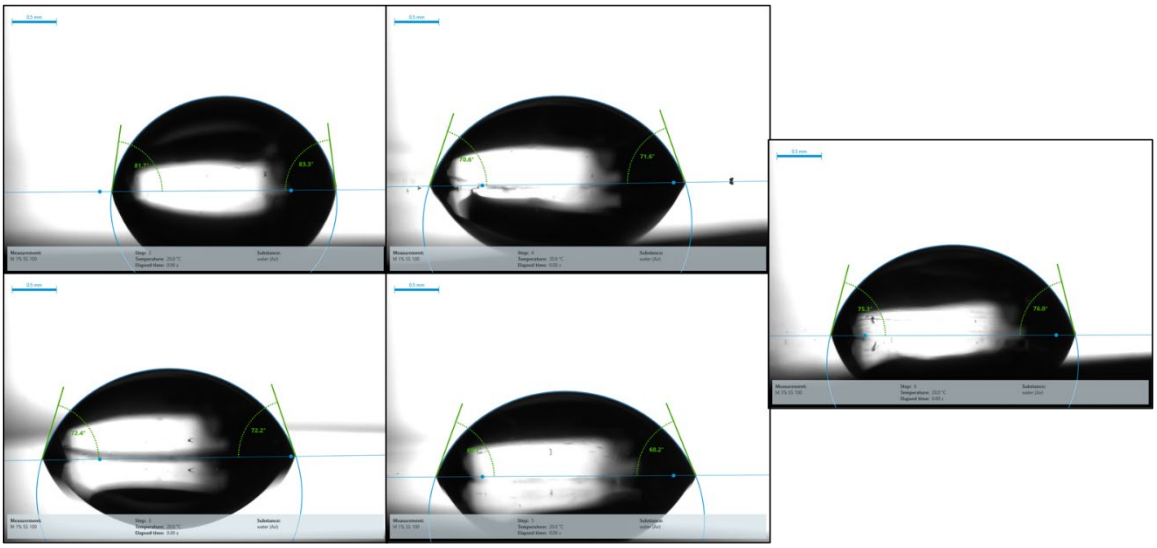

Polished 2 vol% GNP Stainless-Steel (67 J/mm^3) Energy Density

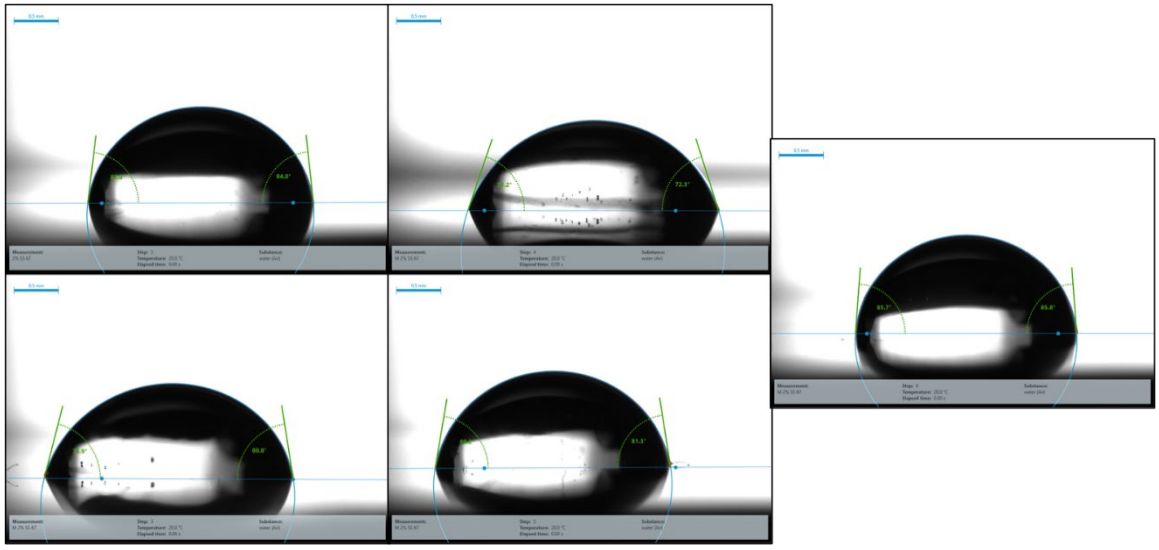

Polished 2 vol% GNP Stainless-Steel (80 J/mm^3) Energy Density

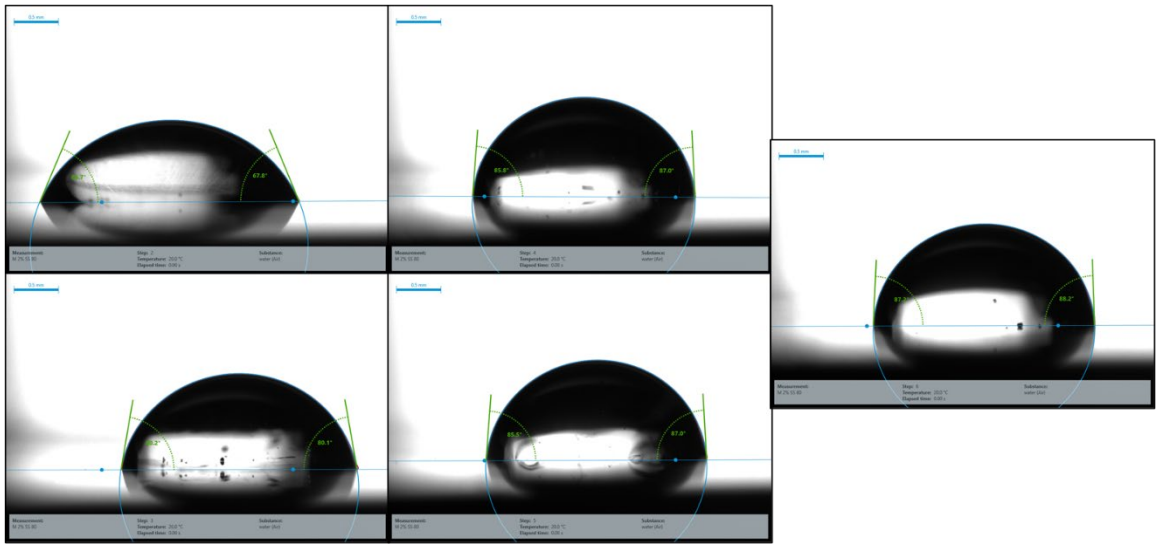

Polished 2 vol% GNP Stainless-Steel (90 J/mm^3) Energy Density

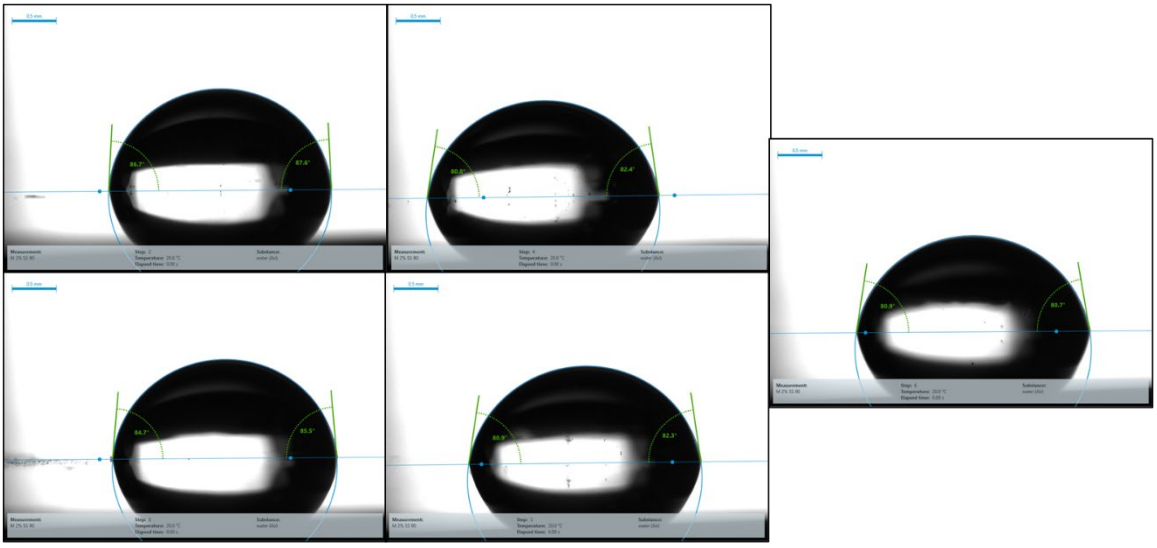

Polished 2 vol% GNP Stainless-Steel (100 J/mm^3) Energy Density

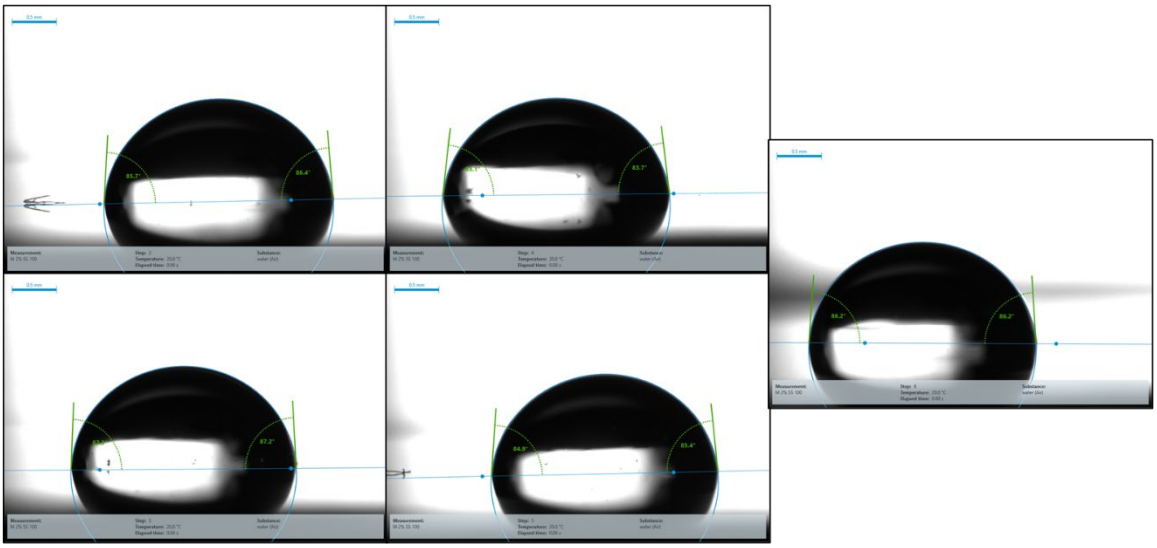

Polished 3 vol% GNP Stainless-Steel (67 J/mm^3) Energy Density

Polished 3 vol% GNP Stainless-Steel (80 J/mm^3) Energy Density

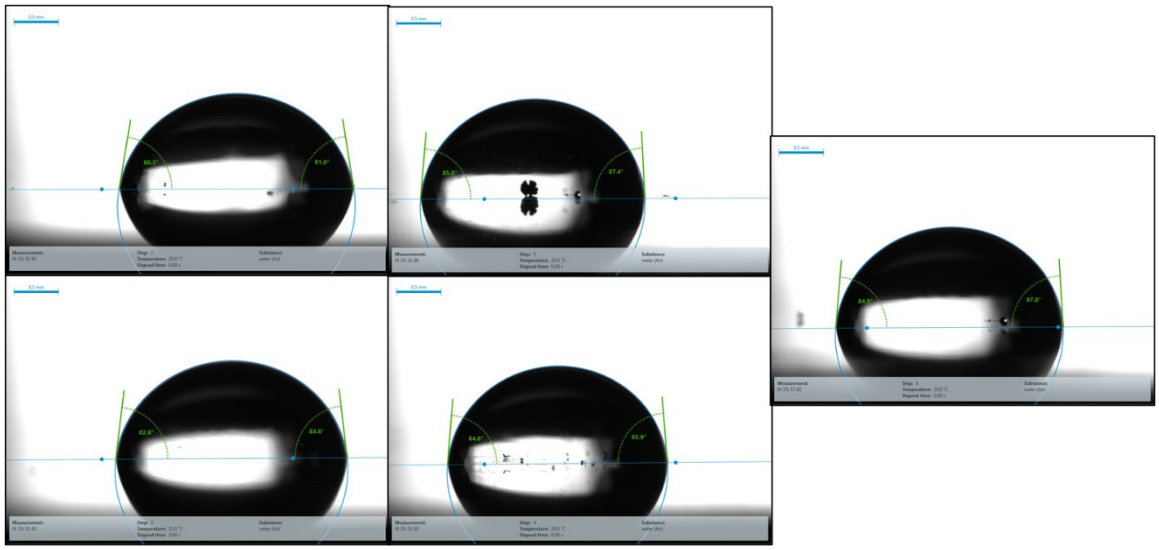

Polished 3 vol% GNP Stainless-Steel (90 J/mm^3) Energy Density

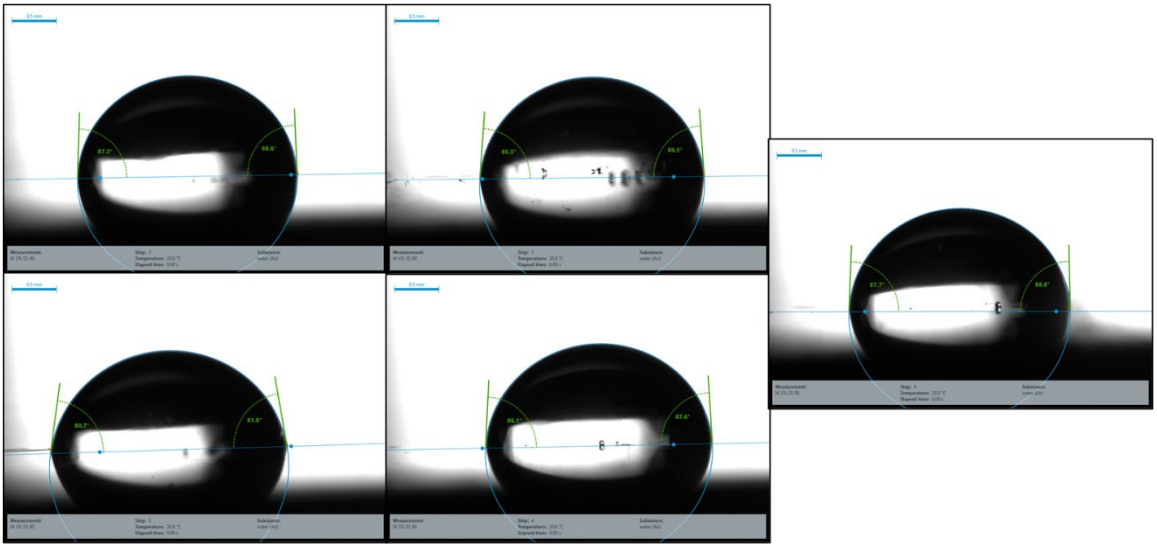

Polished 3 vol% GNP Stainless-Steel (100 J/mm^3) Energy Density

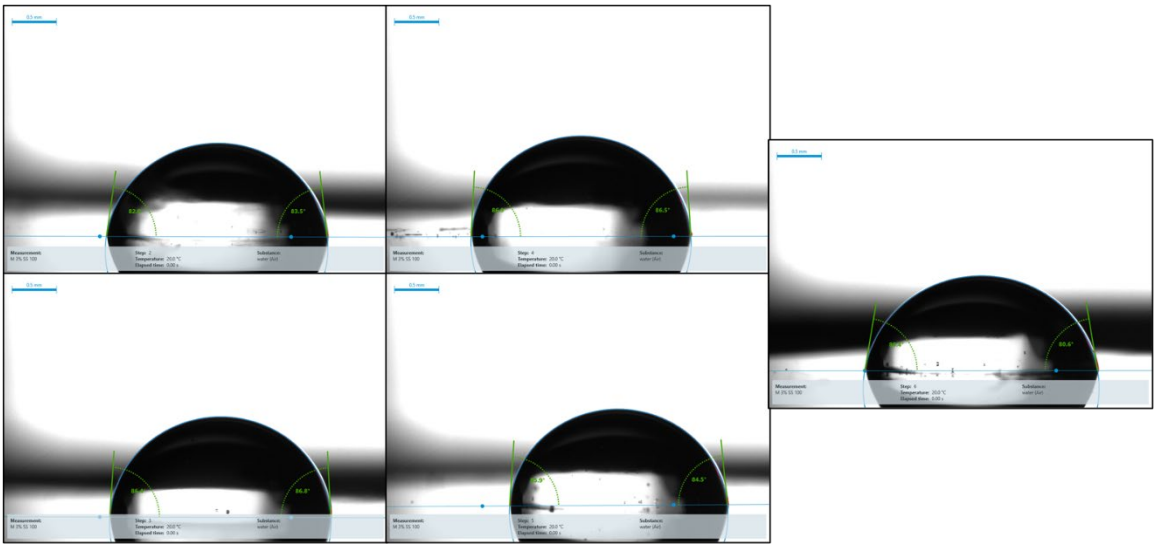

APPENDIX C: OPTICAL PROFILOMETRY SURFACE PROFILES

Standard Stainless-Steel (60 J/mm^3) Energy Density

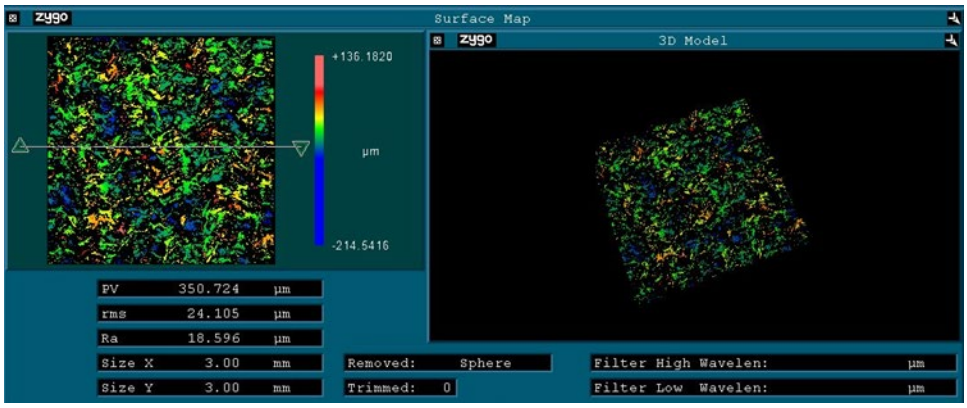

Standard Stainless-Steel (67 J/mm^3) Energy Density

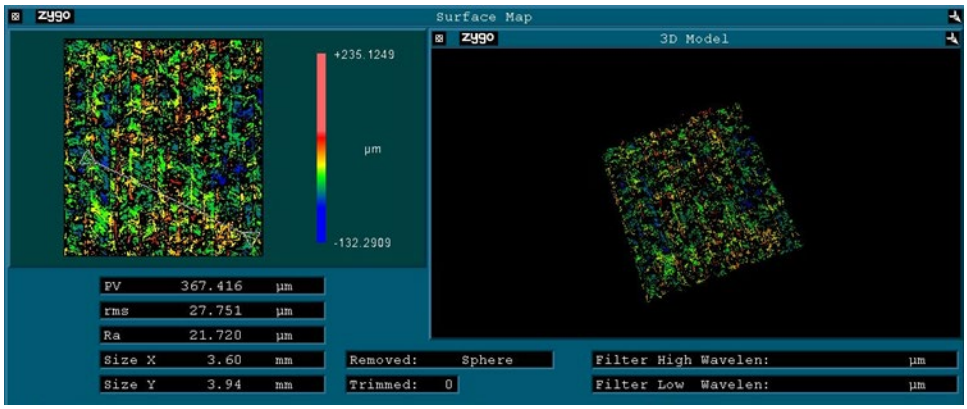

Standard Stainless-Steel (80 J/mm^3) Energy Density

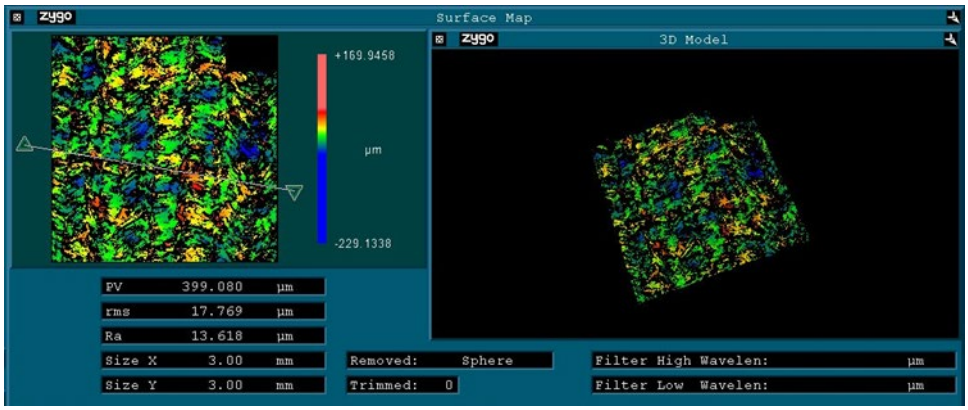

Standard Stainless-Steel (90 J/mm^3) Energy Density

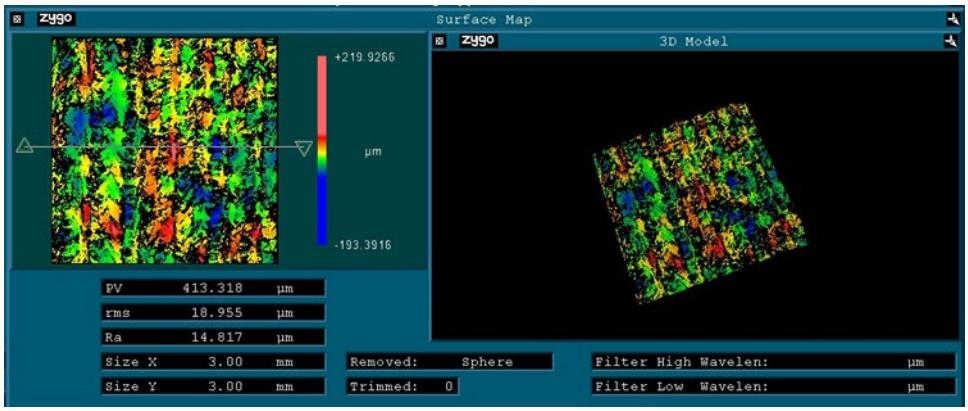

Standard Stainless-Steel (60 J/mm^3) Energy Density

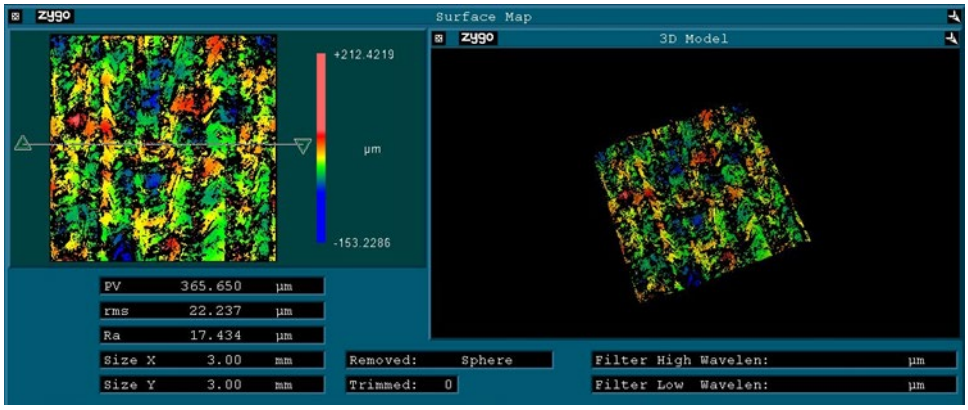

1 vol% Stainless-Steel (60 J/mm^3) Energy Density

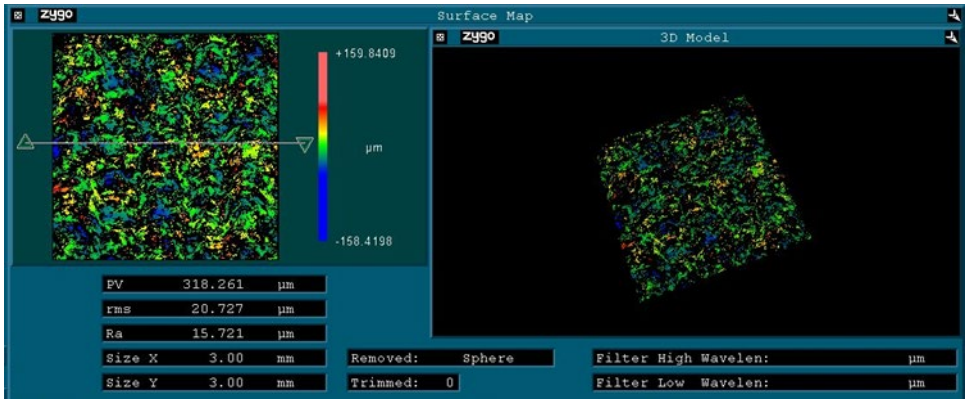

1 vol% Stainless-Steel (67 J/mm^3) Energy Density

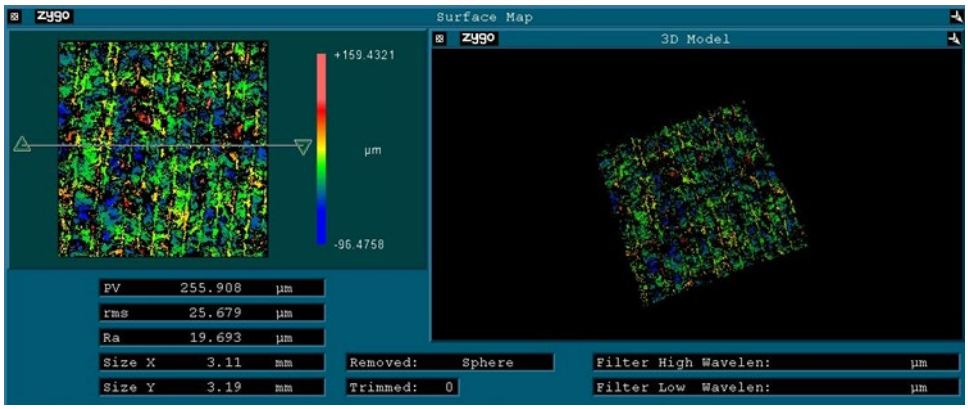

1 vol% Stainless-Steel (80 J/mm^3) Energy Density

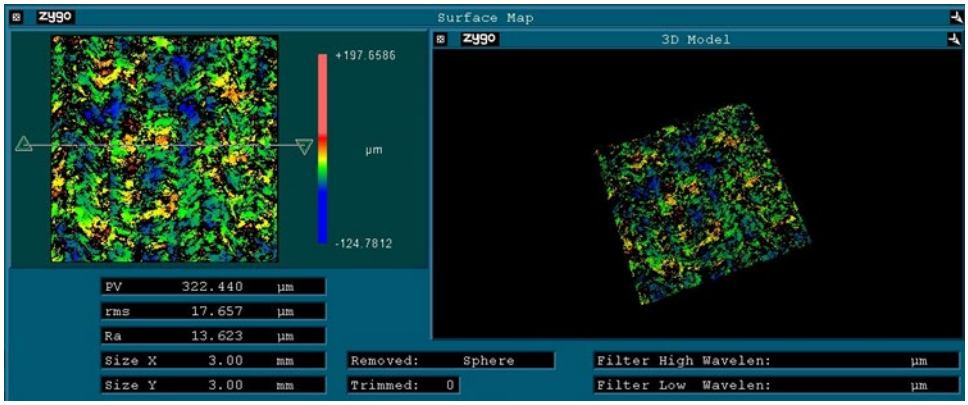

1 vol% Stainless-Steel (90 J/mm^3) Energy Density

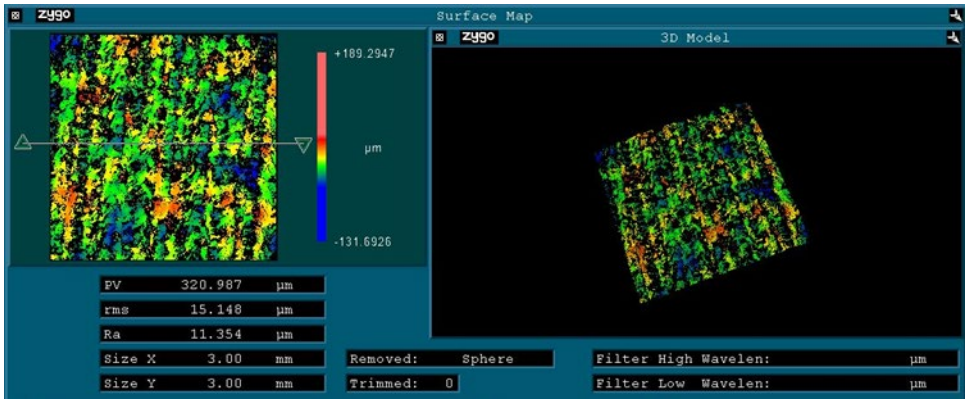

1 vol% Stainless-Steel (100 J/mm^3) Energy Density

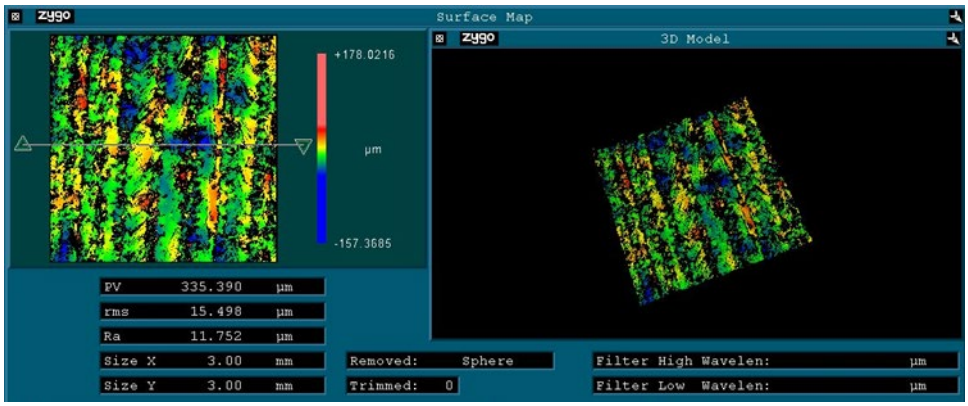

2 vol% Stainless-Steel (67 J/mm^3) Energy Density

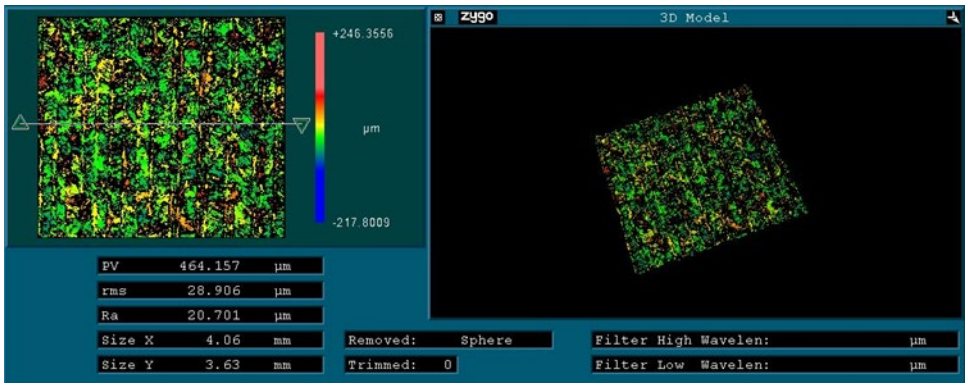

2 vol% Stainless-Steel (80 J/mm^3) Energy Density

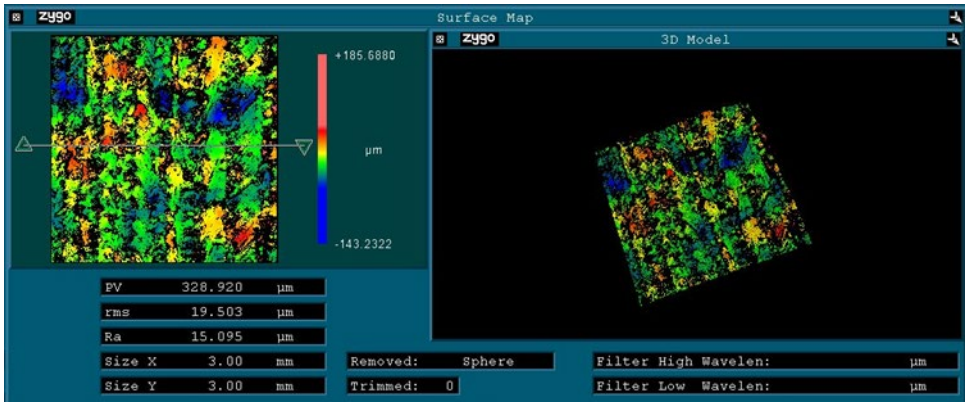

2 vol% Stainless-Steel (90 J/mm^3) Energy Density

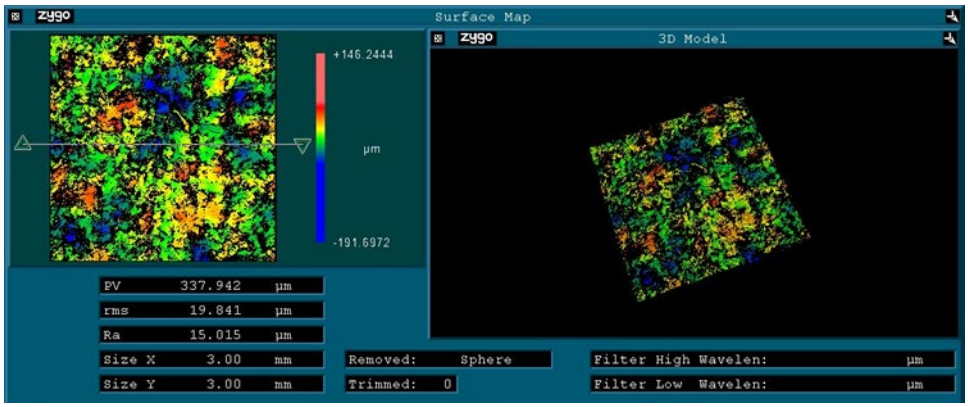

2 vol% Stainless-Steel (100 J/mm^3) Energy Density

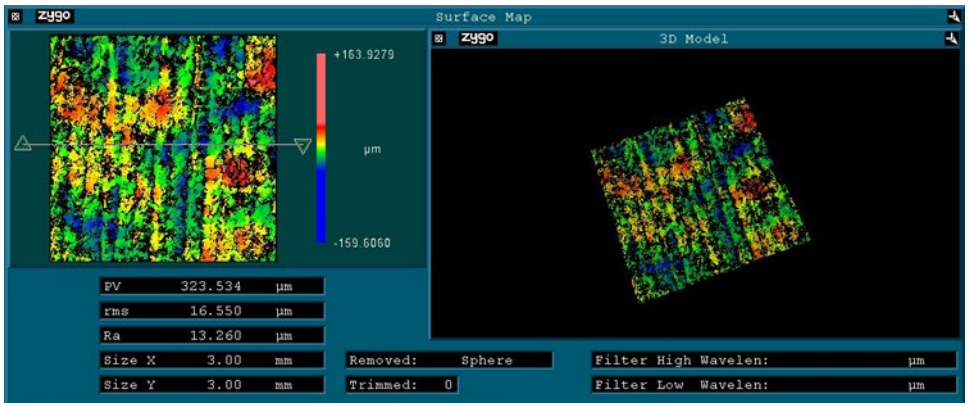

3 vol% Stainless-Steel (67 J/mm^3) Energy Density

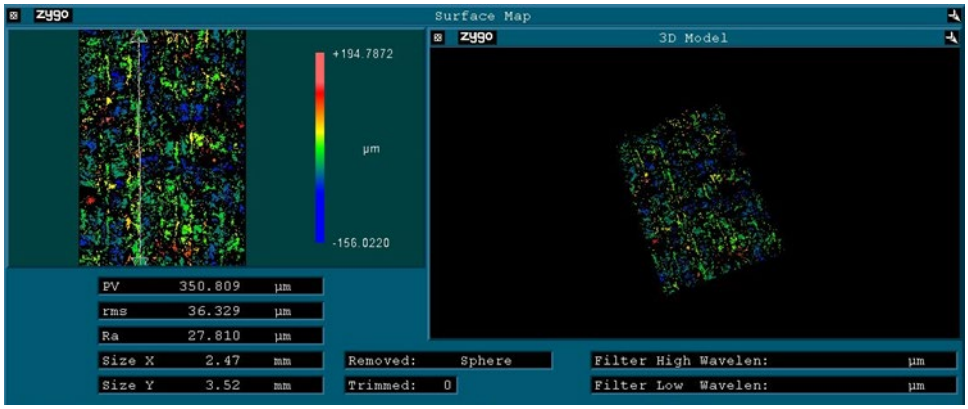

3 vol% Stainless-Steel (80 J/mm^3) Energy Density

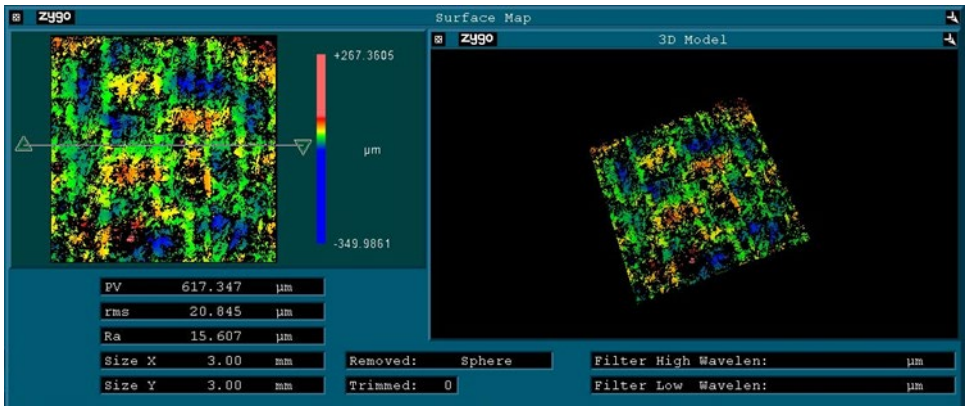

3 vol% Stainless-Steel (90 J/mm^3) Energy Density

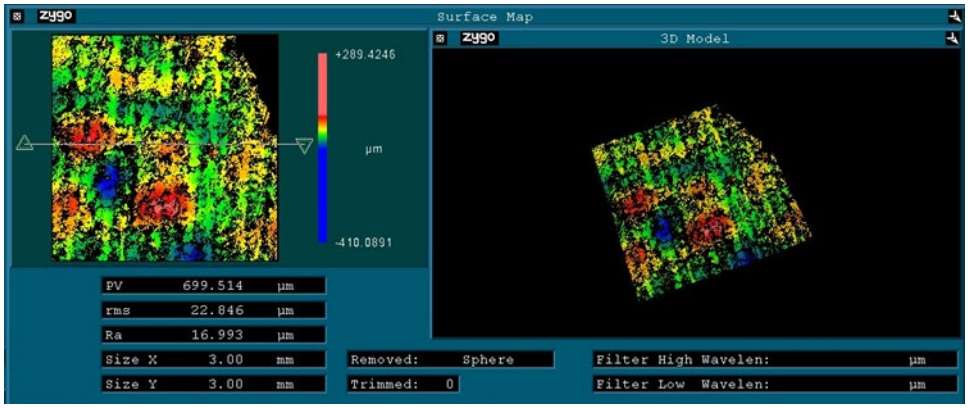

3 vol% Stainless-Steel (100 J/mm^3) Energy Density

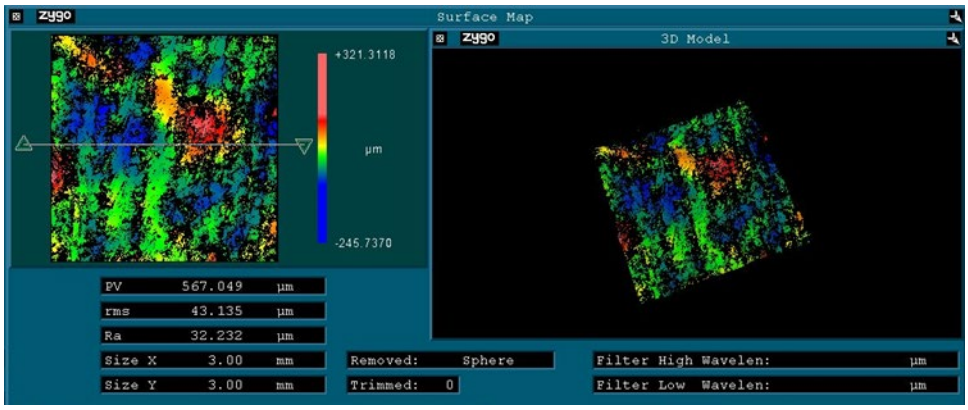

Polished Standard Stainless-Steel (60 J/mm^3) Energy Density

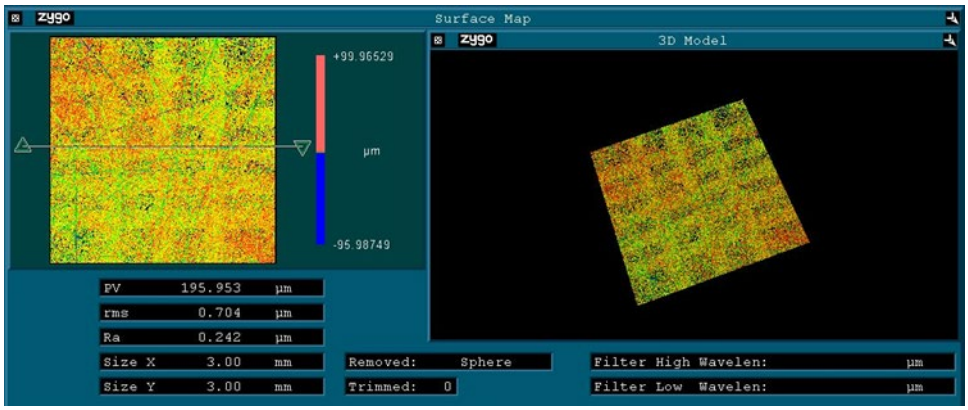

Polished Standard Stainless-Steel (67 J/mm^3) Energy Density

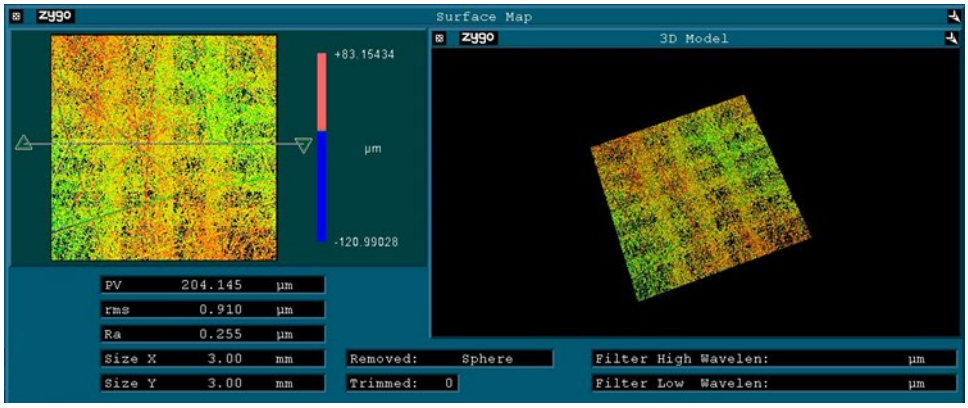

Polished Standard Stainless-Steel (80 J/mm^3) Energy Density

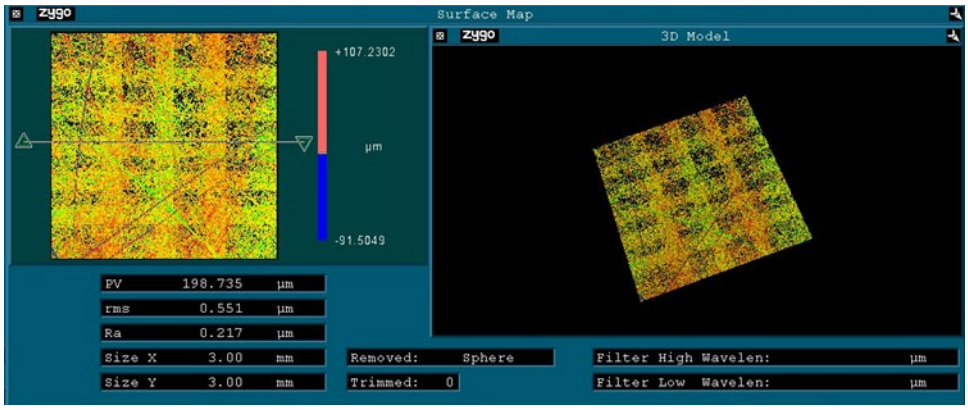

Polished Standard Stainless-Steel (90 J/mm^3) Energy Density

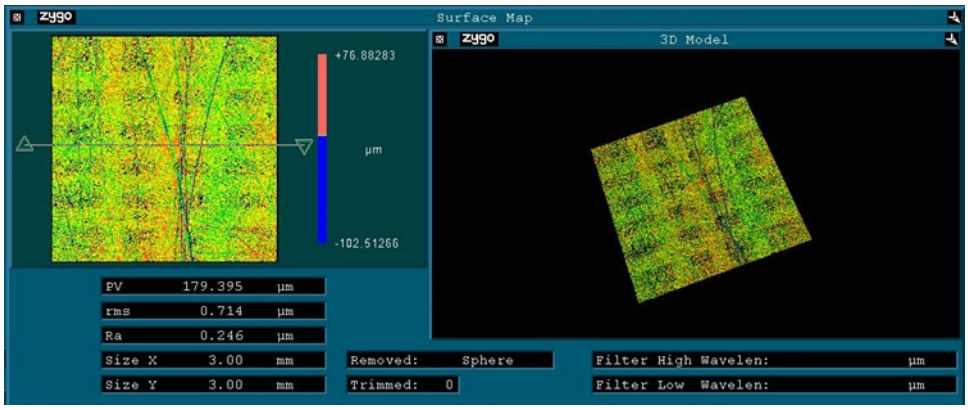

Polished Standard Stainless-Steel (100 J/mm^3) Energy Density

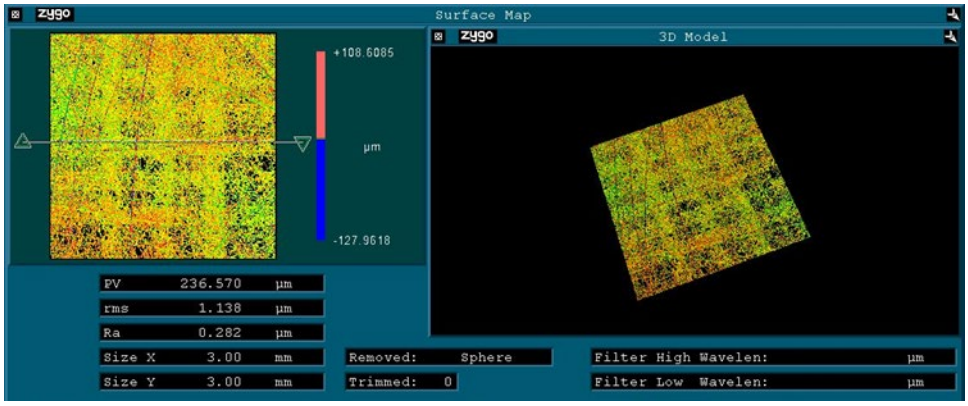

Polished 1 vol% Stainless-Steel (60 J/mm^3) Energy Density

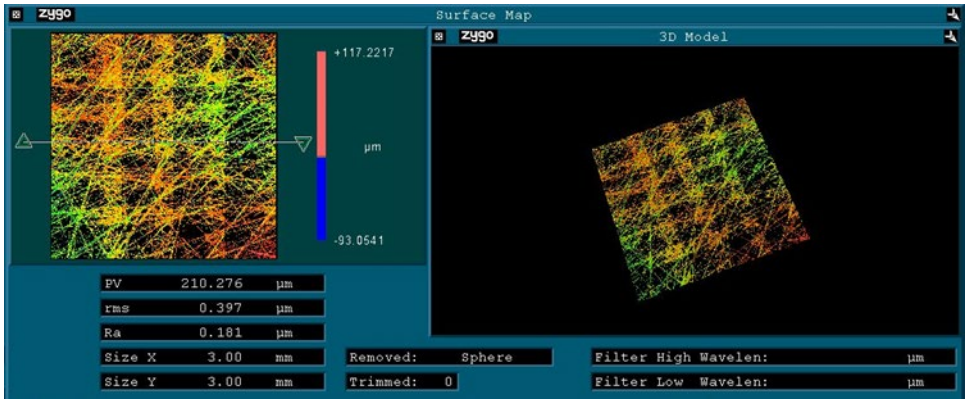

Polished 1 vol% Stainless-Steel (67 J/mm^3) Energy Density

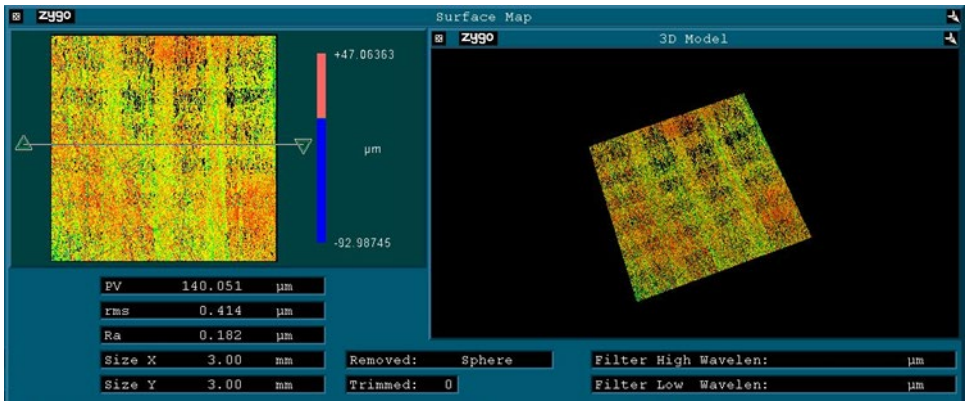

Polished 1 vol% Stainless-Steel (80 J/mm^3) Energy Density

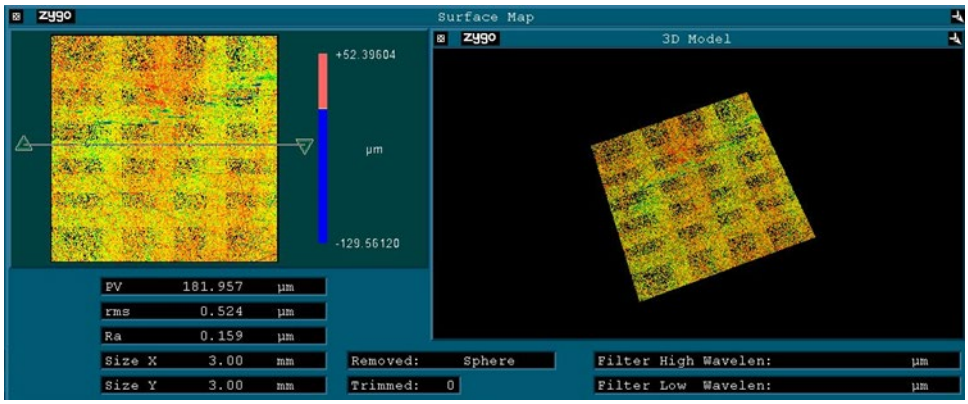

Polished 1 vol% Stainless-Steel (90 J/mm^3) Energy Density

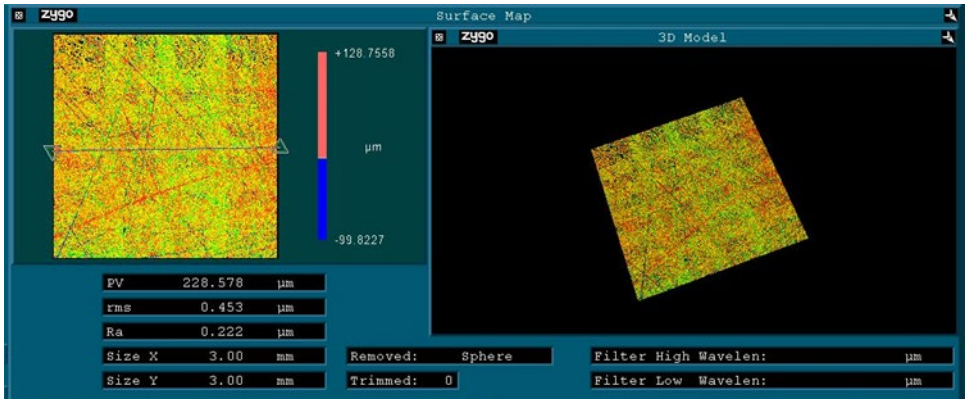

Polished 1 vol% Stainless-Steel (100 J/mm^3) Energy Density

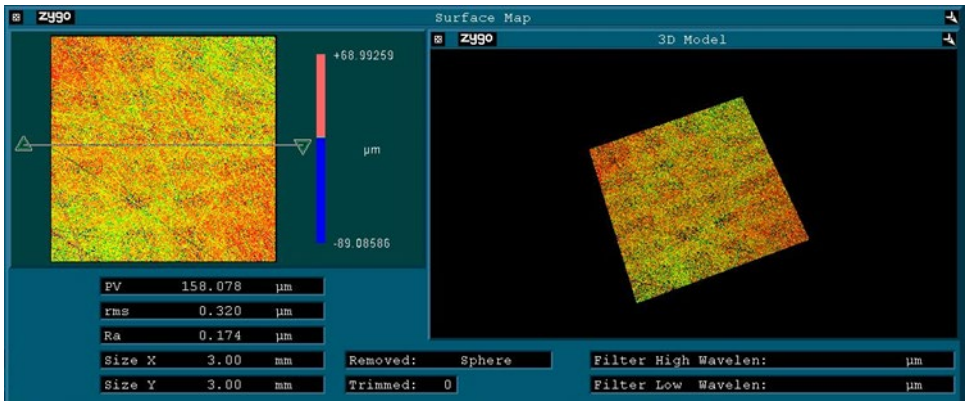

Polished 2 vol% Stainless-Steel (67 J/mm^3) Energy Density

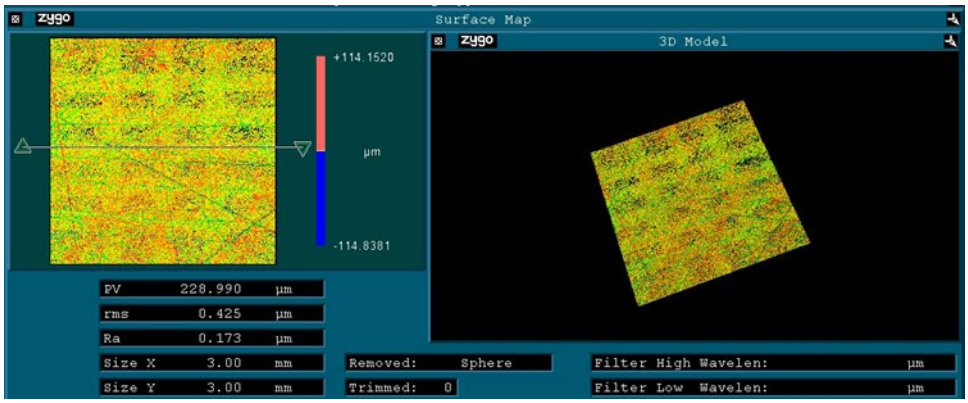

Polished 2 vol% Stainless-Steel (80 J/mm^3) Energy Density

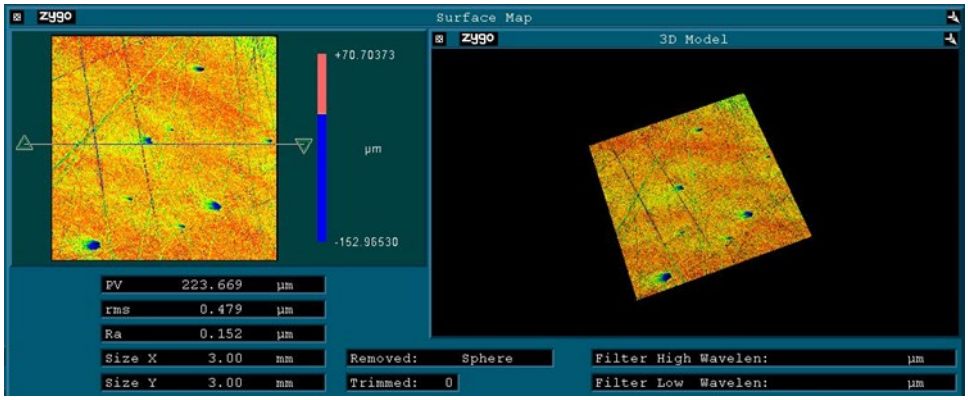

Polished 2 vol% Stainless-Steel (90 J/mm^3) Energy Density

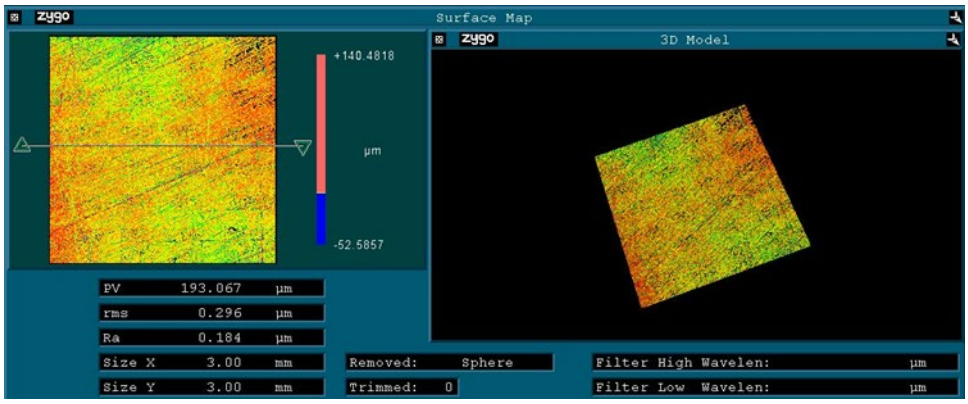

Polished 2 vol% Stainless-Steel (100 J/mm^3) Energy Density

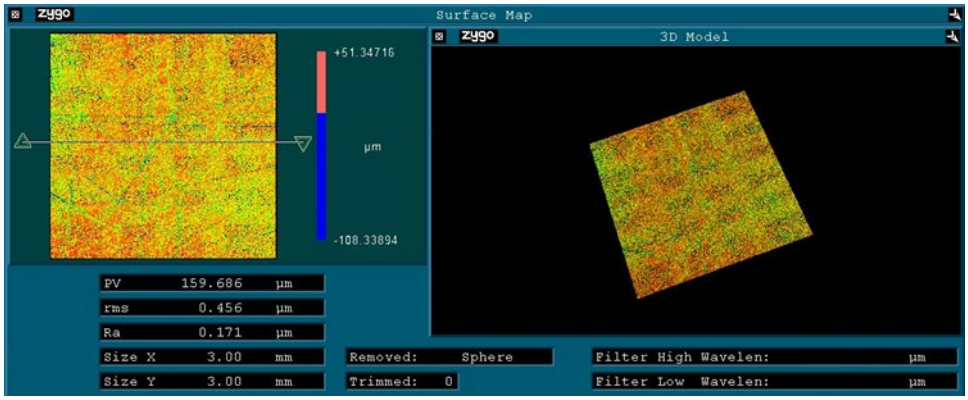

Polished 3 vol% Stainless-Steel (67 J/mm^3) Energy Density

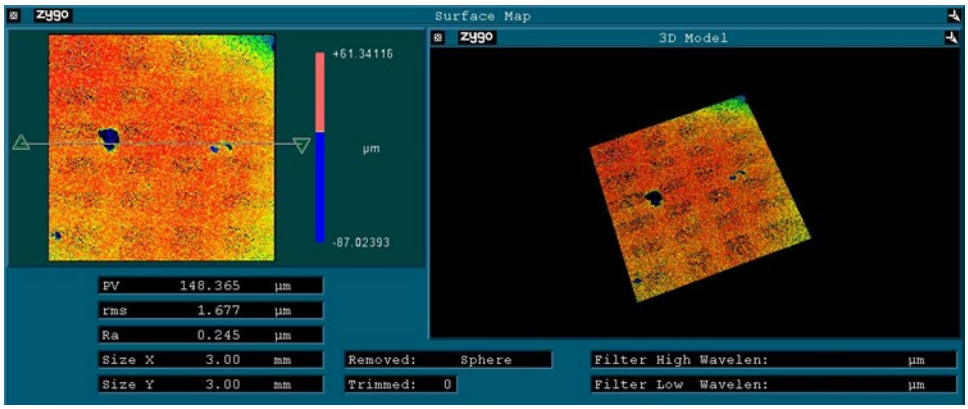

Polished 3 vol% Stainless-Steel (80 J/mm^3) Energy Density

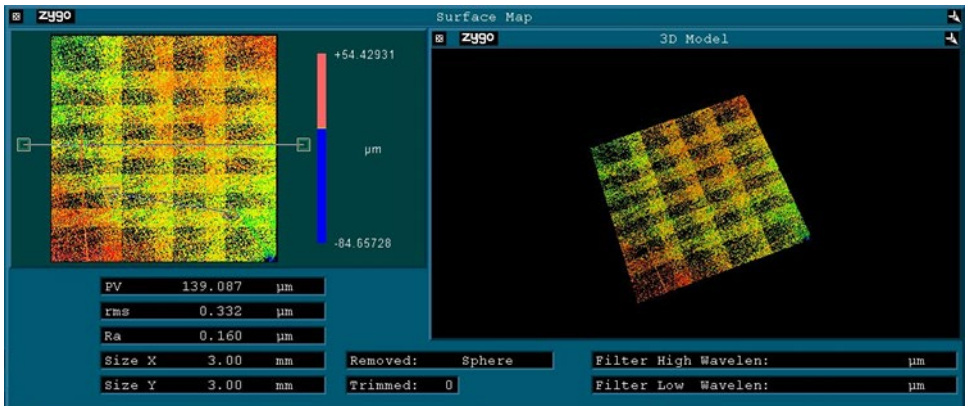

Polished 3 vol% Stainless-Steel (90 J/mm^3) Energy Density

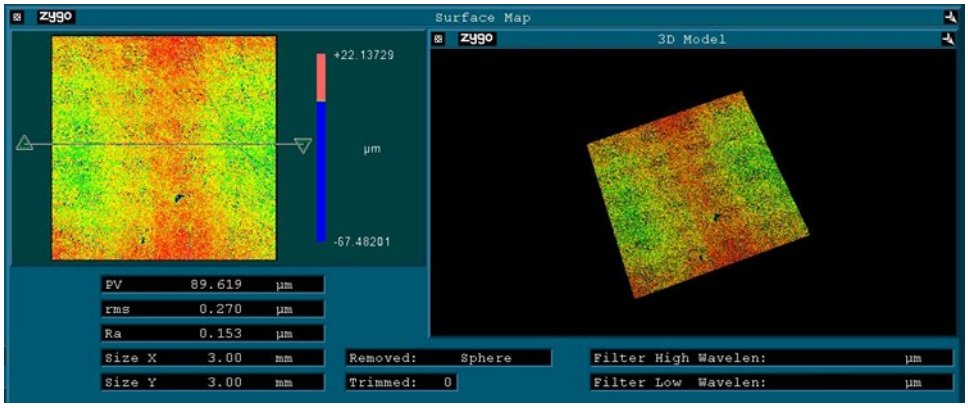

Polished 3 vol% Stainless-Steel (100 J/mm^3) Energy Density

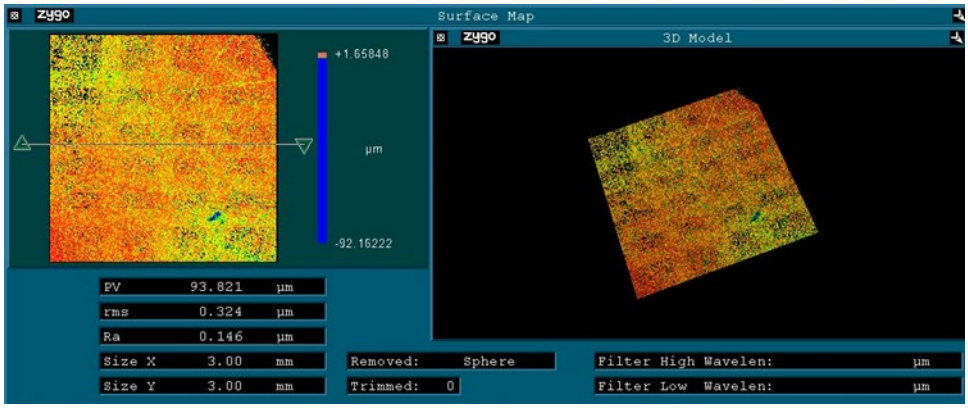

APPENDIX D: CONTACT ANGLE MEASUREMENT BY ENERGY DENSITY PLOTS

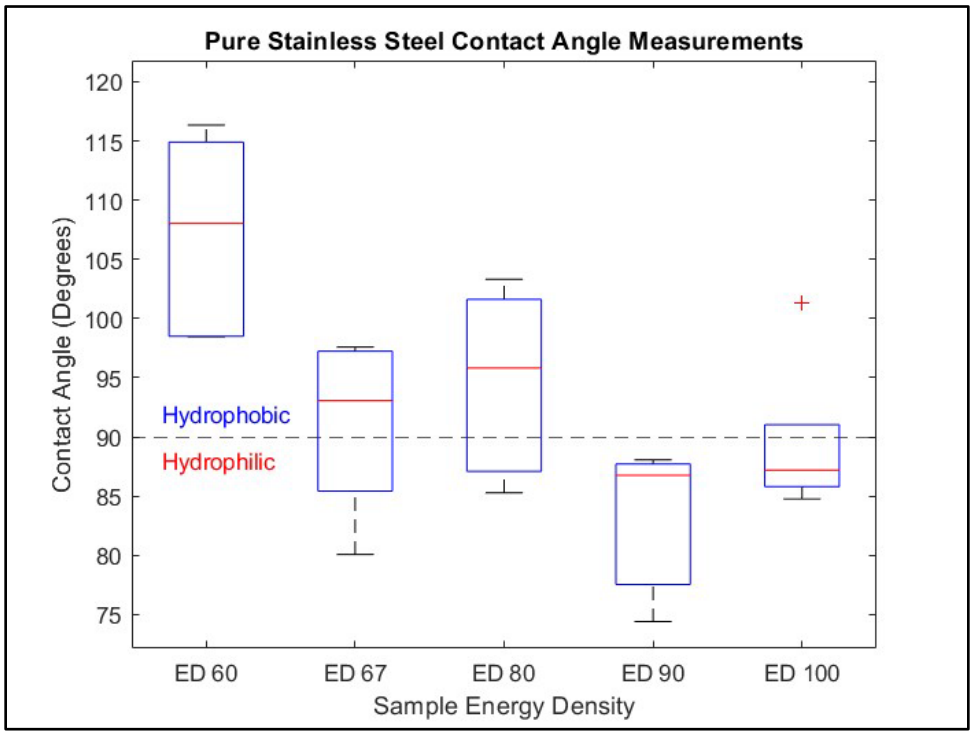

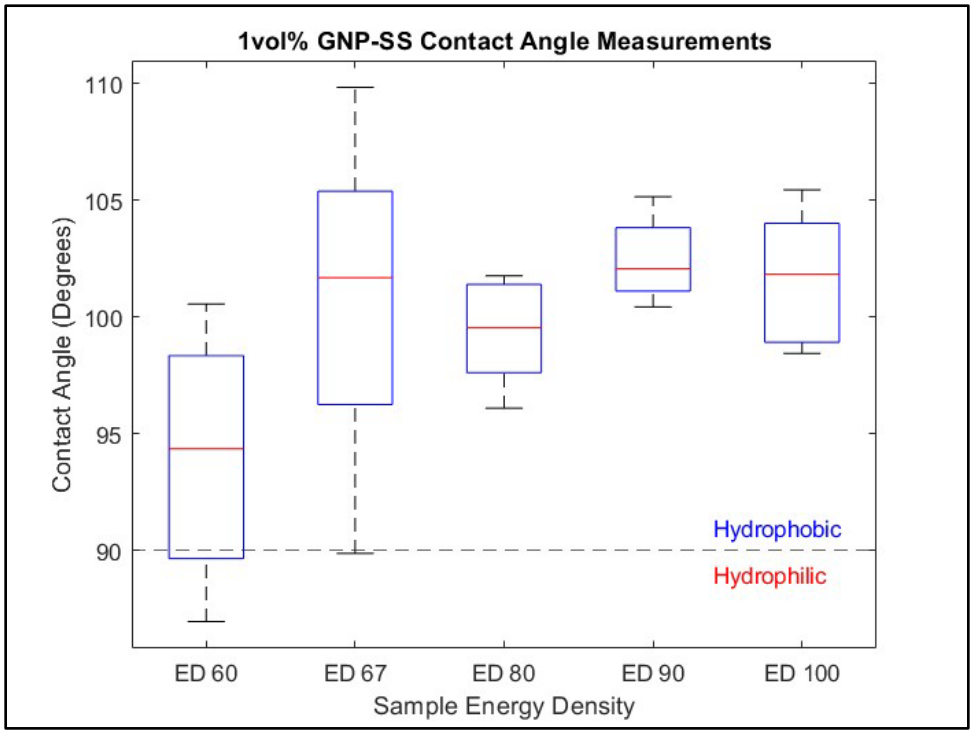

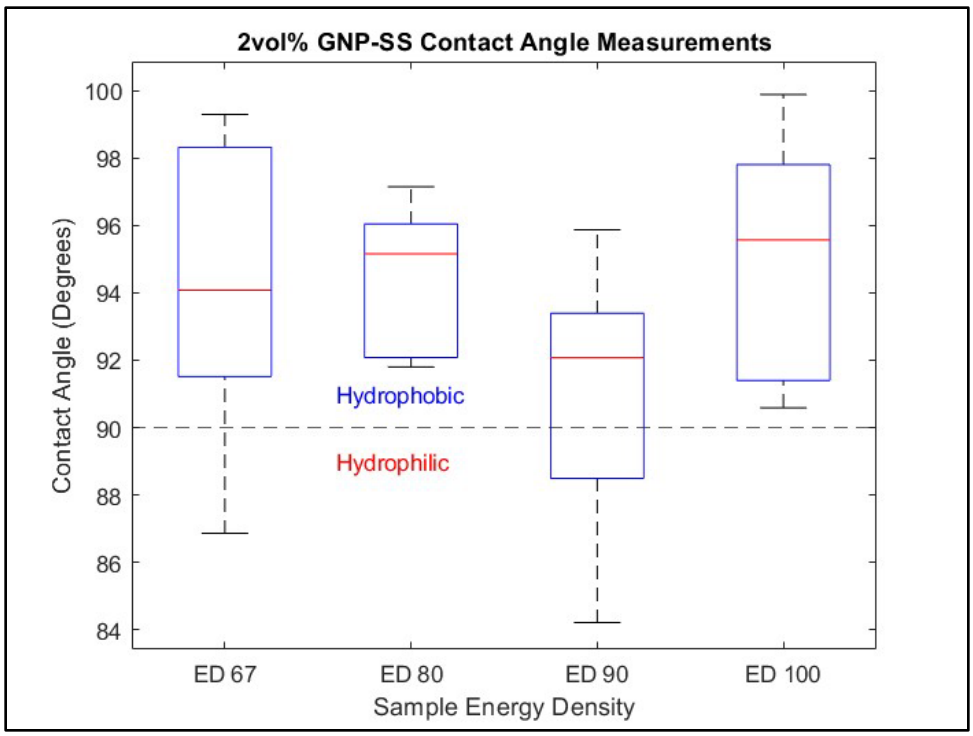
2vol% GNP-SS Contact Angle Measurements
Contact Angle (Degrees)
100
98
96
94
92
90
88
86
84
Hydrophobic
Hydrophilic
ED 67
ED 80
ED 90
ED 100
Sample Energy Density

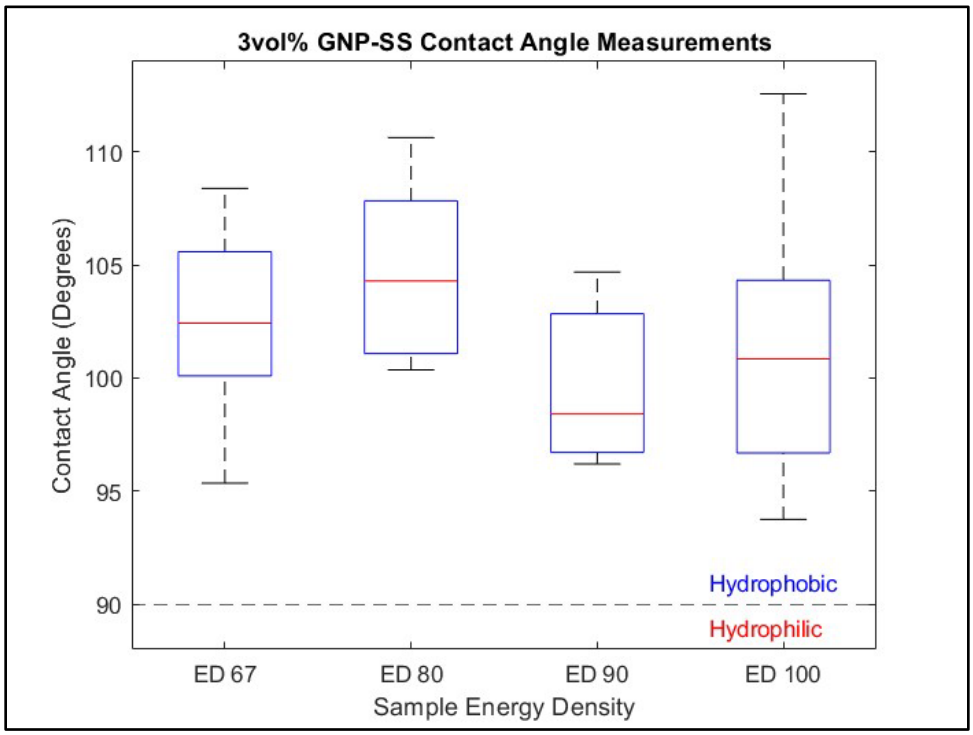
3vol% GNP-SS Contact Angle Measurements
Contact Angle (Degrees)
110
105
100
95
90
Hydrophobic
Hydrophilic
ED 67
ED 80
ED 90
ED 100
Sample Energy Density

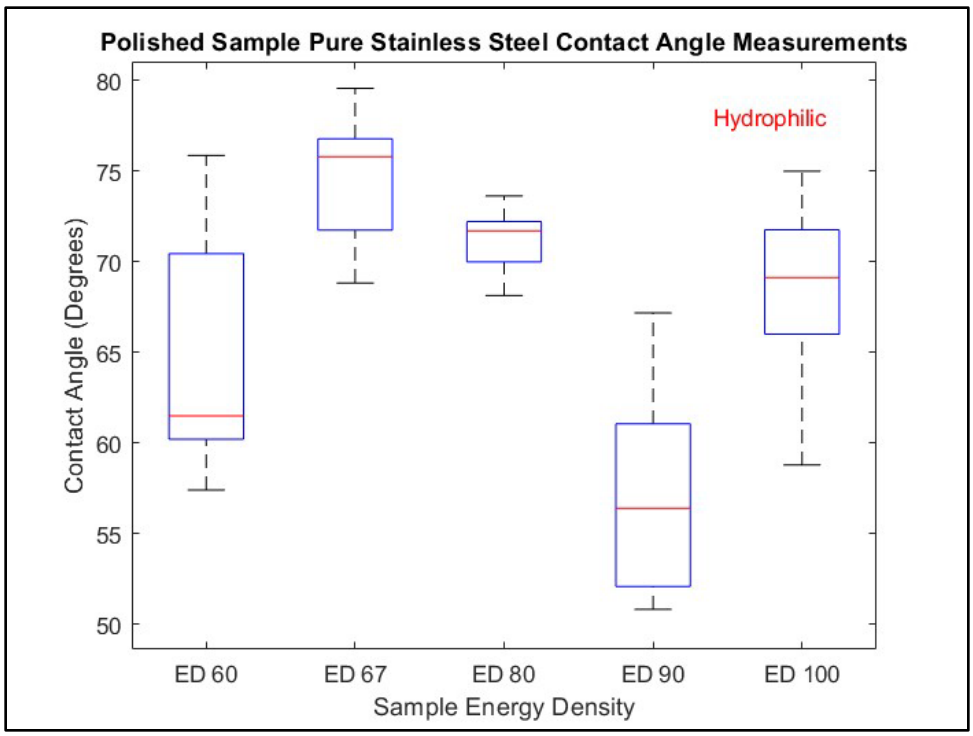
Polished Sample Pure Stainless Steel Contact Angle Measurements
Hydrophilic
Contact Angle (Degrees)
80
75
70
65
60
55
50
ED 60
ED 67
ED 80
ED 90
ED 100
Sample Energy Density

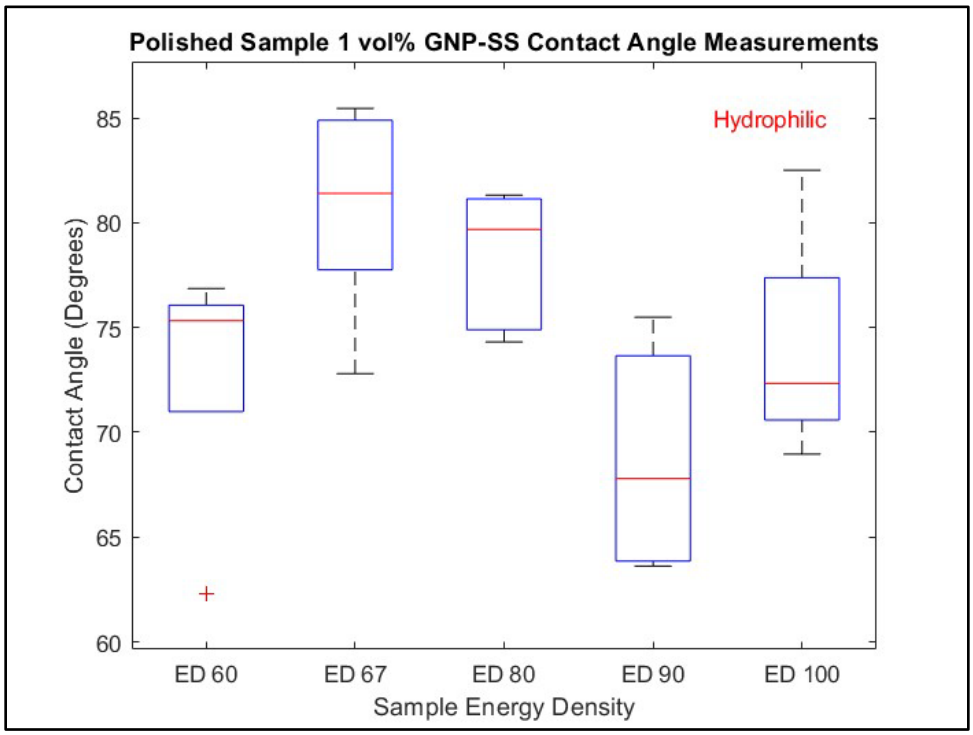
Polished Sample 1 vol% GNP-SS Contact Angle Measurements
Hydrophilic
Contact Angle (Degrees)
85
80
75
70
65
60
ED 60
ED 67
ED 80
ED 90
ED 100
Sample Energy Density

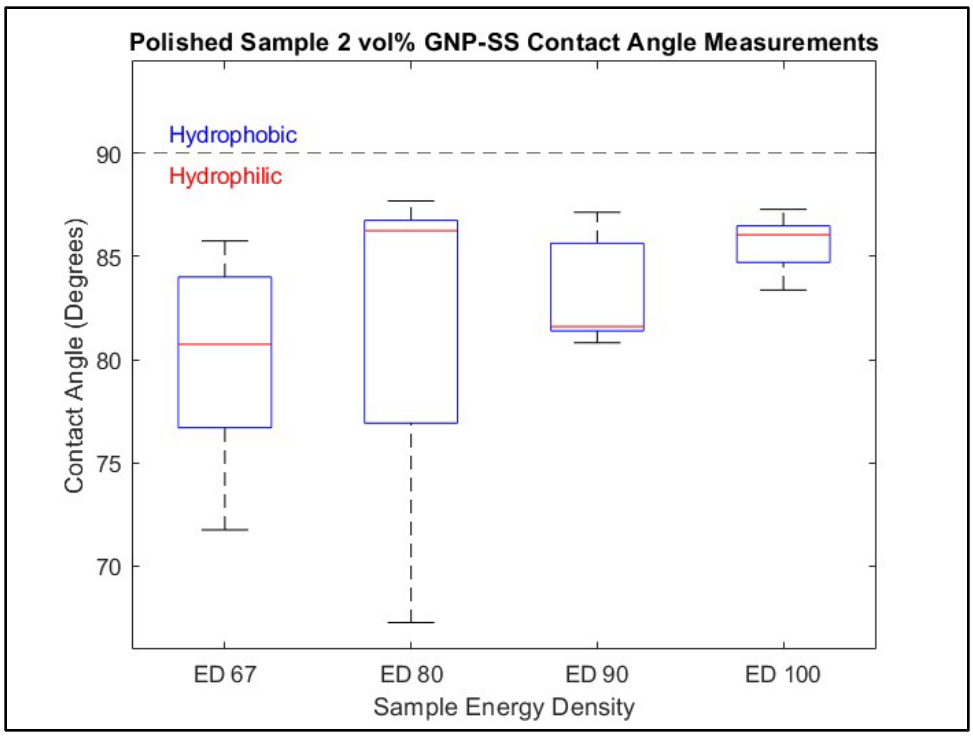
Polished Sample 2 vol% GNP-SS Contact Angle Measurements
Hydrophobic
Hydrophilic
90
85
80
75
70
Contact Angle (Degrees)
ED 67
ED 80
ED 90
ED 100
Sample Energy Density

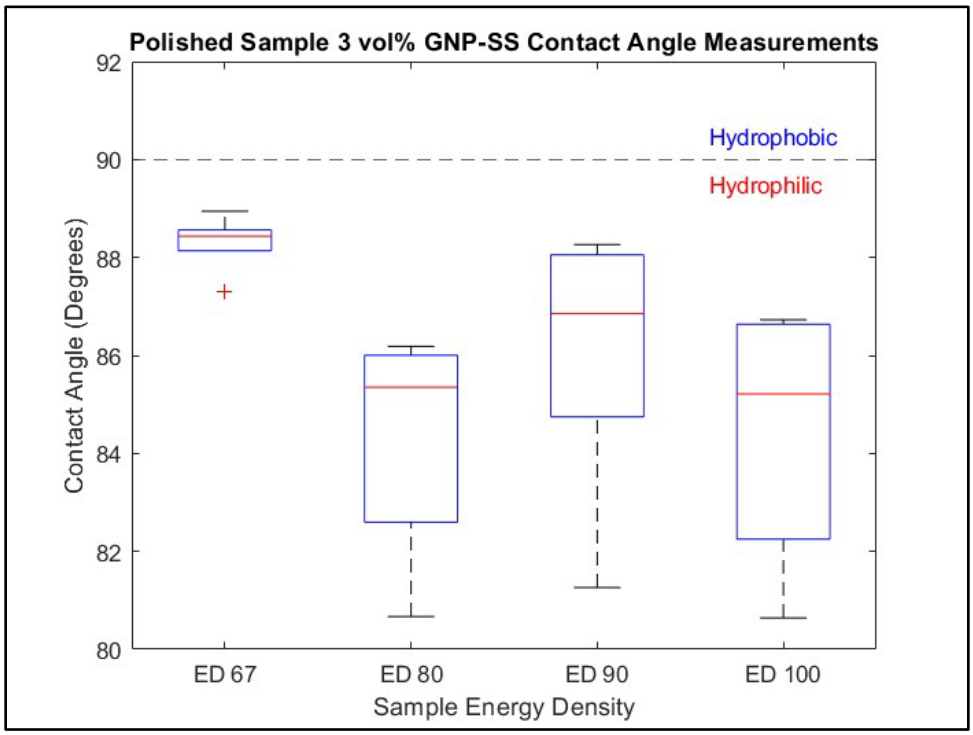
Polished Sample 3 vol% GNP-SS Contact Angle Measurements
92
90
88
86
84
82
80
Hydrophobic
Hydrophilic
Contact Angle (Degrees)
ED 67
ED 80
ED 90
ED 100
Sample Energy Density

LIST OF REFERENCES

[1] M. Iannuzzi and G. S. Frankel, "The carbon footprint of steel corrosion," *Npj Mater. Degrad.*, vol. 6, no. 101, London, UK, 2022, doi: 10.1038/s41529-022-00318-1.

[2] G. Koch, J. Varney, N. Thompson, O. Moghissi, M. Gould, and J. Payer, "International measures of prevention, application, and economics of corrosion technologies study," NACE International Impact, Columbia, MD, USA, 2016 [Online]. Available: http://impact.nace.org/economic-impact.aspx

[3] G. Kosh, M. Brongers, N. Thompson, Y. P. Virmani, and J. Payer, "Corrosion cost and preventative strategies in the United States," Office of Infrastructure Research and Development, Federal Highway Administration, Washington, DC, USA, Technical Report FHWA-RD-01-XXX.

[4] "Defense management observations on changes to the reporting structure for DOD's corrosion office and its implementation of GAO recommendations," United States Government Accountability Office, Congressional Committees GAO-19-513, Washington, DC, USA, 2019.

[5] E. F. Herzberg and A. Timko, "Cost of corrosion assessment guidebook," LMI Government Consulting, MEC70T4, Tysons, VA, USA 2008.

[6] R. A. Herron, "Department of defense corrosion prevention and control strategy." Office of the Under Secretary of Defense for Acquisition and Sustainment, Washington, DC, USA.

[7] "2011 Guidelines for the control and management of ships' biofouling to minimize the transfer of invasive aquatic species," International Maritime Organization, MEPC 62/64/Add.1, London, UK, 2011.

[8] A. Mosunov and V. Evstigneev, "Biofouling as one of the factors of substantial development of shipbuilding," *EDP Sci.*, no. 311, Sevastopol State University, Sevastopol, RU, 2021, doi: 10.1051/e3sconf/202131104003.

[9] T. McClay, C. Zabin, I. Davidson, R. Young, and D. Elam, "Vessel biofouling prevention and management options report," U.S. Coast Guard Research and Development Center, Final CG-D-15-15, Washington, DC, 2015.

[10] M. P. Schultz, J. A. Bendick, E. R. Holm, and W. M. Hertel, "Economic impact of biofouling on a naval surface ship," *Biofouling J. Bioadhesion Biofilm Res.*, vol. 27, no. 1, pp. 87–98, London, UK, 2011, doi: 10.1080/08927014.2010.542809.

[11] C. Winner, "To banish biofouling," *Ocean. Mag.*, vol. 50, no. 2, Woods Hole, MA, USA 2013.

[12] D. K. Steensma, "U.S. Navy aircraft corrosion prevention and control program," Department of Defense, Office of the Inspector General, Final 97–181, Washington, DC, USA, 1997.

[13] "Report to congress on the long-range plan for maintenance and modernization of naval vessels for fiscal year 2020," Naval Sea Systems Command, Washington, DC, USA, 2020.

[14] B. Dubose, "U.S. Navy utilizing remotely operated vehicles to check for corrosion," *Mater. Perform.*, vol. 59, no. 11, Columbia, MD, USA, 2020.

[15] K. Doogon, J. G. Kim, and C. N. Chu, "Aging effect on the wettability of stainless steel," *Mater. Lett.*, Erlangen, Germany, 2016, doi: 10.1016/j.matlet.2016.01.107.

[16] D. Chandler, "Explained: Hydrophobic and hydrophilic," *MIT News*, Massachusetts Institute of Technology, 2013 [Online]. Available: news.mit.edu

[17] C. Li, S. Richter, and S. Nesic, "How do inhibitors mitigate corrosion in oil-water two-phase flow beyond lowering the corrosion rate?," *Corros. Eng. Sect.*, vol. 70, no. 9, Houston, TX, USA, 2014, doi: 10.5006/1057.

[18] R. W. Revie and H. H. Uhlig, "Chapter 1: Definition and importance of corrosion," in *Corrosion and Corrosion Control, An Introduction to Corrosion Science and Engineering*, 4th ed., Hoboken, NJ, USA: John Wiley & Sons, 2008, pp. 1–8.

[19] V. Cicek and B. Al-Numan, *Corrosion Engineering and Cathodic Protection Handbook*. John Wiley & Sons, Hoboken, NJ, USA ,2017.

[20] V. Cicek, *Corrosion Engineering*. John Wiley & Sons, Hoboken, NJ, USA , 2014.

[21] S. Lower, *Chem1 Virtual Textbook*. Simon Fraser University: LibreTexts [Online]. Available: https://chem.libretexts.org/@go/page/182312

[22] R. Francis, *Avoiding Corrosion In Desalination Plants*. Houston, TX: NACE International, 2019.

[23] H. R. Copson, "Effects of velocity on corrosion by water," *Ind. Eng. Chem.*, vol. 44, no. 8, Bayonne, NJ, USA, 1952, doi: 10.1021/ie50512a019.

[24] N. Fredj and T. D. Burleigh, "Corrosion of carbon steel in waters of varying purity and velocity," presented at the NACE International Corrosion 2021 Conference, Columbia, MD, USA, 2012.

[25] A. Lopez-Ortega and J. L. Arana, "Evaluation of protective coatings for high-corrosivity category atmospheres in offshore applications," *Materials*, vol. 12, no. 8, p. 1325, Bilbao, Spain, 2019, doi: 10.3390/ma12081325.

[26] "Cathodic protection of offshore structures." American Bureau of Shipping, Spring, TX, USA, 2018.

[27] K. Sotoodeh, *Coating Application for Piping, Valves, and Actuators in Offshore Oil and Gas Industry*, 1st ed. CRC Press, Boca Raton, FL, USA, 2023.

[28] "Corrosion resistance or stainless steels," WorldStainless, WorldStainless [Online]. Available: https://www.worldstainless.org/files/issf/Education /English/Module_05_Corrosion_Resistance_of_Stainless_Steels_en.pdf

[29] "EOS stainlesssteel 316l material data sheet." [Online]. Available: https://www.eos.info/03_system-related-assets/material-related-contents/metal-materials-and-examples/metal-material-datasheet/stainlesssteel/ss-316l_9011-0032_m100_material_data_sheet_flexline_06-22_en.pdf

[30] *Cleaning and Descaling Stainless Steels: A Designers' Handbook Series*. in 9001. American Iron and Steel Institute, Washington, DC, USA.

[31] L. Duta *et al*., "Wettability of nanostructured surfaces," in *Wetting Wettability* by M. Aliofkhazraei, InTechOpen Limited, London, UK, 2015, doi: 10.5772/60808.

[32] A. Moldovan and M. Enachescu, "Wetting properties at nanometer scale," in *Wetting Wettability* by M. Aliofkhazraei, InTechOpen Limited, London, UK, 2015, doi: 10.5772/60886.

[33] J. Streator, "Solid-Liquid-Solid Interfaces," in *Surf. Energy* by M. Aliofkhazraei, InTechOpen Limited, London, UK, 2015, doi: 10.5772/59354.

[34] S. Lower, *Chem1 Virtual Textbook: Cohesive and Adhesive Forces*. Simon Fraser University: LibreTexts [Online]. Available: https://chem.libretexts.org/@go/page/1499

[35] J. R. Astillero *et al*., "Relationship of the difference in surface tension of immiscible liquids to the contact angle of an antibubble," *Metall. Engineering*, vol. 18, Quezon City, Philippines, 2013.

[36] A. Sarkar and A.-M. Kietzig, "General equation of wettability: A tool to calculate the contact angle for a rough surface," *Chem. Phys. Lett.*, Amsterdam, Netherlands, 2013, doi: 10.1016/j.cplett.2013.04.055.

[37] E. Vazirinasab, R. Jafari, and G. Momen, "Application of superhydrophobic coatings as a corrosion barrier: A review," *Surf. Coat. Technol.*, vol. 341, Amsterdam, Netherlands, 2017, doi: 10.1016/j.surfcoat.2017.11.053.

[38] J. Simpson, S. Hunter, and T. Aytug, "Superhydrophobic materials and coatings: A review," *Rep. Prog. Phys.*, vol. 78, Bristol, UK, 2015, doi: 10.1088/0034-4885/78/8/086501.

[39] K. Seo, M. Kim, and D. H. Kim, "Re-derivation of Young's equation, Wenzel equation, and Cassie-Baxter equation based on energy minimization," in *Surf. Energy* by M. Aliofkhazraei, InTechOpen Limited, London, UK, 2015, doi: 10.5772/61066.

[40] P. M. Costanzo et al., "Comparison between direct contact angle measurements and thin layer wicking on synthetic monosized cuboid hematite particles," *Langmuir*, vol. 11, Washington, DC, USA, 1995, doi: 10.1021/la00005a064.

[41] F. Leroy and F. Muller-Plathe, "Rationalization of the behavior of solid-liquid surface free energy of water in cassie and wenzel wetting states on rugged solid surfaces at the nanometer scale," *Langmuir*, Washington, DC, USA, 2010, doi: 10.1021/la104018k.

[42] M. Samaha *et al*., "Superhydrophobic surfaces: From the lotus leaf to the submarine," *Acad. Sci.,* Amsterdam, Netherlands, 2012, doi: 10.1016/j.crme.2011.11.002.

[43] H. J. Ensikat, P. Ditsche-Kuru, C. Neinhuis, and W. Barthlott, "Superhydrophobicity in perfection: the outstanding properties of the lotus leaf," *Beilstein J. Nanotechnol.*, vol. 2, pp. 152–161, Frankfurt, Germany, 2011, doi: 10.3762/bjnano.2.19.

[44] "What is teflon? What is teflon used For? | DCW," *ptfedf*, May 30, 2022. https://www.ptfedf.com/what-is-teflon-2/ (accessed Apr. 10, 2023).

[45] "20 uses of teflon in daily life – StudiousGuy." https://studiousguy.com/uses-of-teflon/ (accessed Apr. 10, 2023).

[46] F. Adamopoulos *et al*., "Fluorosilane water-repellent coating for the protection of marble, wood and other materials," *Heritage*, vol. 4, Basel, Switzerland, 2021, doi: 10.3390/heritage4040150.

[47] M. R. Dasaev *et al*., "Effect of laser treatment on zinced steel surface wettability and corrosion resistance," *J. Phys.*, Melville, NY, USA, 2022, doi: 10.1088/1742-6596/2388/1/012083.

[48] J. Budan, "Engineering superhydrophobic behavior in 3D-printed stainless steel composites," Naval Postgraduate School [Online]. Available: http://hdl.handle.net/10945/70641

[49] M. Galimberti, V. Barbera, and A. Sironi, "Controlled functionalization of graphene layers," in *Graphene Materials Structure, Properties and Modifications*, 2017 [Online]. Available: doi: 10.5772/65151

[50] A. Jimenez-Suarez and S. G. Prolongo, "Graphene nanoplatelets," *MDPI Appl. Sci.*, vol. 10, no. 1753, Basel, Switzerland, 2020, doi: doi:10.3390/app10051753.

[51] T. Radadiya, "Properties of Graphene," *Eur. J. Mater. Sci.*, vol. 2, no. 1, pp. 6–18, Abingdon, UK, 2015.

[52] A. K. Geim and K. S. Novoselov, "The rise of graphene," *Nat. Mater.*, vol. 6, New York, NY, USA, 2007.

[53] "xGnP graphene nanoplatelets material data safety sheet," XG Sciences, xGnP MSDS Rev. 2.1.0, Lansing, MI, USA, 2010.

[54] C. N. R. Rao *et al*., "Graphene: The new two-dimensional nanomaterial," *Angew. Chem.*, Hoboken, NJ, USA, 2009, doi: 10.1002/anie.200901678.

[55] J.-H. Ding, H.-R. Zhao, and H.-B. Yu, "A water-based green approach to large-scale production of aqueous compatible graphene nanoplatelets," *Sci. Rep.*, no. 8, London, UK, 2018, doi: 10.1038/s41598-018-23859-5.

[56] A. Dimev *et al*., "Chemical mass production of graphene nanoplatelets in ~100% yield," *ACS Nano*, vol. 10, Washington, DC, USA, 2016, doi: 10.1021/acsnano.5b06840.

[57] W. Hu *et al*., "Graphene-based antibacterial paper," *ACS Nano*, vol. 4, no. 7, Washington, DC, USA, 2010.

[58] H. Zhou *et al*., "Surface deposition of graphene layer for bioactivity improvement of biomedical 316 stainless steel," *Mater. Lett.*, vol. 192, Amsterdam, Netherlands, 2017, doi: 10.1016/j.matlet.2016.12.043.

[59] Y. Song *et al*., "Biomimetic super hydrophobic structured graphene on stainless steel surface by laser processing and transfer technology," *Surf. Coat. Technol.*, no. 328, Amsterdam, Netherlands, 2017, doi: 10.1016/j.surfcoat.2017.08.031.

[60] N. Asnafi, "Metal additive manufacturing – State of the art 2020," *Metals*, vol. 11, no. 867, Besel, Switzerland, 2021, doi: 10.3390/met11060867.

[61] E. Toyserkani *et al*., *Metal Additive Manufacturing*. Hoboken, New Jersey: John Wiley & Sons, 2022.

[62] L. Bian *et al*., *Laser-Based Additive Manufacturing of Metal Parts: Modeling, Optimization, and Control of Mechanical Properties*. Boca Raton, FL: CRC Press.

[63] I. Yadroitsev, I. Yadroitsava, and A. Du Plessis, "Basics of laser powder bed fusion," in *Fundamentals of Laser Powder Bed Fusion of Metals*, Free State, South Africa, 2021.

[64] "EOS M systems laser sintering system for metal powder training manual." EOS GmbH, Krailling, Germany.

[65] I. Yadroitsev and I. Yadroitsava, "A step-by-step guide to the L-PBF process," in *Fundamentals of Laser Powder Bed Fusion of Metals*, Free State, South Africa, 2021.

[66] "8000D dual mixer/mill operating manual." SPEX Sample Prep, Metuchen, NJ, USA, 2010.

[67] "EOS M 100 additive manufacturing system for the fast and efficient production of delicate metal parts," EOS GmbH, Krailling, Germany.

[68] "datasheet-7100-d834.pdf." Accessed: Apr. 05, 2023 [Online]. Available: http://www.lao.cz/data/ke-stazeni/datasheet-7100-d834.pdf

[69] J. Wyant and O. Center, "White light interferometry," vol. 4737, University of Arizona, Tuscon, AZ, USA, 2002 [Online]. Available: http://wp.optics.arizona.edu/jcwyant/wp-content/uploads/sites/13/2016/08/WhiteLightInterferometry.pdf

[70] J. Hernandez *et al*., "The 2D continuous wavelet transform: Applications in fringe pattern processing for optical measurement techniques," *Wavelet Theory Its Appl.*, Boston, MA, USA, 2018, doi: 10.5772/intechopen.74813.

INITIAL DISTRIBUTION LIST

1. Defense Technical Information Center
   Ft. Belvoir, Virginia

2. Dudley Knox Library
   Naval Postgraduate School
   Monterey, California